PHOTONIC CRYSTALS FOR OPTOFLUIDIC TRANSPORT, TRAPPING AND BIOSENSING

A Dissertation

Presented to the Faculty of the Graduate School

of Cornell University

In Partial Fulfillment of the Requirements for the Degree of

Doctor of Philosophy

by

Sudeep Mandal

February 2010

PHOTONIC CRYSTALS FOR OPTOFLUIDIC TRANSPORT, TRAPPING AND BIOSENSING

Sudeep Mandal, Ph. D.

Cornell University 2010

Photonic crystals, since their discovery in 1987 have been of great interest to the optics community. Their unique optical properties have revolutionized the field of photonics and have enabled a new class of optical devices with applications in a broad range of areas such as creating nanophotonic light guiding circuits, efficient optical add-drop filters and modulators as well as a new class of low loss optical fibers. This thesis work aims to exploit the optical properties of photonic crystals that enable them to strongly confine and guide light towards developing and designing novel optical devices for performing optofluidic transport, trapping and biosensing.

While optical biosensors are of great interest to the biosensing community, one of the limitations of current optical nanobiosensors is their inability to perform a large number of detections in parallel. I have demonstrated a novel one-dimensional resonant photonic crystal architecture that is extremely well suited for performing highly sensitive and multiplexed, label-free biological detections. These sensors also have very a small form-factor allowing for the successful detection of tens of attograms of bound mass on the sensor surface.

Over the last two decades, optical tweezers have been developed to exert optical forces for trapping and manipulating microparticles and cells. However, they exhibit two significant drawbacks. Firstly, they have a very small interaction length over which they can exert optical forces on particles thus limiting the distances over

which particles can be propelled using optical scattering forces. Additionally, they are diffraction limited systems which make them incapable of trapping smaller objects such as dielectric nanoparticles and biomolecules. In my doctoral work, I have demonstrated for the first time, the ability to exploit liquid-core waveguiding structures to propel dielectric microspheres over long distances due to their ability to strongly confine and guide light thus overcoming the limitation of previous systems with respect to their small interaction lengths. I have also demonstrated a resonant photonic crystal architecture that overcomes the limitations imposed by diffraction by confining the optical field to sub-wavelength volumes while simultaneously amplifying it. This has enabled the trapping of nanoparticles as small as 48-nm (in diameter) and trap stiffnesses that are an order of magnitude higher than the current state-of-the-art.

The results of this work will enable future devices with the ability to potentially trap and sense single biomolecules such as proteins. In addition, by integrating these photonic crystal elements with other photonic circuit elements, it opens up a vast number of exciting possibilities for optofluidically enabled transport in micro and nano-fluidic systems. In particular, my doctoral research lays down the groundwork for enabling future work on sensitive size based optical chromatography and ultra-sensitive biosensors.

BIOGRAPHICAL SKETCH

Sudeep Mandal was born on November 4, 1983 to Arun and Jayati Mandal in Bombay, India. He received his Bachelor of Technology degree in Engineering Physics from the Indian Institute of Technology Bombay in 2005. In the summer of his third year at IIT Bombay he joined Professor Gianaurelio Cuniberti's Molecular Computing research group at the University of Regensburg, Germany for a three month long research internship. Under the guidance of Professor Cuniberti and his post doctoral researcher, Rafael Gutierrez, Sudeep enjoyed a very fruitful three months over the course of which he worked on a theoretical model for charge transport in DNA. This research led to two peer reviewed publications. This was a pivotal experience for him and it strengthened his resolve to apply to a graduate program in Physics after the completion of his undergraduate degree. Sudeep joined the Applied Physics department at Cornell University in 2005, working with Professor David Erickson on optofluidic transport in liquid-core photonic crystal fibers. This project incited his interest in photonic crystals and their novel optical properties. Sudeep completed his doctorate in Applied Physics in 2010. He is currently continuing on as a postdoctoral researcher in Professor David Erickson's laboratory.

To my parents, my brother and my fiancée for all their love, patience and support

ACKNOWLEDGMENTS

First and foremost, I would like to thank my research advisor, Professor David Erickson, for introducing me to the field of optofluidics and for his constant support and faith in me over the course of my doctoral research. I am very grateful to him for his innovative ideas that helped launch my graduate research. I am also very thankful to him for mentoring me and for his invaluable feedback while preparing manuscripts and conference presentations. I sincerely thank my committee members, Professors Michal Lipson, Harold Craighead and Terrill Cool for their input and support for my research.

I would also like to sincerely thank Bradley Schmidt from Professor Michal Lipson's group who helped me get started with fabricating optical chips. His advice was invaluable and it certainly saved me many months of tedious work in the cleanroom. I am also extremely grateful to Carl Poitras, Arthur Nitkowski and Sasikanth Manipatruni in the Lipson group for helping me with my optical setup and for letting me pick their brains with many experimental and theoretical questions.

I am thankful to all my labmates for making my time in the lab enjoyable. In particular, I would like to thank Bernardo Cordovez, Mekala Krishnan, Aram Chung, and Mike Tolley for all their help and support. My heartfelt thanks go to Professor Julie Goddard with whom I collaborated extensively while she was a postdoctoral researcher in our lab.

I would like to thank my parents Arun Kanti Mandal and Jayati Mandal for their unconditional support and encouragement. Without their love and patience, I would never have been able to accomplish everything that I have achieved today. I would also like to thank my brother Ayan Mandal (dada) for being the best elder

brother I could ever ask for. I am forever grateful to him for his love, support and advice and for being there for me at all times. I am also very thankful to his wife, Rajni Mandal for her love and affection and for making me the world's best mango cupcakes every time I visit them. My most heartfelt thanks also go to Rajni's parents, Dr. Kandukuri Raman and Usha Raman for being like a second set of parents to me in Ithaca. I will forever be indebted to them for their love and affection and for all that they have done for me to make my stay in Ithaca an enjoyable one. Finally, I must thank my fiancée Meisha Morelli, without whom these last few years would have been much harder to get through. I am truly fortunate to have her love and support which brighten up even the bleakest and gloomiest winter days in Ithaca.

This work was funded by the National Institute of Health, the Defense Advanced Research Projects Agency, and the Nanobiotechnology Center.

TABLE OF CONTENTS

LIST OF FIGURES

CHAPTER 1

INTRODUCTION*

1.1 Goals, Aims, Scope and Overview of the Thesis

There are two major goals of this thesis. The first is to develop and characterize a novel optical platform for performing highly multiplexed, label-free biosensing. My research on this front has led to the development of Nanoscale Optofluidic Sensor Arrays (NOSA) which is a resonant photonic crystal based optofluidic architecture capable of performing massively multiplexed detections while possessing the mass sensitivity to detect attogram levels of bound mass. The second major goal is to enable improved optical trapping and transport abilities over the current state-of-the-art by exploiting novel optical devices. These overall goals can be refined down to a series of specific aims, which will be the focus of this thesis.

- The development of a liquid core waveguiding structure so as to enable optical transport of microparticles over distances on the order of a few centimeters. (Chapter 2)
- The design, characterization and numerical analysis of a novel photonic architecture (NOSA) for performing highly sensitive and multiplexed biomolecular detections. (Chapter 3)
- The experimental demonstration of the NOSA architecture as a highly sensitive biosensor capable of detecting attogram levels of bound mass and performing numerous biomolecular detections in parallel. (Chapter 4)

* Section 1.3 is re-printed with kind permission from Springer Science Business Media: Erickson, D., Mandal, S., Cordovez, B., Yang, A., "Nanobiosensors: Optofluidic, electrical and mechanical approaches to biomolecular detection at the nanoscale." *Journal of Microfluidics and Nanofluidics*, **4**, 33-52 (2008).

- The demonstration of resonant photonic crystal optical traps for the trapping and handling of dielectric nanoparticles with an improvement of an order of magnitude over the current state-of-the-art in optical trapping techniques. (Chapter 5)

1.2 Photonic Crystals

Photonic crystals [I.1-2] are materials that exhibit a periodicity in their dielectric permittivity. This periodic variation in their material dielectric permittivity or refractive index imparts unique optical properties to them. Since their discovery in 1987 [I.1], there has been a vast amount of research in the field of photonic crystals. This has led to many fascinating advances in the field of photonics ranging from photonic crystal fibers [I.3], photonic crystal waveguides [I.4], ultra-high Q/V optical resonators [I.5-6], optical biosensors [I.7-8] and integrated light sources [I.9-10]. All of these advances have been enabled by the unique ability of photonic crystals to control and confine light.

1.2.1 Photonic Crystal Theory

As mentioned above, photonic crystals consist of materials possessing a periodic modulation in their dielectric permittivity. While a rigorous theoretical description of photonic crystals is outside the scope of this text, here, a more intuitive description of photonic crystals backed by numerical simulations that help explain photonic crystals and their relevance towards my research is provided. For a more detailed theoretical

analysis of photonic crystals, the reader is encouraged to refer to two excellent texts on this subject [I.11-12].

When an electromagnetic wave propagates through a periodic lattice, it is scattered at every lattice site within the material. To analyze the behavior of this electromagnetic wave in the periodic structure, it is possible to take into account the scattering from multiple sites and mathematically add up the resulting fields by carefully accounting for any phase differences between these scattered electromagnetic waves. In the case of photonic crystals, there is a band of frequencies or wavelengths of light which are not allowed to have any forward propagating waves within the periodic material. For these wavelengths, all the scattered waves interfere destructively with the incoming electromagnetic wave such that no forward propagating wave can exist within the bulk of the photonic crystal. As a result, any light that possesses a frequency within the photonic bandgap is completely reflected by the photonic crystal. On the other hand, light possessing frequencies outside the photonic bandgap can propagate through the periodic structure without scattering since the scattering cancels out coherently. Maxwell's equations in SI units are

$$\begin{aligned} \nabla \times \mathbf{E} &= -\frac{\partial \mathbf{B}}{\partial t} \qquad & \nabla \cdot \mathbf{D} &= \rho \\ \nabla \times \mathbf{H} &= \mathbf{J} + \frac{\partial \mathbf{D}}{\partial t} \qquad & \nabla \cdot \mathbf{B} &= 0 \end{aligned} \tag{1.1}$$

where **E** and **H** are the electric and magnetic fields respectively, **D** and **B** are the displacement and magnetic induction fields, and **J** and ρ are the current and free charge densities. As outlined in [I.11] we make the following assumptions: We assume that the electric field strengths are small enough so that we are in the linear regime and that the material is isotropic. In addition, we assume that the dielectric permittivity $\varepsilon(\mathrm{r})$ is purely real and positive and we also ignore any material dispersion.

The electric and magnetic fields can be represented as a set of Harmonic modes of the form

$$\begin{aligned}\mathbf{E}(\mathbf{r},t) &= \mathbf{E}(\mathbf{r})e^{-i\omega t} \\ \mathbf{H}(\mathbf{r},t) &= \mathbf{H}(\mathbf{r})e^{-i\omega t}\end{aligned} \tag{1.2}$$

such that the spatial field distribution or "Mode Profile" is separated from the time variance of the field. By using the two divergence equations given in Equation 1.1 and performing further simplification [I.11] we can obtain an equation for **H**(r) given by

$$\nabla \times \left(\frac{1}{\varepsilon(\mathbf{r})} \nabla \times \mathbf{H}(\mathbf{r}) \right) = \left(\frac{\omega}{c} \right)^2 \mathbf{H}(\mathbf{r}) \tag{1.3}$$

Equation 1.3 can be rewritten as

$$\Theta \mathbf{H}(\mathbf{r}) = \left(\frac{\omega}{c} \right)^2 \mathbf{H}(\mathbf{r}) \tag{1.4}$$

It is evident that Equation 1.4 represents an eigenvalue equation where Θ is a linear operator. In the case of photonic crystals that exhibit a periodicity in their dielectric permittivity we obtain the relation

$$\varepsilon(\mathbf{r} + \mathbf{R}) = \varepsilon(\mathbf{r}) \tag{1.5}$$

where **R** is the lattice vector of the periodic dielectric structure. Equations 1.4 and 1.5 are remarkably similar to the expression for the Hamiltonian of an electron in a crystalline conductor under the influence of a periodic potential [I.13] which is also an eigenvalue equation of the form:

$$H\psi = \left(\frac{-\hbar^2}{2m} + U(\mathbf{r}) \right) \psi = \Xi \psi \tag{1.6}$$

Here, H is the Hamiltonian, m is the mass of the electron, Ξ is the energy of the electron, ψ is the electron wavefunction and $U(\mathbf{r})$ is the periodic lattice potential such that

$$U(\mathbf{r}+\mathbf{R}) = U(\mathbf{r}) \tag{1.7}$$

Thus in exactly the same manner that a bandgap is generated when an electron moves within a crystalline conductor under the influence of a periodic potential, photons under the influence of a periodic variation in the material permittivity also encounter an optical bandgap comprising of a range of frequencies that are forbidden within the photonic crystal. To calculate the true bandgap of photonic crystal geometries, it is necessary to utilize numerical simulations to iteratively solve Equation 1.4 so as to obtain a plot of the dispersion relation for a particular geometry.

Photonic crystals can be one, two or three-dimensional depending on whether the periodicity in the materials dielectric permittivity is in one, two or three dimensions. Figure 1.1 illustrates a one dimensional photonic crystal embedded in a silicon waveguide. Here, the photonic crystal consists of a periodic array of air holes that are etched in silicon.

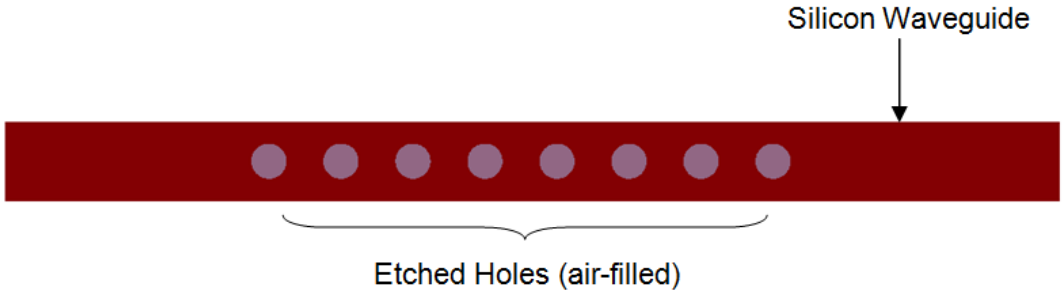

Figure 1.1: A one-dimensional (1-D) photonic crystal consisting of a periodic array of cylindrical holes etched in a Silicon Waveguide.

A two-dimensional finite difference time domain (FDTD) simulation was performed for the geometry shown in Figure 1.1 so as to analyze the behavior of this device over a broad range of wavelengths in the infrared. Figure 1.2(a) illustrates the transmission spectra for such a device. The U-shaped region in the center of the plot indicates a range of wavelengths that are not allowed to propagate through the photonic crystal structure (Figure 1.2 (c)). This corresponds to the photonic bandgap. As is evident, all light within the photonic bandgap is completely reflected back. In addition, we can see that light with a wavelength outside the photonic bandgap is allowed to be transmitted through the photonic crystal (Figure 1.2 (b)).

Thus, a photonic crystal behaves like a near-perfect mirror across a broad range of wavelengths that lie within the photonic bandgap. This property of photonic crystals affords a new tool for tailoring the flow of light within a material which has helped enable a variety of novel photonic devices as described in the following sections.

1.2.2 Photonic Crystals for Guiding and Confining Light

Light is typically confined and guided via total internal reflection. This occurs when light is incident on an interface between two mediums such that the refractive index of the material it is propagating in is higher than that of the other material. In addition, the angle of incidence of the incident beam has to exceed the critical angle for the material pair for it to be completely reflected at the interface. Conventional optical fibers rely on total internal reflection to confine and guide light over long distances. These fibers consist of a central cylindrical core with a higher refractive index than the surrounding concentric cladding. Light is coupled into the core of the fiber and it

continues to undergo successive total internal reflections at the core-cladding interface.

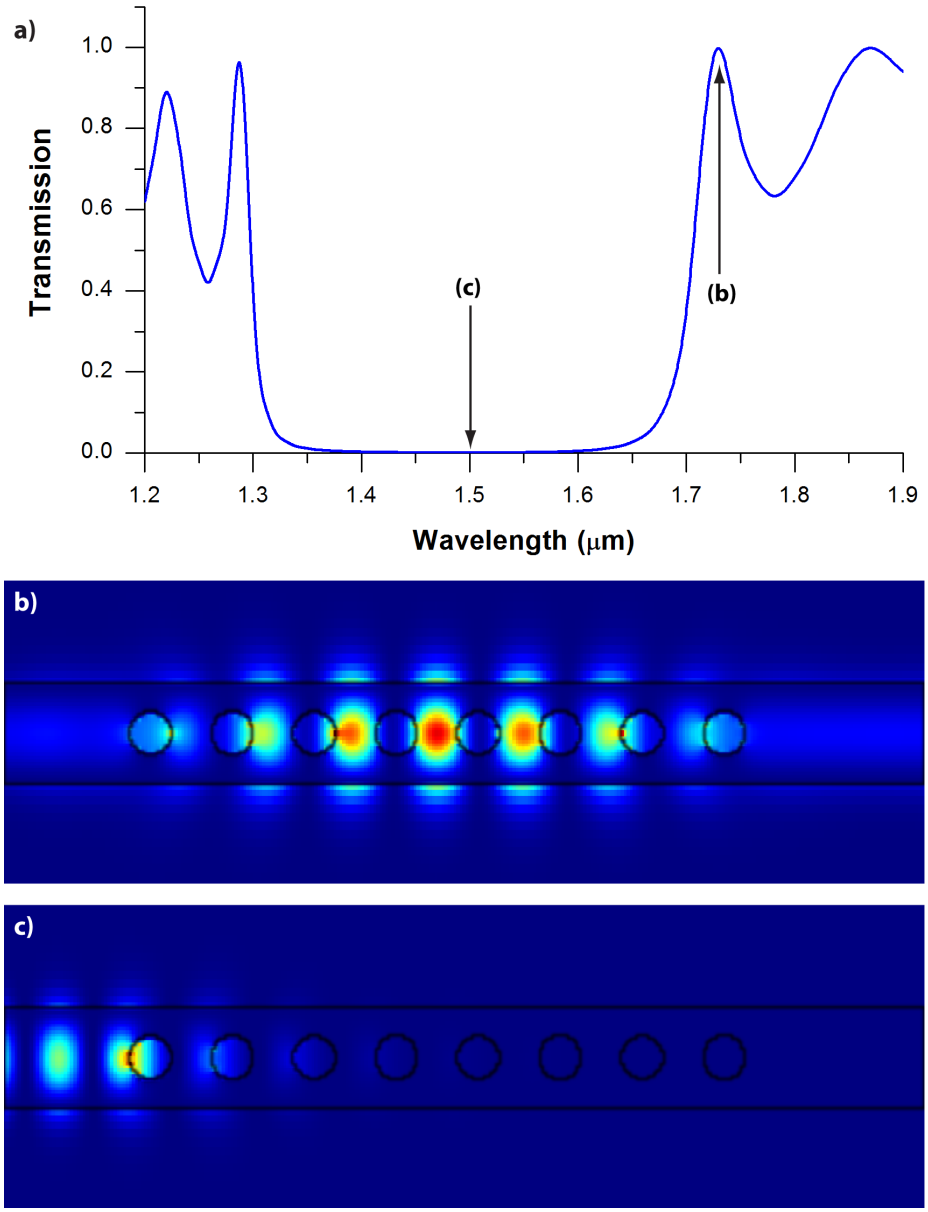

Figure 1.2: **(a)** Transmission spectrum for a silicon waveguide with an embedded 1-D photonic crystal consisting of 8 periodic cylinders that are etched into the silicon. The photonic bandgap is clearly visible and it extends from 1350nm to approximately 1700nm. **(b)** Field distribution for light outside the photonic bandgap (1730nm). It is evident that the light propagates through the periodic structure. **(c)** Field distribution for light in the photonic bandgap (1500nm) illustrating complete reflection by the PC.

However, this technique for guiding light has a few limitations. One such limitation is that total internal reflection can only occur when light is incident from a medium with a higher refractive index on an interface with another material with a lower refractive index. A consequence of this is that light can only be guided in a waveguide whose core has a higher refractive index than the cladding material. As will be discussed in Chapter 2, this gives rise to many technical challenges for designing a liquid core waveguide where its core is filled with water which posses a refractive index lower than that of the surrounding cladding material. The second disadvantage is the necessity for the incident light to have an angle of incidence larger than the Critical angle. If this is violated, it leads to losses in the system as the light is no longer reflected but instead undergoes refraction. This is especially challenging when the waveguiding structures are shrunk down in size since the material interfaces must be smooth with respect to the wavelength of incident light. In addition, bends in waveguides (especially sharp ones) can result in the guided optical modes being coupled into lossy radiation modes. Furthermore, when one tries to confine light to extremely small volumes (on the order of the wavelength of light), total internal reflection cannot be used to effectively contain the light.

Photonic Crystals are ideal candidates for overcoming the limitations imposed by total internal reflection. The photonic bandgap forbids any real solution for the existence of light within a photonic crystal possessing a frequency within the bandgap. This effect is independent of the angle of incidence of light, its polarization as well as the refractive index of the material in which the light is incident. It is important to note that the physical basis of this effect is completely different from total internal reflection.

If a defect is introduced within the periodic photonic crystal structure (for example, a missing lattice point, or a larger lattice spacing at a local point within the

photonic crystal) then it will locally modulate and change the bandstructure at the defect site. Such a local change in the bandstructure can give rise to a highly localized "defect" state [I.14] that corresponds to a mode that is allowed within the defect but is forbidden in the perfectly periodic photonic crystal structure surrounding it. As a result, defects in photonic crystals provide a novel way to strongly localize light without any losses. If the defect is in one dimension, i.e., a fixed point then it gives rise to a resonator. On the other hand, a defect in two dimensions gives rise to a waveguide. Figure 1.3(a) illustrates the transmission spectra for a 1-D photonic crystal microcavity that consists of a periodic 1-D photonic crystal lattice with a point defect introduced in the center of the cavity as shown in Figure 1.3(b).

Comparing Figure 1.3(a) with Figure 1.2(a), we observe a sharp peak in the transmission spectrum of the device located within the photonic bandgap. Thus, the presence of a defect in the photonic crystal cavity gives rise to a resonant mode within the bandgap of the photonic crystal. Figure 1.3(b) illustrates the optical field distribution for the resonant optical mode. It is evident that the resonant optical field is very strongly confined within extremely small volumes in these types of resonators. In addition, the optical field is amplified within the resonator giving rise to very strong local electric fields. The implications of these unique properties of photonic crystal resonators will be discussed in detail in Chapters 3, 4 and 5.

The ability of photonic crystals to completely reflect light possessing a wavelength within the photonic bandgap makes it an excellent candidate for creating a new class of light guiding structures that do not need to rely on total internal reflection to confine light. This has enabled novel designs for optical waveguides that were previously unachievable. For example, Figure 1.4 illustrates a 2-D photonic crystal waveguide with a 90 degree bend in the waveguide.

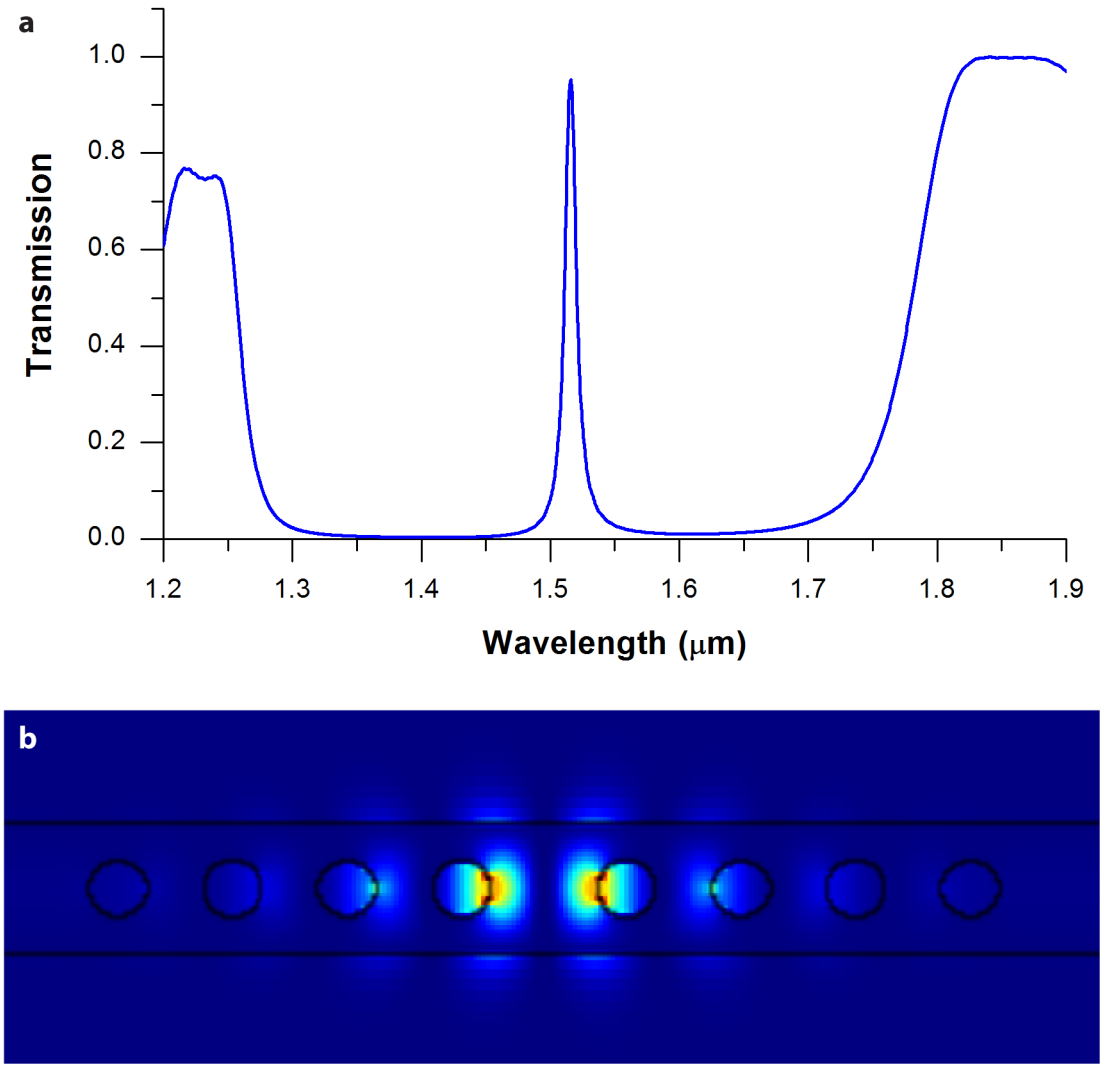

Figure 1.3: (a) Transmission spectra for a 1-D photonic crystal resonator comprising of a point defect within a regular 1-D photonic crystal lattice. In this example the defect consists of a larger hole-to-hole spacing at the defect site in comparison to the photonic crystal lattice spacing. **(b)** Field profile for a transverse-electric (TE) resonant mode within the cavity (λ = 1515 nm). It is evident that the light is amplified within the resonator. Additionally, the optical field is strongly confined in volumes on the order of the wavelength of light.

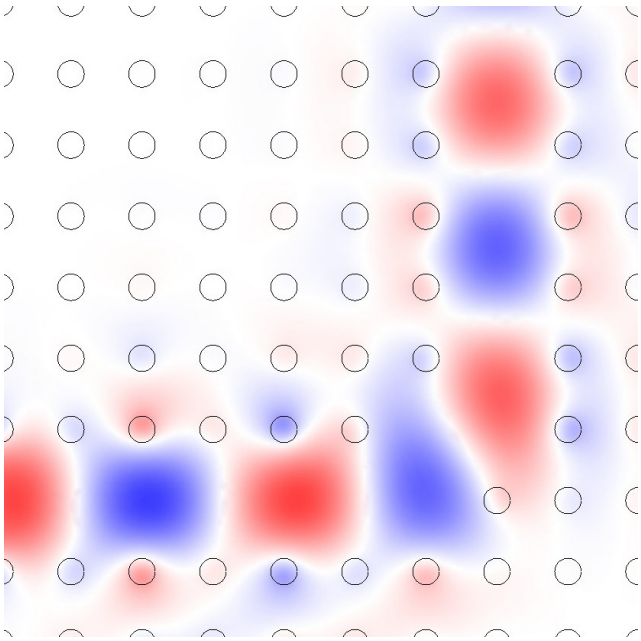

Figure 1.4: Numerical simulation for a photonic crystal waveguide with a 90 degree bend. The waveguide consists of a row of cylindrical GaAs posts that are removed from a periodic two dimensional lattice. The guided light (λ=1μm) lies within the photonic bandgap and as a result, is confined and guided within the waveguide.

The waveguide consists of a row of cylindrical Galium Arsenide (GaAs) posts that are removed from a 2-D photonic crystal lattice to form a waveguide for wavelengths of light within the photonic bandgap. The advantage of using the photonic bandgap for guiding light is abundantly clear since almost all the light continues to be guided after encountering the 90 degree bend in the photonic crystal waveguide. In the case of traditional total internal reflection based waveguides, bending losses become more and more prevalent as the radius of curvature of the bend is decreased. Thus, these types of waveguides are limited in their scope for the design of compact on-chip integrated photonic circuits. The ability to form exceptionally sharp bends in waveguides without losses is unique to photonic crystals and is of great interest to the integrated photonics community.

While the example above was that of a planar photonic crystal waveguide, there has also been significant research in the area of photonic crystal fibers or photonic bandgap fibers. These fibers, like traditional optical fibers, are constructed from silica and have similar diameters and material properties. Unlike traditional optical fibers however, photonic bandgap fibers consist of a central core that is surrounded by a concentric arrangement of periodic air capillaries which result in a photonic bandgap material forming the outer cladding of the fiber. Since the photonic bandgap effect is independent of the relative refractive index of the core and cladding materials, it allows the central core of the bandgap fiber to be hollow (i.e., with a refractive index lower than the cladding) without affecting the light guiding properties of the fiber. This ability to guide light in a hollow core over long distances and with low losses has revolutionized the field of optics. Since the optical fields are strongly confined within the hollow core, these fibers make excellent candidates for performing a variety of experiments in non-linear optics [I.15-16] where a large overlap between the optical field and the nonlinear material is crucial.

Thus, the unique properties of photonic crystals that enable them to confine and guide light in extremely small volumes has revolutionized the field of optics and has enabled many exciting technologies. In particular, photonic crystals are viewed as excellent candidates for designing extremely sensitive and multiplexable optical biosensors. The next section first introduces optical biosensors and their working principle and is followed by a brief overview of various optical biosensor designs. Finally the advantages of using a photonic crystal based structure as a biosensor will be discusses.

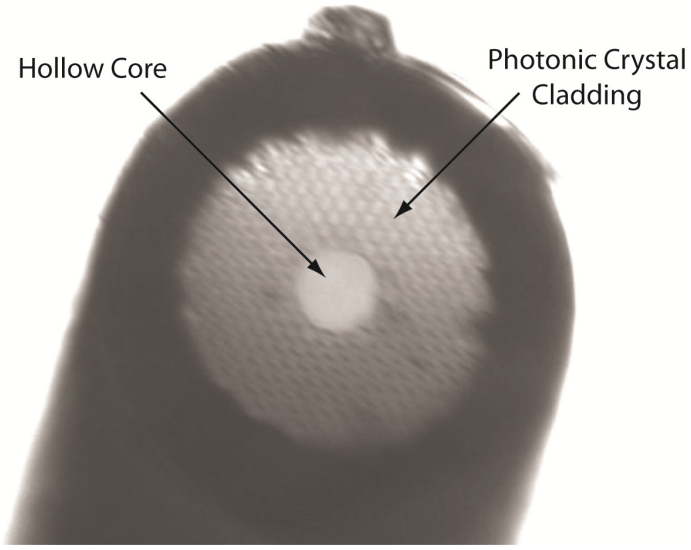

Figure 1.5: Micrograph of a hollow core photonic bandgap fiber. The fiber consists of a cylindrical hollow core that is surrounded by a periodic lattice of cylindrical air capillaries which form a photonic crystal cladding around the hollow fiber core.

1.3 Optical Biosensors

Optical biosensors have been of great interest to the biosensor community. The advantage of optical biosensors over other techniques is that the optical field is non-invasive and does not harm the bound target biomolecules at the sensor surface. Additionally, the optical signal is un-affected by surface charge conditions and solution pH, something that is a significant drawback in the case of nanowire based biosensors. Finally, by appropriately designing optical biosensors, it is possible to achieve a large degree of parallelism without sacrificing the sensitivity of the biosensor (see Chapters 3 and 4). Here, we will focus on techniques which exploit localized changes in the refractive index induced by biomolecular binding in the evanescent field of a dielectric structure. Furthermore, we will specifically overview

photonic crystal based devices and the advantages they afford towards creating ultra-sensitive optical biosensors.

1.3.1 Evanescent Field based Biosensors

While most of the optical energy is confined within the structure itself, solid core dielectric waveguides have an exponentially decaying tail of the guided optical mode, referred to as the evanescent field, that impinges a small distance (on the order of a hundred nanometers for most systems of interest here) into the surrounding medium. The majority of label-free optofluidic biosensors utilize this evanescent field to probe the surface of a sensing site for the presence of bound or absorbed analytes [I.17]. Binding of the target at the sensing site causes a change in the local refractive index in that region imparting a slight phase shift to the propagating optical mode. This simple phenomenon can be exploited via a number of different techniques to perform label-free optofluidic detection. In the following section we present an overview of these techniques while analyzing their advantages and limitations.

1.3.1.1 Interferometric based Techniques

Interferometry can be used to detect the phase difference between two collimated light beams of a coherent light source. Likely the simplest practical configuration for chip based integrated optofluidic biosensing is the Mach-Zehnder interferometer (MZI) such as that presented by Luff *et al.* [I.18]. Their design consisted of an input optical waveguide which split into two arms of equal length and then recombined to form the

output optical waveguide. One arm is referred to as the reference arm while a section of the other, sensing arm, is functionalized with the desired biorecognition agent. In the absence of any surface modifications to either of the arms, the light recombining at the output port remains in phase giving rise to constructive interference and maximal light intensity at the output port. When binding occurs at the surface of the sensing arm it changes the local refractive index and the resulting phase shift causes the output power to drop due to destructive interference effects. In the aforementioned work by Luff *et al.*, this phase shift was deduced by measuring the light intensity at the output waveguide. More recently an MZI biosensor using silicon nitride waveguides and standard CMOS processes was demonstrated [I.19]. It was used to detect the pesticide Carbaryl and was shown to have a refractive index limit of detection of around 10^{-5}. Others [I.20] have managed to push this limit to as low as 10^{-7} using the MZI configuration. While this technique is very sensitive, it is difficult to multiplex devices in a MZI configuration since each can consist of only one reference and one sensing arm. Another drawback is that the interaction length necessary for producing sufficient phase shifts is often on the order of a centimeter which, in comparison with some of the other techniques that will be discussed below, is very large. In a variant on the traditional approach, Lou *et al.* [I.21] recently proposed using silica nanowire waveguides in a MZI configuration. Their theoretical estimates indicate that the sensing site length can be decreased by an order of magnitude (to around 1 mm) to achieve similar refractive index sensitivity as the previously described works.

Brandenburg [I.22] demonstrated the use a Young's interferometer based sensor for refractive index measurements in liquids. Recently Ymeti *et al*. [I.23] extended this concept to perform multiplexed label-free biosensing. Their devices consist of a waveguide which guides monochromatic light coupled in from a laser source. This waveguide is split into two parallel waveguides by the means of a Y-

junction. Similar to the MZI sensor, one of the waveguides is functionalized with a biorecognition agent while the other acts as a reference waveguide. The light emerging from the output ends of the two waveguides is collected by a cylindrical lens and made incident on a charge coupled device (CCD) screen. By analyzing the interference pattern generated, the phase shift caused by binding events occurring on the surface of the sensing waveguide can be inferred. In their design they were able to resolve the interference patterns between four waveguides. Thus by using one waveguide as the reference, three different targets could be detected simultaneously. In that work, detection of herpes simplex virus 1 (HSV-1) was demonstrated and a device sensitivity of 10^{-7} refractive index units (RIU) which corresponded to a protein mass coverage of approximately 20 fg/mm^2 was reported. Although a certain level of multiplexing has been demonstrated, it is very hard to push beyond this limit with the Young interferometer design. As in the case of MZI sensors, interaction lengths in these sensors are on the order of a centimeter.

1.3.1.2 Resonant Cavity based Techniques

As stated above, one of the chief drawbacks of evanescent-wave sensing by interferometric techniques is the long interaction length of the sensing site, which requires a relatively large amount of bound mass to make an appreciable difference in the transduction signal. Resonant cavity sensors provide a way to overcome this disadvantage by shrinking the size of devices by orders of magnitude while still retaining similar device sensitivity. Microcavities sustaining whispering gallery modes (WGMs) [I.24-25] have been a popular choice for a label-free biosensing architecture. WGMs correspond to light being confined along a circular orbit along the edge of a

sphere, disk or cylinder type structure. Those wavelengths of light which after completing one revolution return in phase are sustained in the resonator while the other wavelengths die out due to interference effects. WGMs have been extensively studied in liquid droplets and fused silica spheres [I.26] both of which can have nearly atomic scale smoothness. In such microcavities optical losses are significantly lower than in other optical resonators and the Quality-factor (Q-factor) can exceed a hundred million [I.27-28]. Typically, light is evanescently coupled into these resonators using tapered fibers. The output spectrum observed at the end of the coupling fiber consists of a series of sharply peaked dips in transmission. Changes in the local refractive index at the surface of the resonator cause a slight perturbation to the resonance condition for the cavity, imparting a lateral shift to the peaks in the output spectrum.

This concept was used to demonstrate a highly sensitive refractometric sensor using a fused silica microsphere resonators [I.29]. The microspheres had a radius of 55 μm and the sensor had a limit of detection on the order of 10^{-7} RIU. For biosensing purposes these resonators can be coated with a suitable biorecognition agent. Vollmer *et al*. [I.30] demonstrated detection of bovine serum albumin (BSA) and streptavidin-biotin binding using such a design. Although these systems possess the properties to make them excellent candidates for ultra-sensitive biosensors, it can be difficult to control the physical parameters of these structures during fabrication as traditional lithographic techniques typically cannot be used to create on-chip cavities with such high Q-factors. This problem was solved by Armani *et al*. [I.27] who used a novel process to fabricate toroidal silica microresonators with a diameter of 120 μm on a chip. These structures had a Q-factor in excess of a hundred million. An extension of this work [I.31] demonstrated the use of these microresonators to detect heavy water concentration. Using an entirely different approach, Zhu *et al*. [I.32] have proposed a technique for on-capillary refractive index detections. The circular cross section of the

capillary acts as a ring resonator along which the input laser light remains confined. The interaction of the evanescent field with the contents of the liquid filled capillary allowed for non-invasive, on-capillary analysis.

While the techniques described above are well suited to perform highly sensitive detections, they lack robustness and are difficult to integrate in planar systems compatible with traditional microfluidics for performing multiplexed detections. Another drawback is that the entire surface of such devices has to be functionalized although the WGM interacts with a small fraction of this surface area. Planar microdisk [I.33-34] and microring resonator structures can overcome some of these difficulties as they can be easily be integrated on chip using standard semiconductor fabrication techniques (though the Q-factor is not nearly as high as those discussed above). Microring resonators consist of a ring waveguide which is adjacent to a bus waveguide. Light from a laser is coupled into the bus waveguide and this in turn evanescently couples into the ring resonator. As in the case of the silica microsphere resonators, resonance occurs for those wavelengths which are in phase after performing one round-trip around the ring and the spectrum at the output end of the bus waveguide consists of sharply peaked dips in transmission. Binding events along the surface of the microring increase the refractive index in the evanescent field, effectively lengthening the ring and causing the resonant peaks to red shift. Chao *et al*. [I.35] demonstrated polymer microring resonators of 45 μm radius having a Q-factor of 20,000. They were able to detect an effective refractive index change of 10^{-7} RIU and had a detection limit of approximately 250 pg/mm^2 mass coverage on the microring surface. While microring resonator sensors provide a robust architecture for potentially building highly multiplexed biosensors, their binding surface area is still reasonably large. For example in the Chao *et al.* device mentioned above the total

surface area or the ring resonator is ~ 6.5×10^{-4} mm^2 thus the mass limit of detection is ~160 fg.

1.3.2 Photonic Crystal Biosensors

Photonic crystals [I.2, 11] as described in the previous section, are composed of periodic dielectric structures. One of the features this periodicity gives rise to is a range of wavelengths which are not allowed to propagate within the structure, referred to as the photonic bandgap. The size of the bandgap and its position in the spectrum can be tuned by varying the refractive index contrast of the dielectric materials and/or the periodicity of the structure [I.36]. These properties of photonic crystals make them extremely useful in a number of applications, including biosensing. As an example, Skivesen *et al*. [I.37] demonstrated a photonic-crystal waveguide biosensor. This consisted of a silicon waveguide flanked on either side by a 2-D photonic crystal which caused light corresponding to the photonic bandgap to remain guided in the waveguide. As with the other optical devices, adsorption of proteins on the surface of the photonic crystal increased the local refractive index and shifted the bandgap. This was then detected by recording the spectrum at the waveguide output. 0.15 μM concentration of BSA, corresponding to a surface coverage of 6 ng/mm^2, was easily detected. While being a novel technique for performing label-free sensing, this device design is hard to multiplex since the bandgap prohibits transmission over a large range of wavelengths. In the experiment mentioned above, the device exhibited a relatively low solution phase limit of detection although the authors argue that there is still room for optimization.

Photonic crystal resonator devices posses very high Q-factors and are very sensitive to changes in the refractive index of their structural elements. They consist of a 1D or 2D photonic crystal with a defect in the crystal structure which acts as the resonant cavity. Chow *et al*. [I.38] demonstrated a 2-D photonic crystal microcavity consisting of a periodic lattice of holes in a silicon layer with a central hole defect. Changes in the refractive index in these holes shifted the resonant peak which allowed them to measure the refractive index of the surrounding liquid medium. More recently Lee and Fauchet [I.7] demonstrated a similar architecture with a Q factor well over 5000. They were able to detect BSA with a lower detection limit of a molecule monolayer with a total mass as small as 2.5 fg. Although it is difficult to perform multiplexed detections on a single waveguide using this design, it offers the unique advantage of performing highly sensitive detections in ultra-small volumes.

Chapter 3 and 4 details my research on a novel design for a photonic crystal biosensor that enables extremely low mass detections while simultaneously being capable of performing highly multiplexed detections.

1.4 Optical Forces

In 1970, Arthur Ashkin made a pioneering breakthrough [I.39] when he first demonstrated the ability to exert forces on dielectric microspheres in aqueous environments by utilizing electromagnetic radiation pressure. Since all electromagnetic fields possess an inherent electromagnetic momentum given by $\left(\mathbf{E}\times\mathbf{H}\right)/c^2$, the transfer of this momentum to particles in it's path via scattering, absorption and reflection can lead to the exertion of forces on these particles. In the case of a collimated laser beam, all the photons have an associated forward momentum in the direction of propagation of the beam. When this laser light is

incident upon a particle such as a dielectric microsphere that is transparent (i.e. it does not convert most of the incident light into heat) in a transparent aqueous environment, the light is scattered and refracted by the microsphere. This induced change in the direction of propagation of light implies a change in momentum for each photon. Thus, by the conservation of momentum the particle itself must undergo a change in momentum. Thus, the interaction of light with a transparent dielectric particle can induce optical forces on a particle. In his initial experiments, Ashkin demonstrated that the polystyrene microspheres were pushed along the direction of laser propagation in the aqueous chamber by a 'propulsion force'. In addition, he also noted that the beads would be pulled in towards the region of highest field intensity (i.e. the center of the Gaussian beam profile) while simultaneously being pushed in the direction of light propagation. Thus, by utilizing two co-axial counter propagating laser beams, he was able to demonstrate the stable all-optical trapping of polystyrene microspheres. In this particular configuration, the two counter propagating beams of light were necessary to nullify the axial propulsion force and stably trap particles in all three dimensions.

However, a few years later, Ashkin and his co-workers were able to overcome this design limitation by designing the first three dimensional single beam optical trap [I.40]. They realized that particles experience a 'gradient force' that pulls them towards regions of high field intensity. In the Rayleigh regime, this force is given as:

$$\mathbf{F}_{grad} = -\frac{n_m}{2}\alpha\nabla\mathbf{E}^2 \tag{1.8}$$

Where n_m is the refractive index of the surrounding medium, α is the polarizability of the dielectric particle and ∇E^2 is the gradient of the electric field intensity. Thus, from Equation 1.8, we see that the particle experiences a force that is proportional to the gradient in the electric field intensity and directed towards regions of high field intensity. Ashkin and his co-workers realized that by creating a large enough optical

field gradient in all three dimensions it would be possible to overcome the axial propulsion force and thus stably trap a particle in all three dimensions using a single beam. They demonstrated that by using high numerical aperture (NA) objectives to strongly focus the laser beam into a tight spot in all three dimensions they were able to stably trap several latex microspheres of differing sizes. This setup involving a high NA objective to optically trap particles was termed an optical tweezer. Since this original discovery by Ashkin, optical tweezers have revolutionized the fields of single molecule biology [I.41] and solid state physics [I.42].

One of the limitations with traditional optical tweezers is that all high NA objectives are diffraction limited. As a result, the minimum spot size to which the laser beam can be focused is on the order of the wavelength of light. Thus, this places a limit on the maximum field gradient that can be generated using such techniques which in turn places a lower bound on the size of particles that can be trapped stably in an aqueous environment. While the input optical power can be increased to enhance the trapping forces, limitations in the maximum power that can be output by continuous wave lasers as well as laser induced heating and damage at high powers prevents the ability to raise input powers of optical traps over a few Watts. Chapter 5, outlines my research on using resonant optical nanocavities for confining light beyond the diffraction limit so as to overcome these limitations. I will demonstrate that the amplification of the optical field in these resonant cavities combined with the exceptionally strong field gradients due to the strong confinement of light gives rise to extremely strong optical traps that are capable of trapping dielectric nanoparticles as small as 50-nm in diameter. This is an improvement in trap strength by several orders of magnitude over the current state-of-the-art.

REFERENCES

[I.1] Yablonovitch, E. Inhibited Spontaneous Emission in Solid-State Physics and Electronics. *Physical Review Letters* **58**, 2059 (1987).

[I.2] Joannopoulos, J. D., Villeneuve, P. R. & Fan, S. Photonic crystals: putting a new twist on light. *Nature* **386**, 143-149 (1997).

[I.3] Knight, J. C. Photonic crystal fibres. *Nature* **424**, 847-851 (2003).

[I.4] Chutinan, A. & Noda, S. Waveguides and waveguide bends in two-dimensional photonic crystal slabs. *Physical Review B* **62**, 4488 (2000).

[I.5] Akahane, Y., Asano, T., Song, B.-S. & Noda, S. High-Q photonic nanocavity in a two-dimensional photonic crystal. *Nature* **425**, 944-947 (2003).

[I.6] Song, B.-S., Noda, S., Asano, T. & Akahane, Y. Ultra-high-Q photonic double-heterostructure nanocavity. *Nature Materials* **4**, 207-210 (2005).

[I.7] Lee, M. R. & Fauchet, P. M. Two-dimensional silicon photonic crystal based biosensing platform for protein detection. *Optics Express* **15**, 4530-4535 (2007).

[I.8] Mandal, S. & Erickson, D. Nanoscale optofluidic sensor arrays. *Optics Express* **16**, 1623-1631 (2008).

[I.9] Wadsworth, W. *et al.* Supercontinuum and four-wave mixing with Q-switched pulses in endlessly single-mode photonic crystal fibres. *Optics Express* **12**, 299-309 (2004).

[I.10] Hirayama, H., Hamano, T. & Aoyagi, Y. Novel surface emitting laser diode using photonic band-gap crystal cavity. *Applied Physics Letters* **69**, 791-793 (1996).

[I.11] Joannopoulos, J. D., Meade, R. D. & Winn, J. W. *Photonic Crystals: Molding the Flow of Light*. (Princeton University Press, 1995).

[I.12] Lourtioz, J. et al. Photonic Crystals: Towards Nanoscale Photonic Devices. 2nd edn, (Springer, 2008).

[I.13] Ashcroft, N. W. & Mermin, N. D. *Solid State Physics*. (Brooks Cole, 1976).

[I.14] Foresi, J. S. *et al.* Photonic-bandgap microcavities in optical waveguides. *Nature* **390**, 143-145 (1997).

[I.15] Benabid, F., Knight, J. C., Antonopoulos, G. & Russell, P. S. J. Stimulated Raman Scattering in Hydrogen-Filled Hollow-Core Photonic Crystal Fiber. *Science* **298**, 399 (2002).

[I.16] Fuerbach, A., Steinvurzel, P., Bolger, J. A. & Eggleton, B. J. Nonlinear pulse propagation at zero dispersion wavelength in anti-resonant photonic crystal fibers. *Optics Express* **13**, 2977-2987 (2005).

[I.17] Marazuela, M. D. & Moreno-Bondi, M. C. Fiber-optic biosensors - an overview. *Analytical and Bioanalytical Chemistry* **372**, 664-682 (2002).

[I.18] Luff, B. J. *et al.* Integrated optical Mach-Zehnder biosensor. *Journal of Lightwave Technology* **16**, 583-592 (1998).

[I.19] Prieto, F. *et al.* An integrated optical interferometric nanodevice based on silicon technology for biosensor applications. *Nanotechnology* **14**, 907-912 (2003).

[I.20] Heideman, R. G. & Lambeck, P. V. Remote opto-chemical sensing with extreme sensitivity: design, fabrication and performance of a pigtailed integrated optical phase-modulated Mach-Zehnder interferometer system. *Sensors and Actuators B-Chemical* **61**, 100-127 (1999).

[I.21] Lou, J. Y., Tong, L. M. & Ye, Z. Z. Modeling of silica nanowires for optical sensing. *Optics Express* **13**, 2135-2140 (2005).

[I.22] Brandenburg, A. Differential refractometry by an integrated-optical Young interferometer. *Sensors and Actuators B-Chemical* **39**, 266-271 (1997).

[I.23] Ymeti, A. *et al.* Fast, ultrasensitive virus detection using a young interferometer sensor. *Nano Letters* **7**, 394-397 (2007).

[I.24] Matsko, A. B. & Ilchenko, V. S. Optical resonators with whispering-gallery modes - Part I: Basics. *Ieee Journal of Selected Topics in Quantum Electronics* **12**, 3-14 (2006).

[I.25] Ilchenko, V. S. & Matsko, A. B. Optical resonators with whispering-gallery modes - Part II: Applications. *Ieee Journal of Selected Topics in Quantum Electronics* **12**, 15-32 (2006).

[I.26] Arnold, S., Khoshsima, M., Teraoka, I., Holler, S. & Vollmer, F. Shift of whispering-gallery modes in microspheres by protein adsorption. *Optics Letters* **28**, 272-274 (2003).

[I.27] Armani, D. K., Kippenberg, T. J., Spillane, S. M. & Vahala, K. J. Ultra-high-Q toroid microcavity on a chip. *Nature* **421**, 925-928 (2003).

[I.28] Gorodetsky, M. L., Savchenkov, A. A. & Ilchenko, V. S. Ultimate Q of optical microsphere resonators. *Optics Letters* **21**, 453-455 (1996).

[I.29] Hanumegowda, N. M., Stica, C. J., Patel, B. C., White, I. & Fan, X. D. Refractometric sensors based on microsphere resonators. *Applied Physics Letters* **87** (2005).

[I.30] Vollmer, F. *et al.* Protein detection by optical shift of a resonant microcavity. *Applied Physics Letters* **80**, 4057-4059 (2002).

[I.31] Armani, A. M. & Vahala, K. J. Heavy water detection using ultra-high-Q microcavities. *Optics Letters* **31**, 1896-1898 (2006).

[I.32] Zhu, H. Y., White, I. M., Suter, J. D., Zourob, M. & Fan, X. D. Integrated refractive index optical ring resonator detector for capillary electrophoresis. *Analytical Chemistry* **79**, 930-937 (2007).

[I.33] Boyd, R. W. & Heebner, J. E. Sensitive disk resonator photonic biosensor. *Applied Optics* **40**, 5742-5747 (2001).

[I.34] Krioukov, E., Klunder, D. J. W., Driessen, A., Greve, J. & Otto, C. Sensor based on an integrated optical microcavity. *Optics Letters* **27**, 512-514 (2002).

[I.35] Chao, C. Y., Fung, W. & Guo, L. J. Polymer microring resonators for biochemical sensing applications. *Ieee Journal of Selected Topics in Quantum Electronics* **12**, 134-142 (2006).

[I.36] Erickson, D., Rockwood, T., Emery, T., Scherer, A. & Psaltis, D. Nanofluidic tuning of photonic crystal circuits. *Optics Letters* **31**, 59-61 (2006).

[I.37] Skivesen, N. *et al.* Photonic-crystal waveguide biosensor. *Optics Express* **15**, 3169-3176 (2007).

[I.38] Chow, E., Grot, A., Mirkarimi, L. W., Sigalas, M. & Girolami, G. Ultracompact biochemical sensor built with two-dimensional photonic crystal microcavity. *Optics Letters* **29**, 1093-1095 (2004).

[I.39] Ashkin, A. Acceleration and trapping of particles by radiation pressure. *Physical Review Letters* **24**, 156-159 (1970).

[I.40] Ashkin, A., Dziedzic, J. M., Bjorkholm, J. E. & Chu, S. Observation of a single-beam gradient force optical trap for dielectric particles. *Optics Letters* **11**, 288 (1986).

[I.41] Svoboda, K. & Block, S. M. Biological applications of optical forces. *Annual Review of Biophysics and Biomolecular Structure* **23**, 247-285 (1994).

[I.42] Chu, S. Laser Manipulation of Atoms and Particles. *Science* **253**, 861-866 (1991).

CHAPTER 2

OPTOFLUIDIC TRANSPORT IN LIQUID CORE WAVEGUIDING STRUCTURES*

2.1 Abstract

Here we introduce a method to achieve optofluidically [II.1] based particle transport through the use of liquid-core waveguiding structures. Optically driven transport of 3μm polystyrene particles through a liquid core photonic crystal fiber is demonstrated and the resulting velocity distribution is characterized. We also show that dielectric particles can form highly concentrated bands within the liquid core with negligible transport based dispersion. We anticipate that this approach could lay the groundwork for an innovative class of optically driven particle concentration and separation devices.

*Reprinted with permission from Mandal, S., Erickson D., "Optofluidic Transport in Liquid Core Waveguiding Structures", *Applied Physics Letters*, **90**, 18, 184103, 2007.

2.2 Introduction

The discovery that laser radiation could transfer its momentum to microscopic particles [II.2] and thus be used to manipulate them has led to many innovative applications for micro total analysis systems. The recent interest in Optofluidics [II.1] has led to a series of advanced implementations of various techniques to achieve all-optical control and sorting of particles into advanced and highly integrated microfluidic systems. They range from traditional optical tweezing [II.3], rotational manipulation of components based on form birefringence [II.4] to more recent electro-optic approaches such as that by Chiou et al. [II.5]. Recently an optical force based cell sorting technique [II.6] was developed wherein rare cells were directed into separate streams following the detection of a green fluorescent protein at the interrogation site using radiation pressure. Although a variety of complex manipulations have been demonstrated [II.7], most of them tend to be binary in nature, meaning that they can either trap or not trap a particle based on whether some trapping stability criteria is met [II.8]. A number of studies have extended these ideas to exploit the dependence of this trapping potential on the particle properties, enabling much more advanced and subtle operations. For example MacDonald et al. [II.9] demonstrated microfluidic sorting in a three dimensional optical lattice wherein particles of different sizes were sorted based on their differential affinity towards regions of high optical intensity. Imasaka and coworkers [II.10] provided the initial foundation for optically driven separation techniques which they termed optical chromatography. In these systems the extreme sensitivity of the scattering force to particle size and refractive index (as will be described in greater detail below) is exploited to separate out inhomogeneous species from an initially mixed state. Recently pathogen detection using optical chromatography was demonstrated in a

PDMS microfluidic system by Hart et al. [II.11]. They demonstrated the separation of two closely related bacteria Bacillus anthracis and Bacillus thurungiensis [II.12]. The non invasive nature of these optical techniques makes them well suited for bio-medical analysis devices.

At present one of the major limitations of these and other optically driven microfluidic systems is that the light-particle interaction length is relatively small, limited by the focal depth of the free space optics. Since the spatial separation of optically different targets is proportional to the length of this interaction, this limits the efficiency with which precise separations can be conducted. Using a loosely focused beam increases the interaction length but requires much larger optical power to perform manipulations on these length scales. In this work we demonstrate optofluidically driven transport in liquid core waveguiding structures. Since the light remains confined within the liquid core this gives direct access to the optical mode while increasing the light-particle interaction length by orders of magnitude. We have demonstrated that this allows for optically induced transport of microscopic particles over several centimeters, limited only by the optical power losses in the fiber.

Photonic crystal fibers (PCF) guide light based on a photonic bandgap effect [II.13]. In these devices a periodic lattice of air capillaries surrounds the core creating a photonic bandgap in the cladding which causes light of the wavelengths corresponding to this bandgap to be confined within the low-index core. Here we extend previous works demonstrating particle levitation in air-core PCFs [II.14] to liquid cores which enables bio-analytical functionality. To achieve light guidance in a liquid core PCF we require the refractive index of the liquid core to be higher than the effective refractive index of the holey cladding region. This causes the light coupled into the liquid core to undergo total internal reflection and thus remain confined within the liquid core. To create the desired refractive index contrast we introduce the liquid

in such a manner so that it penetrates into the hollow core without penetrating into the capillaries (using a technique which will be described below).

2.3 Experimental Results

A particle being guided through a liquid-core PCF experiences four forces, namely an axial scattering force, F_{scat}, a gradient force, F_{grad}, which can act in both the axial (due to loses along the length of the fiber) and radial direction (due to variations in the intensity profile), a gravitational force, F_{grav}, and viscous drag, F_{visc}. The origin of scattering and gradient forces lies in the change in momentum of the photons of the beam when they encounter the particle. The gradient force is proportional to the gradient of the field intensity resulting in particles being pushed towards regions of higher optical intensity. In the limit of a Rayleigh particle transported in the low Reynolds number regime it can be shown (by equating the scattering and gradient force relations from Ashkin *et al*. [II.15] with Stokes drag) that the particle velocity, v_p, is

$$v_p(z) = \frac{64\pi^4 a^5 n_m}{9\mu_m \lambda^4 c}\left(\frac{\left(n_p/n_m\right)^2 - 1}{\left(n_p/n_m\right)^2 + 2}\right)^2 I(r,\theta,z) + \frac{a^2}{3c\mu_m}\left(\frac{\left(n_p/n_m\right)^2 - 1}{\left(n_p/n_m\right)^2 + 2}\right)\frac{\partial I(r,\theta,z)}{\partial z} - \frac{m_p g}{6\pi\mu_m a} \tag{2.1}$$

where a is the particle radius, n_m and n_p is the medium and particle refractive indices, μ_m is viscosity, λ is the wavelength, c is the speed of light, m_p and g are the particle mass and gravitational acceleration respectively, and I is the local intensity incident on the particle which is in general a function of all three cylindrical coordinate directions. In Equation 2.1 the first term is representative of the scattering force, the second of the gradient and the third represents gravity which, for our system, is oriented opposite the

direction of the scattering force. From this expression it is evident that the propulsive velocity is extremely sensitive to the particle size ($v \propto a^5$ in the scattering dominated limit) which compares extremely favorably with other bio-analytical separation techniques (the nearest competitor being dielectrophoresis which can be shown to have an a^2 separation velocity dependence on particle size). From Equation 2.1 it is apparent that a transported particle should come to rest at a location z where the scattering force is balanced by the gradient (which acts downwards since $\partial I/\partial z < 0$ for a lossy fiber) and gravitational forces.

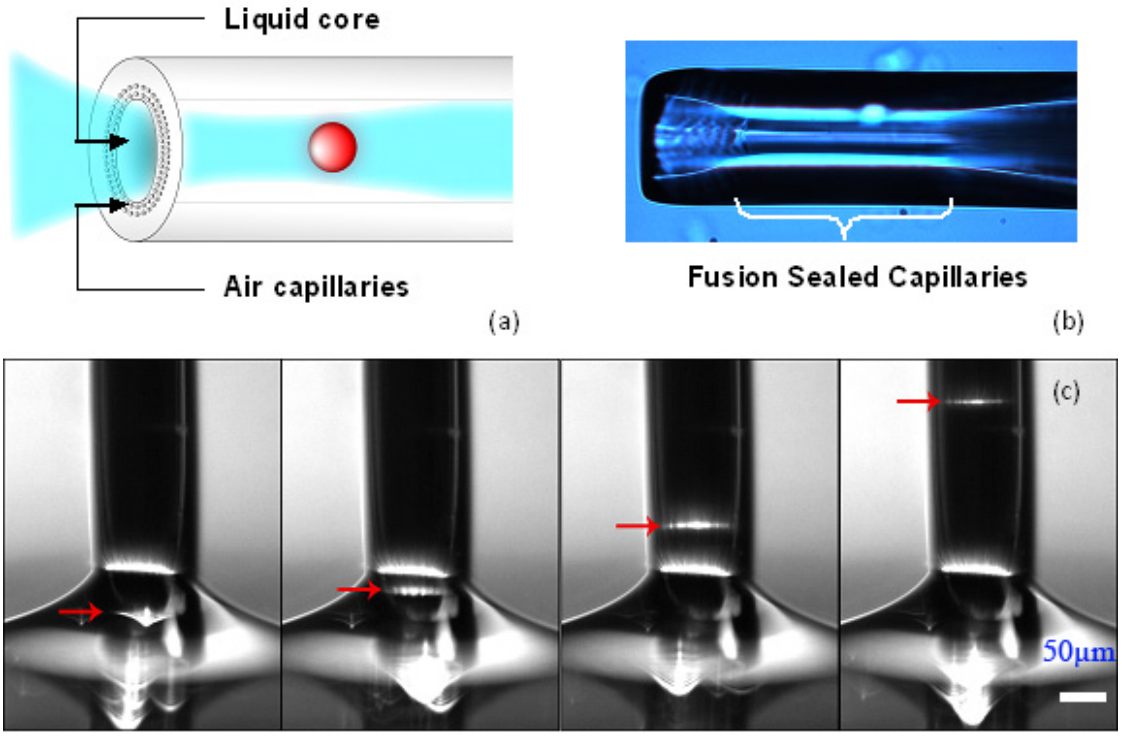

Figure 2.1: Optofluidic transport in a liquid core waveguiding structure. (a) Schematic illustrating optical excitation and transport of particles in liquid core of photonic crystal fiber. (b) Image of sealed air capillaries near inlet of fiber (c) Detail of optically induced transport of 3µm polystyrene beads in the liquid core optical fiber near the inlet. Red arrow tracks a 3µm bead. Successive frames are spaced by 1s.

In the experiments conducted here we used a 20μm diameter core Hollow-core PCF (Crystal Fiber, HC19-1550-01) as shown in Figure 2.1. To selectively fill the hollow core with liquid we close the capillary ends at the fiber mouth while leaving the core open. To achieve this we evaluated UV curing [II.16] and fusion splicing techniques [II.17]. The latter technique (which was used here) was found more reliable. High temperatures during the fusion process cause the small capillaries to collapse into each other, while the central core remains largely unaffected due to its larger diameter. A 488nm argon-ion laser beam is made incident on a 4x microscope objective to couple it into the fiber. The PCF is dipped in a glass container filled with a dilute aqueous solution of 3μm fluorescent polystyrene beads. A 40x objective at the other end of the fiber is used to image the near field pattern of the emerging laser beam. This is required to ensure that the light is being coupled into the core as slight misalignments can lead to light coupling into the silica cladding. A CCD camera with an attached microscope objective is used to image particles rising up the immersed tip of the fiber. Initially the fiber end was dipped in DI water and the fiber was aligned so as to couple light into it. Once proper light guidance through the liquid filled core was confirmed, small quantities of 3μm fluorescing polystyrene particles were introduced into the water. As is shown in Figure 2.1, particles in the path of the 488nm laser beam were pushed axially upwards through the fiber end. The ultimate travel distance of the particles was strongly dependent on the quality of the optical coupling. In some cases we were able to transport particles over distances of greater than 2cm with a laser excitation power of 210mW (measured at the laser output).

To characterize the transport dynamics of the system a series of velocity measurements were performed in a different experiment as shown in Figure 2.2. The excitation laser power measured directly at the laser output was 120mW. These measurements were made approximately 100μm from the mouth of the fiber. As can

be seen the data set shows a near normal distribution in the velocity frequency centered around a median value of 70µm/s. Care was taken to ensure that the suspending fluid was quiescent during these measurements and thus the non-uniform distribution could not be the result of a parabolic flow profile bias, resulting from an induced pressure. The liquid-core PCF is multi-moded due to the large difference in refractive index between the core and cladding. Considerable mode hopping due to the liquid core and the particles propagating through the core was observed. We expect this mode hopping to be responsible for the measured velocity distribution.

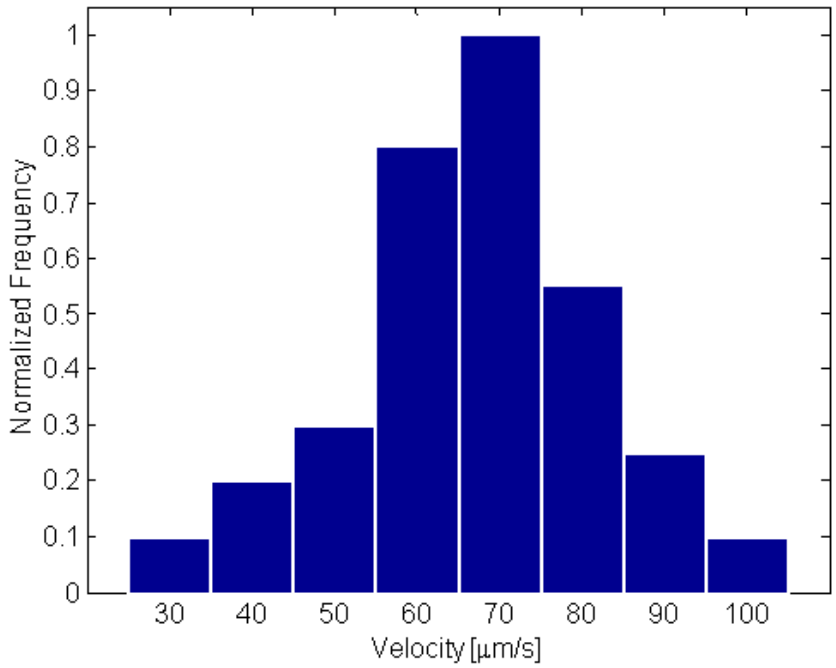

Figure 2.2: Experimentally measured particle velocity distribution. Transport velocities were measured for 3µm beads. As can be seen the velocity distribution showed a near normal distribution centered around 70µm/s.

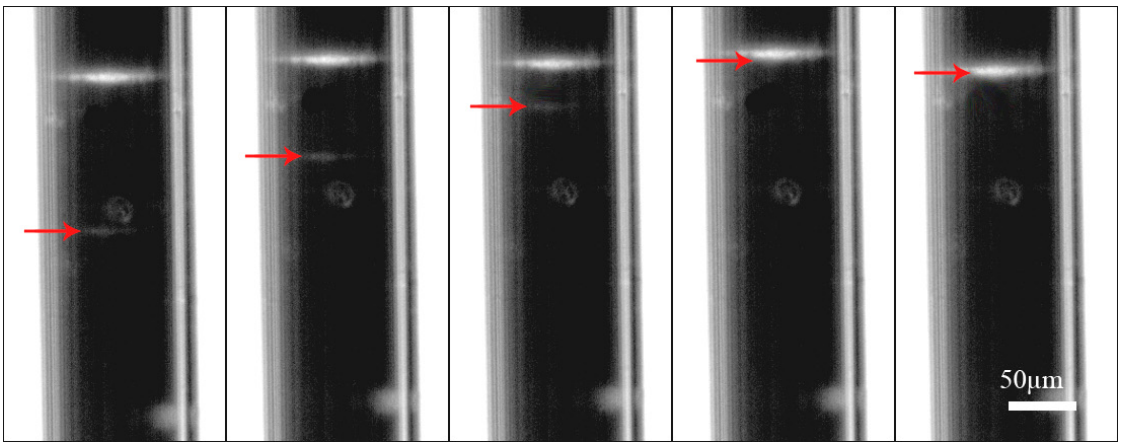

Figure 2.3: Formation of stable "floating bands" in liquid core. Demonstration of the concentration of particles into a stable band structure in a liquid core waveguiding structure. Red arrow tracks a 3µm bead. Successive frames are spaced by 66 ms and the input laser power was 210mW. As can be seen the concentrated band shows almost no transport based sample dispersion.

We have also observed the concentration of similar 3µm polystyrene particles into a distinct "floating bands" within the liquid core of the PCF. An example is as shown in Figure 2.3 which tracks a single particle being attracted into such a band. This banding was demonstrated at excitation powers as low as 50mW and it was observed that these bands can comprise of an extremely large number of particles (no upper limit was detected here). The axial resting place of the floating band was shown to rise with increasing incident power and vice versa. As mentioned earlier, at a particular height the axial scattering force is exactly balanced by the weight of the particle and loss induced gradient force. As can be seen in Figure 2.3 the observed bands are highly compact, exhibiting very little axial dispersion (spreading) which is counterintuitive given the spread in the transport velocity shown in Figure 2.2. Mode hopping was also observed to vary the absolute location of the band along the transport axis, but did not result in any observable dispersion. We believe that this anti-dispersive concentrating effect results from a sharp localized drop in the field

intensity as a result of scattering at the band location. The resulting change in field intensity strongly enhances the local gradient force pulling particles into the formations while maintaining a strong scattering force acting from below.

2.4 Summary

Here we have illustrated an optofluidic technique for particle concentration and trapping. While others have demonstrated particle motion in photonic crystal fibres [II.14], our work demonstrates optical transport in a liquid-core waveguiding structure over long lengths, the spatial characterization of the transport velocities and the optically induced concentration of particles into discrete bands. The light-particle interaction length in our proposed technique is orders of magnitude larger than existing systems. This has great potential in optical chromatography systems for ultra precise particle separations as well as in performing fluidic particle transport without flow field manipulations.

This work was partially supported by the U.S. National Science Foundation through the Sensors and Sensor Networks program under grant NSF/CTS 0529045.

REFERENCES

[II.1] Psaltis, D., Quake, S. R. & Yang, C. H. Developing optofluidic technology through the fusion of microfluidics and optics. Nature 442, 381-386 (2006).

[II.2] Ashkin, A. Acceleration and trapping of particles by radiation pressure. Physical Review Letters 24, 156-159 (1970).

[II.3] Grier, D. G. A revolution in optical manipulation. Nature 424, 810-816 (2003).

[II.4] Neale, S. L., Macdonald, M. P., Dholakia, K. & Krauss, T. F. All-optical control of microfluidic components using form birefringence. Nature Materials 4, 530-533 (2005).

[II.5] Chiou, P. Y., Ohta, A. T. & Wu, M. C. Massively parallel manipulation of single cells and microparticles using optical images. Nature 436, 370-372 (2005).

[II.6] Wang, M. M. et al. Microfluidic sorting of mammalian cells by optical force switching. Nature Biotechnology 23, 83-87 (2005).

[II.7] Curtis, J. E., Koss, B. A. & Grier, D. G. Dynamic holographic optical tweezers. Optics Communications 207, 169-175 (2002).

[II.8] Ashkin, A. & Gordon, J. P. Stability of Radiation-Pressure Particle Traps - an Optical Earnshaw Theorem. Optics Letters 8, 511-513 (1983).

[II.9] MacDonald, M. P., Spalding, G. C. & Dholakia, K. Microfluidic sorting in an optical lattice. Nature 426, 421-424 (2003).

[II.10] Imasaka, T. Optical chromatography. A new tool for separation of particles. Analusis 26, M53-M55 (1998).

[II.11] Terray, A., Arnold, J. & Hart, S. J. Enhanced optical chromatography in a PDMS microfluidic system. Optics Express 13, 10406-10415 (2005).

[II.12] Hart, S. J., Terray, A., Leski, T. A., Arnold, J. & Stroud, R. Discovery of a significant optical chromatographic difference between spores of Bacillus anthracis and its close relative, Bacillus thuringiensis. Analytical Chemistry 78, 3221-3225 (2006).

[II.13] Knight, J. C. Photonic crystal fibres. Nature 424, 847-851 (2003).

[II.14] Benabid, F., Knight, J. C. & Russell, P. S. Particle levitation and guidance in hollow-core photonic crystal fiber. Optics Express 10, 1195-1203 (2002).

[II.15] Ashkin, A., Dziedzic, J. M., Bjorkholm, J. E. & Chu, S. Observation of a single-beam gradient force optical trap for dielectric particles. Optics Letters 11, 288 (1986).

[II.16] Nielsen, K., Noordegraaf, D., Sorensen, T., Bjarklev, A. & Hansen, T. P. Selective filling of photonic crystal fibres. Journal of Optics A: Pure and Applied Optics 7, L13-L20 (2005).

[II.17] Xiao, L. et al. Fabrication of selective injection microstructured optical fibers with a conventional fusion splicer. Optics Express 13, 9014-9022 (2005).

CHAPTER 3

NANOSCALE OPTOFLUIDIC SENSOR ARRAYS*

3.1 Abstract

In this paper we introduce Nanoscale Optofluidic Sensor Arrays (NOSAs), which are an optofluidic architecture for performing highly parallel, label free detection of biomolecular interactions in aqueous environments. The architecture is based on the use of arrays of 1D photonic crystal resonators which are evanescently coupled to a single bus waveguide. Each resonator has a slightly different cavity spacing and is shown to independently shift its resonant peak in response to changes in refractive index in the region surrounding its cavity. We demonstrate through numerical simulation that by confining biomolecular binding to this region, limits of detection on the order of tens of attograms (ag) are possible. Experimental results demonstrate a refractive index (RI) detection limit of $7x10^{-5}$ for this device. While other techniques such as SPR possess an equivalent RI detection limit, the advantage of this architecture lies in its potential for low mass limit of detection which is enabled by confining the size of the probed surface area.

* This chapter was previously published in Mandal, S. and Erickson, D., "Nanoscale optofluidic sensor arrays", *Optics Express*, **16**, 1623 (2008). © Optical Society of America. Reproduced by permission

3.2 Introduction

Optical techniques represent one of the most popular methods for performing sensitive and label free biomolecular detection. Broadly speaking the primary advantages of optical techniques over analogous mechanical or electrical label free methods [III.1] are: the relative ease with which devices can be fabricated and the broad range of fluids and environments in which they can be used (*e.g.* gas, water and serum). Though numerous different architectures have been developed (including interferometric sensors [III.2-3], resonant cavity sensors [III.4-5], whispering gallery mode sensors [III.6-7], surface plasma resonance (SPR) sensors [III.8] and photonic crystal based sensors [III.9-10]) in nearly all cases detection is based on measuring the change in refractive index that results when solution phase targets bind with complimentary probes that have been predeposited on the surface. Of all the different architectures that have been developed, planar photonic crystal sensors [III.11] are particularly interesting not because they are necessarily more sensitive to intensive or bulk properties (*e.g.* refractive index) but rather because the small interrogation volume makes them more sensitive to extensive properties (*e.g.* total bound mass). High quality factor 1D and 2D photonic-bandgap microcavity [III.12] sensors amplify this effect by shrinking the probed volume to the size of the optical cavity, which can be on the order of λ^3. Since the mode volume is so small the total amount of mass required to result in a measureable change in the refractive index (reflected by a change in the wavelength of the resonant peak) can also be very small. Examples of such systems include that of Lee *et al.* [III.9] who demonstrated a 2D resonant photonic crystal based biosensor for protein detection and Schmidt *et al.* [III.13] who demonstrated a nanoparticle sensing in a unique 1D cavity.

The drawback of these designs is that the large photonic bandgap prohibits having multiple sensing sites along the same waveguide. As such the number of targets which can be screened for at once is relatively small. Ideally one would like an architecture that combines the high quality factor, low mode volume sensing of the above devices with the ability to multiplex multiple detection sites along a single waveguide.

Here we describe a new paradigm for optofluidic [III.14-15] sensing that allows us to overcome this limitation, which we refer to as Nanoscale Optofluidic Sensor Arrays (NOSA). As will be demonstrated, this technique has potentially tens of attograms level detection sensitivity without the need for target labeling, while allowing for two dimensional multiplexing at reaction site densities at least equivalent to that found in a standard microarray. While the bulk refractive index sensitivity of this device is lower than that of techniques such as SPR, its chief advantage lies in the ability to confine the size of the probed volume thus allowing for a low mass limit of detection. As such our device should be able to detect rarer targets in a given sample size since a smaller number of them are required to impart a measurable change. Each sensing site consists of an evanescently coupled 1D photonic crystal resonator that can be individually addressed via a microfluidic architecture which is bonded on top of the optical chip. In this paper we describe the device design, theoretical simulations, fabrication methods and experimental device characterizations demonstrating the working of this architecture. The numerical simulations confirm our experimental results and are used to analyze the suitability of our NOSA platform as a sensitive nucleic acid sensor. To illustrate the working of our device we flow aqueous solutions possessing different refractive indices through microfluidic channels that target the resonators. We determine the sensitivity of our devices by observing the shift in the

resonant wavelength of the resonators as a function of the change in refractive index of the fluid.

3.3 Device Design

Figure 3.1(a) shows a 3D illustration of our sensor design. It consists of a silicon (Si) waveguide with a 1D photonic crystal micro-cavity (side resonator) that lies adjacent to the waveguide. The side resonator consists of a central defect cavity with 8 holes on either side which form the 1-D photonic crystal. The Si waveguide was designed to be 450 nm wide and 250 nm tall to make it single mode. The low index silicon dioxide (SiO_2) layer which lies beneath the high index Si waveguide helps confine the light within the waveguide core, preventing optical losses into the lower substrate. Figure 3.1(b) shows the fundamental quasi-TE mode for this waveguide geometry.

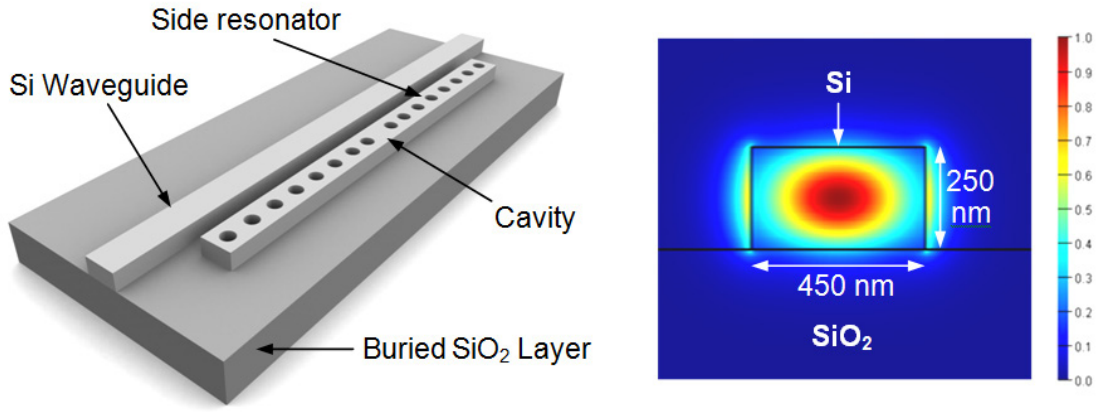

Figure 3.1: (a) 3D illustration of a sensing element in our sensor design. It consists of a 1D photonic crystal micro-cavity which is evanescently coupled to a Si waveguide. (b) The electric field profile for the fundamental TE mode propagating through an air-clad Si waveguide on SiO_2.

A central defect cavity in the 1D photonic crystal gives rise to a defect state in the photonic bandgap. By varying this defect cavity spacing we can tune the resonant wavelength of this state across the bandgap of the side resonator. Analogous to a ring resonator [III.16] light corresponding to the resonant wavelength couples evanescently into the side resonator and is sustained within it. This results in a dip in the output spectrum of the waveguide at the resonant wavelength. Because the resonant structures lie to the side of the waveguide the bandgap does not interfere with the light transmission outside of that which lies in the resonant peak. Thus our unique design allows multiplexing along a single waveguide by placement of a large number of side resonators along the waveguide, each of which is fabricated to have a slightly different resonant wavelength.

Using Bloch-mode engineering concepts, Velha *et al*. [III.17] have experimentally achieved Q-factors as high as 8900 with such 1D resonant cavities. We performed finite difference time domain (FDTD) simulations to study and optimize our device design using a commercial FDTD software package (FDTD Solutions – Lumerical). Here we increased the Q-factor of our device by changing the spacing of the two innermost holes outwards to achieve Q-factors over 2000 for a resonator with 8 holes on either side of the cavity. While more extensive simulations could have been performed to design devices possessing higher Q-factors, a Q-factor of around 2000 is more than sufficient to illustrate the device concept and working principle. The holes in the side resonator were 200 nm in diameter and the lattice spacing of the 1D lattice was 390 nm. The innermost holes were shifted outwards, away from the cavity center by 39 nm.

Figure 3.2(a) shows the steady state electric field distribution for the resonant wavelength within the device. As can be seen, there is a significant amount of light amplification within the resonator. Relative to the evanescent field at the side walls of

the resonator, we observe the inner most holes of the side resonator to have a stronger optical field. This causes the resonators to be very sensitive to refractive index changes within these holes due to the large degree of light-matter interaction inside them.

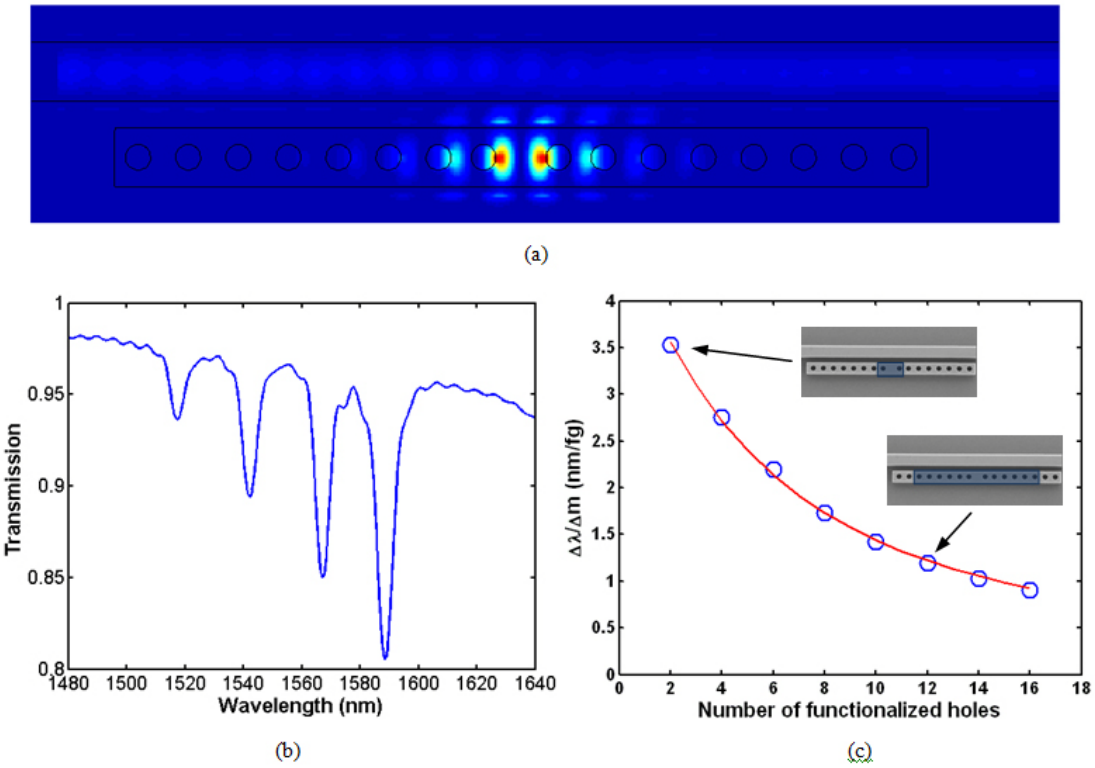

Figure 3.2: (a) Steady state electric field distribution for the resonant wavelength (b) FDTD simulation showing the output spectrum for a device consisting of a waveguide with four evanescently coupled side cavities adjacent to it. Here each resonator consists of a cavity with four holes on either side. (c) FDTD simulation showing the mass sensitivity of the device plotted as a function of the number of functionalized holes. The blue circles indicate the sensitivity values calculated from the simulations. The red curve shows a least-squares fit using an analytical model for the device sensitivity which is described below.

Figure 3.2(b) is a FDTD simulation which demonstrates the typical output spectrum of a device with four evanescently coupled resonators. In this particular simulation each resonator consists of four holes on either side of the central cavity as

opposed to eight which results in a lower Q-factor than that discussed above. The inherent advantage of our sensor design is apparent from this graph. By tuning the input light across a range of wavelengths and having a large number of side resonators (each designed to possess a unique resonant wavelength within this tunable range) placed alongside a single waveguide, the output spectrum will consist of a large number of sharp dips in an otherwise flat spectrum wherein each dip corresponds uniquely to one of the resonators. Any shift in one of the resonances indicates a change in the refractive index of the local environment around the corresponding resonator. In this manner a large number of detections can be done in parallel on a single waveguide (estimates of the maximum number is discussed in the experimental section).

It is important to note that for applications such as biosensing, the device does not measure changes in the bulk refractive index of the surrounding medium, but rather respond to local changes in the refractive index at the surface of the sensor. As a result, the magnitude of the resonant shift will be dependent on a combination of factors such as the biolayer thickness and the effective change in refractive index of the bound targets. To model this here, we performed detailed 3D FDTD simulations wherein we studied the sensitivity of this sensor design and determined how to achieve the lowest mass limit of detection using this architecture. We assumed that the resonator was initially functionalized by a 50 nm thick single stranded DNA monolayer (ssDNA). When a detection event occurs, the complementary ssDNA strand of the target would hybridize with the functionalized capture probes forming double stranded DNA (dsDNA). The ssDNA monolayer and the dsDNA monolayer were assumed to possess refractive indices of 1.456 and 1.53 respectively and a binding density of 1.49 pmol/cm^2 [III.18]. The molecular weight of the nucleic acids used in our simulations is 57000 Daltons. We varied the number of holes being

functionalized to study the mass sensitivity of the device as a function of the number of functionalized holes. Simulations were performed for the cases of two holes (the innermost holes on either side of the cavity), four holes (the inner two holes on either side), and so forth, up to 16 holes (eight holes on either side) being functionalized with a ssDNA capture probe. We have calculated the term $\Delta\lambda/\Delta m$ in all these cases where $\Delta\lambda$ is the shift in the resonant wavelength of the device caused due to positive binding events resulting in the formation of dsDNA and Δm is the mass of the bound target. This $\Delta\lambda/\Delta m$ term is indicative of the mass sensitivity of the device. We use nucleic acids as our model species in this case due to the availability of data relating the change in local refractive index with surface concentration of immobilized probes and bound targets. For very large nucleic acid targets however there may be steric effects which preclude transport into the resonator holes potentially degrading the overall sensitivity. For smaller nucleic acids or antibody/antigen systems we do not expect this to be a problem.

The blue circles in Figure 3.2(c) show the calculated sensitivity, $\Delta\lambda/\Delta m$ for these different cases. As can be seen, the innermost holes are the most sensitive to any refractive index changes in the local environment as opposed to the holes that are further away from the cavity. These results can be explained by noting that in Figure 3.2(a) the evanescent field is largest inside the innermost holes and decreases inside holes that are situated further away from the cavity. This is important to note because targeting only the inner most holes for functionalization allows for the lowest possible limit of mass detection for this device. In the case where only the inner two holes are functionalized we find that the resonance shifts by 3.5 nm when 1 femtogram of DNA binds to the resonator. Therefore a mass change of 10 attograms would result in a mass surface density of 0.84 nanogram/cm^2 and an approximate shift of 10^{-2} nm which can be experimentally detected.

The mass sensitivity $\Delta\lambda/\Delta m$ can be expressed by the following equation:

$$\frac{\Delta\lambda}{\Delta m} = \frac{\Delta n}{\frac{\Delta m}{A}} \times \left[\frac{\Delta\lambda}{\Delta n} \times \frac{1}{A} \right] \tag{3.1}$$

Here Δn is the change in refractive index induced by binding events at the sensing site and A is the area of the sensor that is functionalized with probe molecules. To maximize the mass sensitivity we try to optimize the terms in the RHS of Equation 3.1 . We observe that the first term $\Delta n/(\Delta m/A)$ which represents the change in refractive index induced by the binding of mass, Δm per unit area is purely dependent on the optical properties of the bound target and the functionalization surface chemistry and thus cannot be increased by any other means. The $\Delta\lambda/\Delta n$ term is a measure of the refractive index sensitivity of the device.

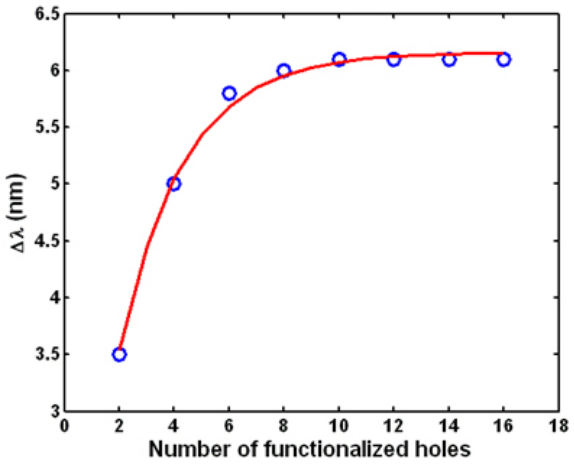

Figure 3.3: Plot illustrating the dependence of the shift in resonant wavelength of a resonator on the number of functionalized holes. The blue holes indicate the data obtained from 3D FDTD simulations. Red curve is a best-fit curve of the form $a(1-e^{-bN})$ where a and b are arbitrary constants. The values of a and b used here are 6.159 nm and 0.4273 respectively.

Figure 3.3 is a plot illustrating the dependence of the wavelength shift $\Delta\lambda$ on the number of functionalized holes N. We observe that an exponential function of the form $a(1-e^{-bN})$ (shown in red), where a and b are arbitrary constants approximates this dependency quite well. It should be noted that the area A is directly proportional to the number of functionalized holes N. Thus taking all of the above into consideration we can express Equation 3.1 analytically as:

$$\frac{\Delta\lambda}{\Delta m} = \frac{\alpha\left(1-e^{-\beta N}\right)}{N} \tag{3.2}$$

where α and β are arbitrary constants. From the form of Equation 3.2 we observe that the mass sensitivity increases if we lower the number of holes N, that are functionalized. Equation 3.2 is used to fit the red curve in Figure 3.2(c) where the values of α and β are 14.96 nm/fg and 0.3238 respectively. Thus, this analytical expression shows good agreement with the FDTD simulation results and helps us to understand that the mass sensitivity of the device increases with a decrease in the number of functionalized holes. To reiterate, although the resonant shift is larger for the greater number of holes which are functionalized, more bound mass is required to impart this change. Thus increasing the number of holes which are functionalized tends to negatively affect the mass limit of detection.

3.4 Device Fabrication and Experimental Setup

To demonstrate the nanoscale optofluidic sensor array architecture and provide some validation of our numerical technique we fabricated a number of devices and performed a series of experimental characterization experiments. The devices were

fabricated on SOI wafers having a device thickness of 250 nm. XR-1541 e-beam resist (HSQ, Dow-Corning Corporation) was spun on the wafer and the devices were patterned using a Leica VB6-HR electron beam lithography system. The Si device layer was then etched vertically down using a Chlorine based inductively coupled plasma etching system. The remaining XR-1541 was dissolved in a dilute 100:1 HF solution. To increase coupling efficiencies nanotapers [III.19] were fabricated and a layer of hard baked SU-8 (Microchem) photoresist was used as a cladding to the nanotapers. Following this the wafer was diced along the input and output ends of the waveguides.

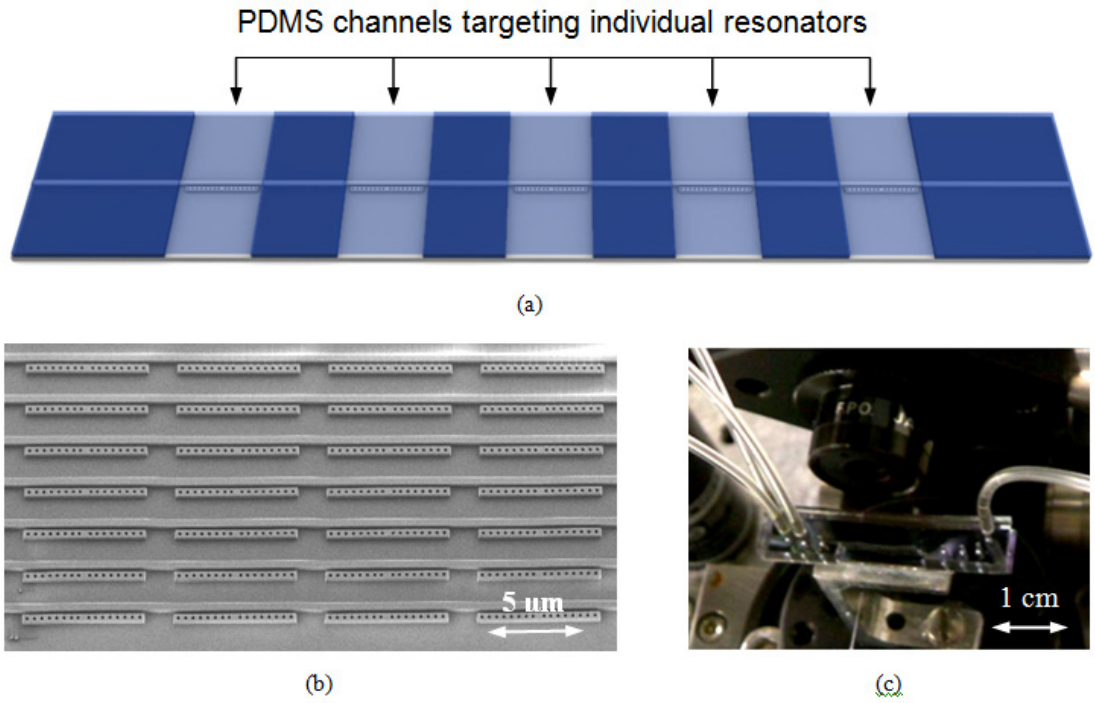

Figure 3.4: (a) 3D schematic showing a PDMS channel running across the side resonator. This channel allows the fluidic targeting of individual sensing sites (b) SEM of a NOSA device. It illustrates how this architecture is capable of two dimensional multiplexing, thus affording a large degree of parallelism. (c) Actual NOSA chip with an aligned PDMS fluidic layer on top.

The top fluidic architecture was fabricated using a soft lithography technique with polydimethylsiloxane (PDMS) [III.20] which is a flexible polymer. SU-8 photoresist was patterned and hardbaked on a silicon wafer to form the fluidic mold which consisted of individual channels for targeting each of the resonators separately. PDMS was poured on top of the mold and allowed to bake at 80°C for 2 hours. Following this the PDMS was carefully peeled off the mold to obtain the PDMS fluidic layer. Holes were punched into the fluidic reservoirs and then the PDMS layer was plasma cleaned for a few seconds along with the chip. The PDMS was then bonded irreversibly to the chip with the channels running orthogonal to the waveguide, with each channel aligned to one of the side resonators along the waveguide (Figure 3.4(a)). Precise alignment of the channels with the resonators during bonding was ensured by using a modified overhead optical microscope setup. The bonded chip was left in an oven at 80°C for 10 hours to increase the bonding strength between the fluidic layer and the substrate. Fluids were flown through the channels using a digital pneumatic manifold setup (Fluidigm Corp). Figure 3.4(b) shows an SEM image of the NOSA.

We used an Ando AQ4321D Tunable Laser Source, which is tunable across the 1520nm to 1620nm spectrum. A lensed fiber is used to couple light from the laser into the chip. The fiber is clamped onto a three axis stage so that it can be positioned precisely for coupling light into the waveguides. The chip is mounted on another 3-axis stage. At the output end of the waveguide a lens is used to collect and collimate the output light from the waveguide into a photodetector. The output end of the waveguide is laterally shifted from the input end by 2mm to prevent directly scattered light from the input end reaching the detector. A polarizer is placed between the lens and the detector to select only the TE component of light emerging from the waveguide. Figure 3.4(c) shows the NOSA chip with a bonded PDMS fluidic layer.

3.5 Experimental Results

A typical output spectrum of a waveguide with five resonators of differing sizes is shown in Figure 3.5. In this case all five resonators had water as the surrounding medium. As can be seen, each resonator contributes a sharp dip to the output spectrum of the device. We observe that each 1D resonator possesses a large Q-factor varying from 1500 to 3000 and a full width at half maxima of less than a nanometer. This is important for two reasons. Firstly, higher Q-factors make it easier to detect very small shifts in the resonances. Equally as important however, is that as the peaks get narrower it allows us to pack the output spectrum with a larger number of closely spaced dips and thus allows us to multiplex a larger number of resonators onto a single waveguide. Given the operational range of a standard 1550nm tunable laser (such as the one used here) and the linewidth of the observed resonances, we expect that 50 such side resonators could be incorporated on a single waveguide allowing us to perform as many as 50 detections in parallel on a single waveguide. In addition, as mentioned before, the Q-factors of these resonators can be significantly enhanced by optimizing the device geometry to allow an even larger degree of multiplexing.

To investigate the RI sensitivity of the device we performed an experiment wherein one of the resonators was targeted by a fluidic channel which was initially filled with water. When a higher refractive index solution of Calcium Chloride is passed through the channel it changes the resonance condition of the resonator and pushes its unique resonant dip towards the red end of the spectrum as shown in Figure 3.6(a). It is important to note that the other peaks are unaffected. In this way one can confirm positive binding events occurring at any one of the resonators since only their corresponding resonances would show a shift in the output spectrum. Resonators with no binding occurring will show no shift in their output resonance.

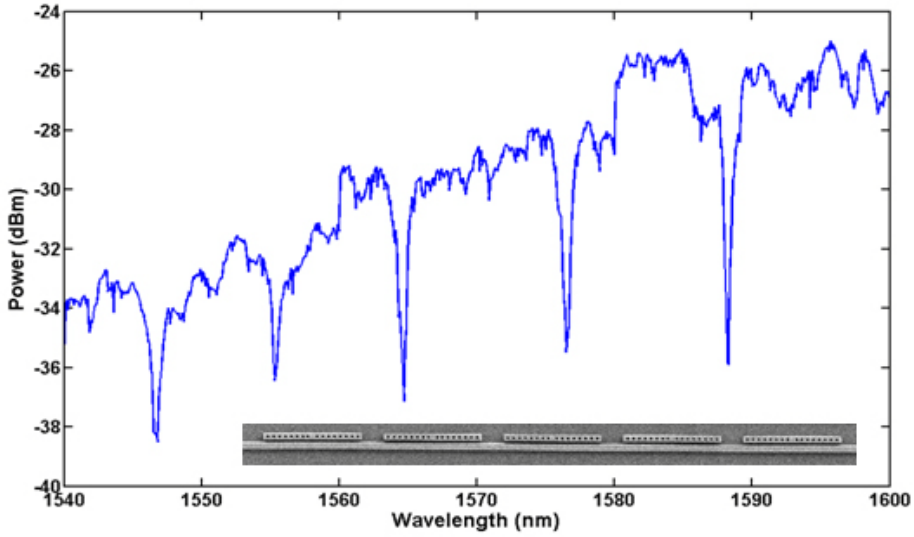

Figure 3.5: Output spectrum of a NOSA device consisting of five side-resonators as shown in the inset. Each dip in the spectrum is unique to one of the five resonators.

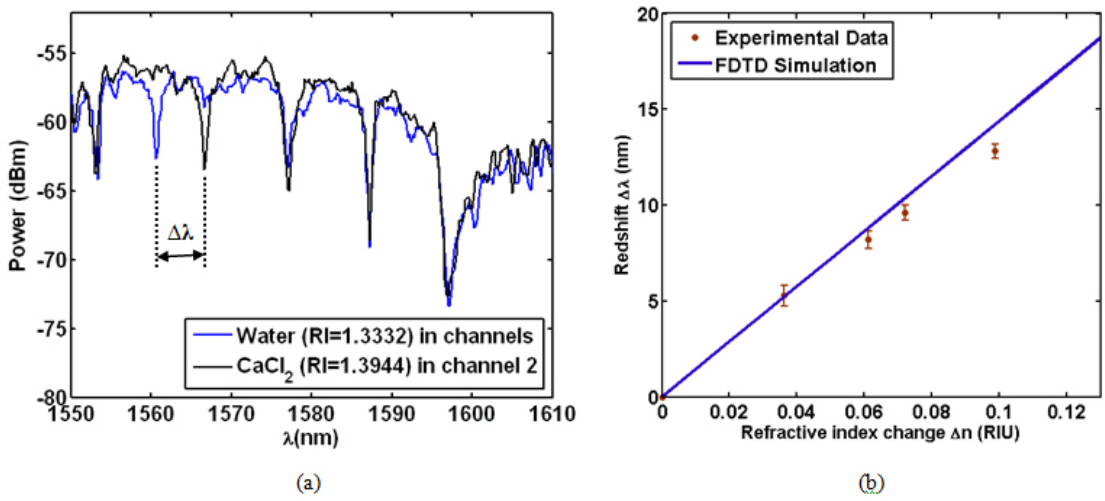

Figure 3.6: (a) Output spectrum for a NOSA where one of the 5 resonators is fluidically targeted, first with water and then with a $CaCl_2$ solution. The resonance of the targeted resonator shifts towards the red end of the spectrum due to the higher refractive index of the $CaCl_2$ solution. (b) Experimental data (with error bars indicating inter-device variability) showing the redshifts for various refractive index solutions. The blue line is the theoretically predicted redshift from FDTD simulations. The experimental data is in excellent agreement with the theory.

The RI sensitivity of the NOSA devices was characterized by flowing fluids of different refractive indices through a channel targeting a particular resonator. We used deionized (DI) water as well as various concentrations of Calcium Chloride solution. The molar concentration of the CaCl2 solutions varied from 1M to 5M. The refractive indices of all the liquids were initially measured using a commercial refractometer.

Figure 3.6(b) shows a plot of the shift in the resonant peak as a function of the change in refractive index of the fluid flowing through the channels. We observe an excellent match between the experimental data and the theoretically predicted redshifts. The slight discrepancy between the experimentally observed redshifts and those predicted by theory can possibly be attributed to optical losses in the waveguides and resonators arising due to surface roughness at their walls. The device exhibits a bulk refractive index sensitivity of over 130 nm for a unit shift in refractive index. Assuming a spectral resolution of 10 picometers we estimate the bulk refractive index detection limit of this device to be approximately $7x10^{-5}$. Thus, while the refractive index limit of detection of this device is not as good as techniques like SPR, the ability to drastically confine the detection volume by targeting the holes (especially the innermost holes as shown in the theoretical simulations) allows us to lower the mass limit of detection.

3.6 Conclusions

In this paper a new biosensor platform, which we refer to as nanoscale optofluidic sensor arrays, has been demonstrated and characterized. These devices comprise of a waveguide with a series of evanescently coupled “side resonators”. A change in the refractive index of the near field region surrounding the optical cavity results in a shift

in the resonant wavelength. We have characterized the sensitivity of this device and shown agreement between experimental results and theory. Our results suggest a bulk refractive index resolution of $7x10^{-5}$ which translates to a mass limit of detection of approximately 35 ag. While the Q-factors of the devices were demonstrated to be around 3000, they could be enhanced by optimizing the device geometry thus providing room for increasing the multiplexing capabilities of this architecture.

Acknowledgements

This work was supported by the Nanobiotechnology Center (NBTC), an STC Program of the National Science Foundation under Agreement No. ECS-9876771. Additional support for this work was provided by the National Institutes of Health - National Institute of Biomedical Imaging and Bioengineering (NIH-NIBIB) under grant number R21EB007031 and the Defense Advanced Research Projects Agency Microsystems Technology Office (DARPA-MTO) Young Faculty Award Program. We would also like to acknowledge Brad Schmidt and Michal Lipson for helpful discussions.

REFERENCES

[III.1] Erickson, D., Mandal, S., Yang, A. & Cordovez, B. Nanobiosensors: optofluidic, electrical and mechanical approaches to biomolecular detection at the nanoscale. *Microfluidics and Nanofluidics* **4**, 33-52 (2008).

[III.2] Luff, B. J. *et al.* Integrated optical Mach-Zehnder biosensor. *Journal of Lightwave Technology* **16**, 583-592 (1998).

[III.3] Ymeti, A. *et al.* Fast, ultrasensitive virus detection using a young interferometer sensor. *Nano Letters* **7**, 394-397 (2007).

[III.4] Matsko, A. B. & Ilchenko, V. S. Optical resonators with whispering-gallery modes - Part I: Basics. *IEEE Journal of Selected Topics in Quantum Electronics* **12**, 3-14 (2006).

[III.5] Armani, A. M. & Vahala, K. J. Heavy water detection using ultra-high-Q microcavities. *Optics Letters* **31**, 1896-1898 (2006).

[III.6] Vollmer, F. *et al.* Protein detection by optical shift of a resonant microcavity. *Applied Physics Letters* **80**, 4057-4059 (2002).

[III.7] Armani, A. M., Kulkarni, R. P., Fraser, S. E., Flagan, R. C. & Vahala, K. J. Label-Free, Single-Molecule Detection with Optical Microcavities. *Science* **317**, 783-787, doi:10.1126/science.1145002 (2007).

[III.8] Karlsson, R. SPR for molecular interaction analysis: a review of emerging application areas. *Journal of Molecular Recognition* **17**, 151-161 (2004).

[III.9] Lee, M. R. & Fauchet, P. M. Two-dimensional silicon photonic crystal based biosensing platform for protein detection. *Optics Express* **15**, 4530-4535 (2007).

[III.10] Skivesen, N. *et al.* Photonic-crystal waveguide biosensor. *Optics Express* **15**, 3169-3176 (2007).

[III.11] Joannopoulos, J. D., Meade, R. D. & Winn, J. W. *Photonic Crystals: Molding the Flow of Light*. (Princeton University Press, 1995).

[III.12] Foresi, J. S. *et al.* Photonic-bandgap microcavities in optical waveguides. *Nature* **390**, 143-145 (1997).

[III.13] Schmidt, B., Almeida, V., Manolatou, C., Preble, S. & Lipson, M. Nanocavity in a silicon waveguide for ultrasensitive nanoparticle detection. *Applied Physics Letters* **85**, 4854-4856 (2004).

[III.14] Monat, C., Domachuk, P. & Eggleton, B. J. Integrated optofluidics: A new river of light. *Nature Photonics* **1**, 106-114 (2007).

[III.15] Psaltis, D., Quake, S. R. & Yang, C. H. Developing optofluidic technology through the fusion of microfluidics and optics. *Nature* **442**, 381-386 (2006).

[III.16] Almeida, V. R., Barrios, C. A., Panepucci, R. R. & Lipson, M. All-optical control of light on a silicon chip. *Nature* **431**, 1081-1084 (2004).

[III.17] Velha, P. *et al.* Ultracompact silicon-on-insulator ridge-waveguide mirrors with high reflectance. *Applied Physics Letters* **89**, 171121-171123 (2006).

[III.18] Elhadj, S., Singh, G. & Saraf, R. F. Optical Properties of an Immobilized DNA Monolayer from 255 to 700 nm. *Langmuir* **20**, 5539-5543 (2004).

[III.19] Almeida, V. R., Panepucci, R. R. & Lipson, M. Nanotaper for compact mode conversion. *Optics Letters* **28**, 1302-1304 (2003).

[III.20] Quake, S. R. & Scherer, A. From micro- to nanofabrication with soft materials. *Science* **290**, 1536-1540 (2000).

CHAPTER 4

A MULTIPLEXED OPTOFLUIDIC BIOMOLECULAR SENSOR FOR LOW MASS DETECTION*

4.1 Abstract

Optical techniques have proven to be well suited for *in situ* biomolecular sensing because they enable high fidelity measurements in aqueous environments, are minimally affected by background solution pH or ionic strength, and facilitate label-free detection. Recently, there has been significant interest in developing new classes of optically resonant biosensors possessing very high quality-factors. This high quality-factor enables them to resolve the presence of very small amounts of bound mass and leads to very low limits of detection. A drawback of these devices is that the majority of the resonant electromagnetic energy is confined within the solid light-guiding structure thus limiting the degree to which it overlaps with the bound matter. This in turn lowers the ultimate device sensitivity, or the change in output signal in response to changes in bound mass. Here we present a novel optofluidic biosensor platform that incorporates a unique one-dimensional photonic crystal resonator array which enables significantly stronger light-matter interaction. We show here how this, coupled with the ability of planar photonic crystals to spatially localize the optical field to mode volumes on the order of a wavelength cubed, enables a limit of detection on the order of 63 ag total bound mass (estimated using a polyelectrolyte growth model) and a device sensitivity an order of magnitude better than similar devices. The multiplexing capabilities of our sensor are demonstrated by the individual and concurrent detection of interleukins 4, 6 and 8 using a sandwich assay.

* This chapter was previously published in Mandal, S., Goddard, J. M. and Erickson, D., "A Multiplexed Optofluidic Biomolecular Sensor for Low Mass Detection", *Lab on a* Chip, 9, 2924-2932 (2009). **DOI:**10.1039/b907826f. Reproduced by permission of The Royal Society of Chemistry.

4.2 Introduction

Biosensors that exploit optical [IV.1-3], electrical [IV.4], and mechanical [IV.5] methods of signal transduction bypass the need for a fluorescent, radio, or enzymatic labels. Label-free approaches can exhibit enhanced sensitivity and specificity over traditional sensors because such labels can: interfere with the binding event, non-specifically adsorb to the surface, and complicate the chemistry of the detection reaction [IV.6]. Of these methods, optical biosensors are particularly promising because of their low limits of detection, high sensitivities and capacity for multiplexed detection [IV.7-9]. While recent nano-mechanical [IV.10] and nano-electrical [IV.11-12] devices have similarly proven successful, they tend to be limited in that they require measurements to be made outside of liquid environment, or exhibit sensitivity to background electrical conditions such as solution pH and ionic strength. The performance of optical sensors is far less dependent on favorable environmental conditions making them appropriate for a much broader range of applications.

This advantage, amongst others, has led to the development of a large number of label-free optical sensor technologies, including interferometric [IV.13-14], resonant-cavity [IV.3, 15-16], photonic crystal [IV.17-19] and surface plasmon resonance (SPR) [IV.20-22] devices. The performance of a biosensor is characterized by two parameters: its limit of detection (the smallest amount or target that can be detected) and the device sensitivity (or the amount by which the detection signal responds to a change in input). In the case of optical biosensors the limit of detection is largely determined by how precisely a change in the output signal can be resolved and sensitivity by how strong the overlap is between the electromagnetic energy [IV.23] and the target molecules. As a result of this, there has been significant recent interest in the development of whispering gallery mode (WGM) type biosensors,

exploiting toroidal [IV.24], microsphere [IV.25], microring [IV.26], and microdisk [IV.27] resonator structures. The advantage of these devices is the high degree to which electromagnetic energy can be localized resulting in very high quality factors (Q-factor) and very narrow line-widths. These narrow line widths make it relatively simple to resolve subtle changes in the resonant frequency, yielding very low limits of detection [IV.3]. In general however to achieve these high Q-factors the electromagnetic energy must be largely confined within a solid structure and thus the extent to which it can interact with the bound molecular targets is limited to a small portion of the evanescent field, negatively impacting device sensitivity.

We present here a label-free multiplexed immunosensor based on our nanoscale optofluidic sensor array (NOSA) architecture [IV.28]. Illustrated in Figure 4.1, our device consists of arrays of evanescently coupled one-dimensional photonic crystal resonators. As we demonstrate below, the accessible optical field inside the holes of photonic crystal is significantly stronger than the evanescent fields of WGM sensors, thereby strengthening the light-matter interactions that enhance sensitivity. We demonstrate here how this coupled with the ability of planar photonic crystals to spatially localize the optical field to mode volumes on the order of a wavelength cubed [IV.29-30], enables a limit of detection on the order of 10s of attograms total bound mass (compared with femtograms [IV.17, 31-32]) and a device sensitivity an order of magnitude better than similar devices. In this paper we characterize the sensitivity of our device to bound mass by monitoring the growth of a polyelectrolyte multilayer and the resulting change in resonant wavelength. Real-time binding kinetics and dynamic range are determined by associating anti-streptavidin with surface-immobilized streptavidin. While many optically resonant sensors face design challenges when moving towards performing highly multiplexed detection, we demonstrate the facile

multiplexability our approach affords through the concurrent detection of multiple interleukins (IL-4, IL-6, and IL-8) in a single integrated optofluidic [IV.33-34] device.

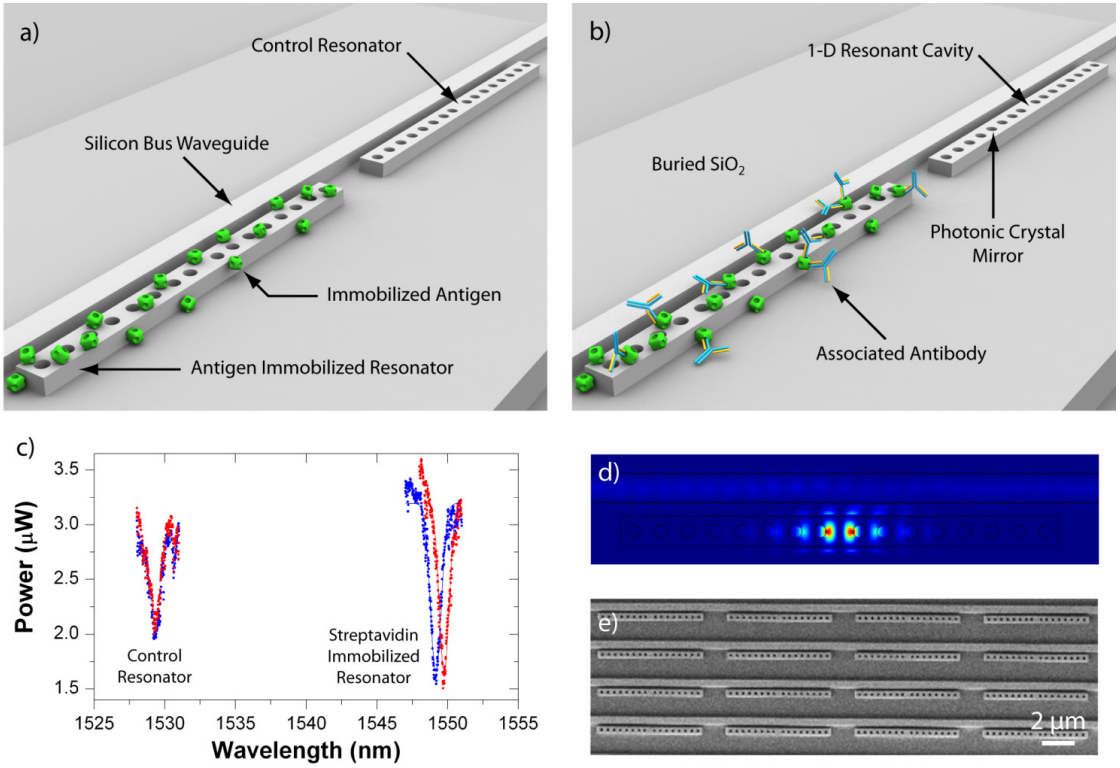

Figure 4.1: (a) 3D rendering of the NOSA device showing two 1-D photonic crystal resonators evanescently coupled to a silicon bus waveguide. The first resonator is immobilized with an antigen whereas the second resonator acts as a control. (b) 3D rendering illustrating the association of the corresponding antibody to the antigen immobilized resonator (not drawn to scale). (c) Experimental data illustrating the successful detection of 45 μg/ml of anti-streptavidin antibody. The blue trace shows the initial baseline spectrum corresponding to Figure 4.1(a) where the first resonator is immobilized with streptavidin. The red trace shows the test spectra after the association of anti-streptavidin as shown in Figure 4.1(b). The resonant wavelength of the control is unchanged while that of the streptavidin immobilized resonator red-shifts appreciably indicating successful detection of anti-streptavidin. (d) Finite difference time domain (FDTD) simulation of the steady state electric field distribution within the 1-D photonic crystal resonator at the resonant wavelength. (e) SEM image demonstrating the 2-dimensional multiplexing capability of the NOSA architecture.

4.3 Results

4.3.1 Device Operation and Detection Principle

As shown in Figure 4.1, the NOSA platform consists of multiple evanescently coupled 1-D photonic crystal resonators situated along a single bus waveguide. A central cavity in the 1-D photonic crystal structure of each resonator gives rise to a defect state [IV.35] in the photonic bandgap. This results in a resonant dip in the output spectrum of the bus waveguide. By tailoring the cavity length, each of the evanescently coupled 1-D resonators is designed to possess a unique resonant wavelength. Figure 4.1(d) illustrates the steady-state electric field intensity distribution within the 1-D resonator at the resonant wavelength. The binding of target biomolecules to the surface of the resonator induces a slight increase in the local refractive index around it. The interaction of the resonant optical field with the bound target biomolecules at the sensor surface and within the photonic crystal holes results in a red-shift in the corresponding resonant wavelength of the resonator. Put simply, the increase in the refractive index of the optical cavity caused by the presence of bound mass increases the effective optical length of the cavity and thereby the wavelength of light that will resonate within it. The output optical spectrum from the bus waveguide can be constantly monitored and binding of target biomolecules to the resonator is inferred when a red-shift is observed. Figure 4.1(c) illustrates a typical experiment demonstrating the detection of anti-streptavidin antibody binding to a streptavidin functionalized resonator. Note that no observable shift is detected in the case of the control resonator which is not streptavidin functionalized.

Since each evanescently coupled 1-D resonator possesses a unique resonance in the output spectrum, multiplexed detection along a single waveguide is possible. In

this case, each of the 1-D resonators is initially functionalized with a unique capture molecule. The sample containing target bio-molecules is made to flow over the 1-D resonators while the output spectrum is monitored. By observing the combination of resonances that red-shift it is possible to determine which target molecules were present in the detection sample. Analysis of the degree of red-shift provides quantitative information regarding the amount of bound mass which can be correlated to concentration of target molecule present in a sample. Figure 4.1(e) is an SEM image of a NOSA array, illustrating the 2-dimensional multiplexing capabilities of the platform.

4.3.2 Device Characterization

To quantitatively determine the device sensitivity to bound mass, we use a polyelectrolyte multilayer "layer-by-layer" deposition technique. This technique enables an accurate determination of the sensing range of a biosensor, i.e., how far above the sensor surface can biomolecules bind and still produce a shift in the resonant wavelength. This is important to characterize as it helps determine what kinds of surface conjugation techniques can be used successfully to immobilize the required capture biomolecules without pushing the bound target biomolecules too far above the sensor surface and away from the sensing region. Briefly, multilayers of polyethyleneimine and polyacrylic acid were deposited on the glutaraldehyde functionalized NOSA device, and on similarly functionalized silicon wafers in parallel. The scheme for surface functionalization is illustrated in Figure 4.2 (see supplementary material) and is fully described in the methods section. After deposition of each layer, output spectra were recorded to quantify shift in resonant

wavelengths and polyelectrolyte multilayer film thickness was determined on silicon wafers using ellipsometry. Output spectra were compared to the initial baseline spectra to determine resonance shift ($\Delta\lambda$, in nm), and were plotted against film thickness as plotted in Figure 4.3.

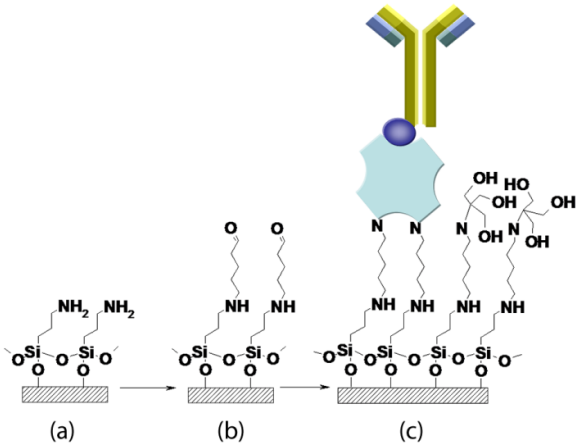

Figure 4.2: Schematic of surface functionalization chemistry. (a) After APTMS treatment, (b) after immobilization of glutaraldehyde, (c) after conjugation of streptavidin hydrazide, blocking of remaining aldehyde groups by Tris, and finally association of biotinylated capture antibodies.

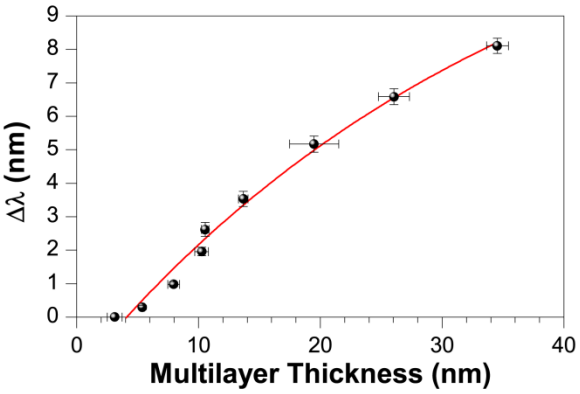

Figure 4.3: Optical response to polyelectrolyte layer growth. Effect of polyelectrolyte multilayer thickness on resonance shift. Data have been fit to an exponential model; error bars represent standard deviation.

Baseline spectra ($\Delta\lambda$ = 0 nm) were taken on 5 NOSA resonators and parallel silicon wafers after surface functionalization. A film thickness of 3.11 nm corresponds to the molecular thickness of native oxide, amine-terminated silane monolayer, and glutaraldehyde functionalization, each of which contributes ~1 nm to total film thickness. Since the field at the sensor surface exhibits an exponential decay, the growth of the polyelectrolyte multilayer and the resulting effect on resonance shift were fit to an exponential model as shown in Figure 4.3. Although the device continues to respond past 30 nm of deposited polyelectrolyte multilayers, it exhibits the greatest sensitivity in the first 20 nm of multilayer growth, with an apparent sensitivity of 0.35 nm resonance shift per nanometer multilayer growth. This suggests that the NOSA device is well suited for small molecule detection, as the Stokes radii of proteins relevant in medical diagnostics and nucleic acids relevant in pathogen detection tend to be below 15 nm, in the region of greatest device sensitivity. Figure 4.4 is a finite difference time domain (FDTD) simulation that illustrates the field decay within the innermost hole of the 1-D resonator which reaches a 1/e value 80 nm away from the hole surface. Thus the NOSA architecture can probe regions even 80-90 nm away from the substrate, which is consistent with our experimental observation (Figure 4.3) that the red-shift did not saturate for polyelectrolyte layers up to 35 nm thick.

4.3.3 Label-free Multiplexed Immunoassay

Cytokines represent a unique class of serum signaling proteins that have proven to be a useful tool in diagnostics. Specifically, interleukins have been demonstrated to be excellent candidates as cancer biomarkers [IV.36]. The potential for monitoring of *in-*

vivo concentrations of various interleukins for prognosis in cancer patients [IV.37-38] has generated significant interest in the biosensor community.

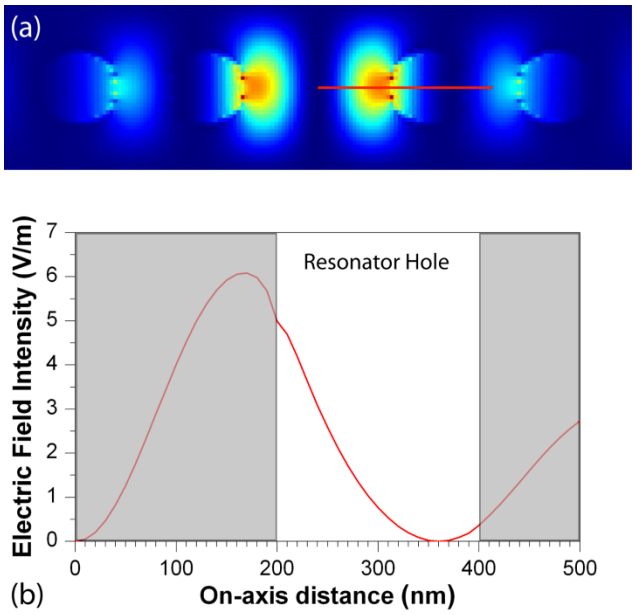

Figure 4.4: Electric field distribution inside resonator hole. (a) FDTD simulation showing the steady state electric field distribution within the central resonator cavity for the resonant wavelength. (b) Plot of the Electric field intensity along the red line shown in Figure 4.4(a). The gray boxes indicate the device silicon whereas the white area indicates the electric field intensity within the innermost hole of the 1-D resonator. It is clear that a significant portion of the resonant field extends within the holes of the resonator thus allowing for strong light-matter interactions within the holes. The field decays to its 1/e value approximately 80 nm away from the wall of the hole.

To demonstrate the multiplexability of the NOSA device, monoclonal antibodies to interleukin 4, 6, and 8 were immobilized on adjacent resonators and tested for cross-reactivity (see methods). Glutaraldehyde functionalized resonators and streptavidin immobilized resonators served as controls for non-specific analyte adsorption. As an additional control, cross-reactivity of secondary antibodies with complementary as well as non-complementary capture antibodies was assessed. Resonance shifts due to cross-reactivity were less than 0.02 nm in all experiments and

did not therefore significantly affect the detection resonance shift. The Q-factor of 3000 for our resonators sets our detection limit at 0.01 nm. Reported data are representative of experiments repeated on at least two separate days. To assess multiplex capability, we tested concurrent detection of multiple interleukins after their association with secondary interleukin antibodies.

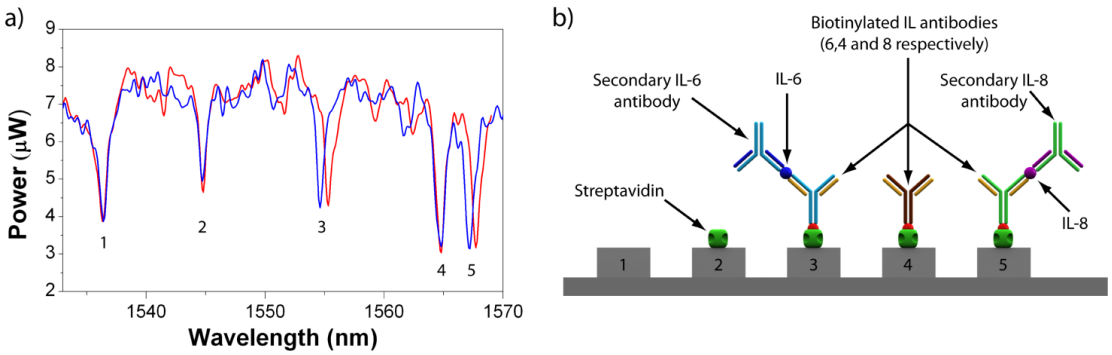

Figure 4.5: Multipexed detection of interleukins. (a) Spectra for resonators labelled 1 through 5 that correspond to control (glutaraldehyde functionalized), streptavidin-functionalized control, anti-interleukin 6, anti-interleukin 4, and anti-interleukin 8, respectively. The trace in blue shows the initial baseline spectrum. The red trace corresponds to the test spectrum after introducing 10 μg/ml of interleukin 6 along with 1 μg/ml of interleukin 8, followed by the sequential association of secondary antibodies corresponding to each of these interleukins. We clearly see shifts corresponding to the resonators functionalized with anti-interleukin 6 and 8 (Resonance 3 and 5 respectively) while the other resonances do not shift appreciably thus indicating the lack of non-specific binding. Fabry-Perot resonances were filtered out in both spectra by performing a fast Fourier transform. (b) Reaction stages at each of 5 resonators.

Figure 4.5(a) shows the resulting spectra after introducing 1 μg/ml of interleukin 8 along with 10 μg/ml of interleukin 6, followed by sequential association of secondary antibodies corresponding to each of these interleukins. In the figure, the resonant wavelengths numbered 1 through 5 correspond to control (glutaraldehyde functionalized), streptavidin-functionalized control, anti-interleukin 6, anti-interleukin 4, and anti-interleukin 8, respectively [Figure 4.5(b)]. The test spectrum (red) is

superimposed over the baseline spectrum (blue) to illustrate the lack of significant non-specific binding. We observe shifts in the resonance corresponding to immobilized monoclonal anti-interleukin 8 (0.58 nm) and 6 (0.68 nm), but no significant shift in the resonance corresponding to immobilized monoclonal anti-interleukin 4. This further supports the ability of the NOSA device to function as a multiplexed biosensor with little cross- reactivity or non-specific binding. Figure 4.6 (see supplementary information) shows the resulting spectra from other multiplexed assays after introduction of 10 μg/ml of interleukin 6, 8, or 4 (respectively), followed by association with secondary antibody. In each case, there is an average shift of 0.72 nm (mean of 6 determinations) with a standard deviation of 0.1 nm in the resonant wavelength corresponding to the target analyte used in a given experiment.

Physiologically relevant concentrations of serum interleukins for *in-vivo* monitoring are on the order of 1-10 pg/ml, which is within the detection limits of available ELISA techniques [IV.39-40]. While the demonstrated LOD of the NOSA prevents the detection of interleukins at these concentrations, as outlined in the subsequent section, improvements in the sensor design can enable extremely high-Q microcavity resonators with a significantly improved detection limit. In addition, by tagging the secondary antibodies with nanoparticles possessing a high refractive (such as titanium dioxide) the induced red-shift can be amplified thus offering another means for enhancing the sensitivity of this biosensor platform. In its current design, our device can detect antibodies in a concentration range of 1 ug/ml to 1 mg/ml, which is of clinical significance in medical diagnostics (i.e. HIV detection), and drug screening [IV.41].

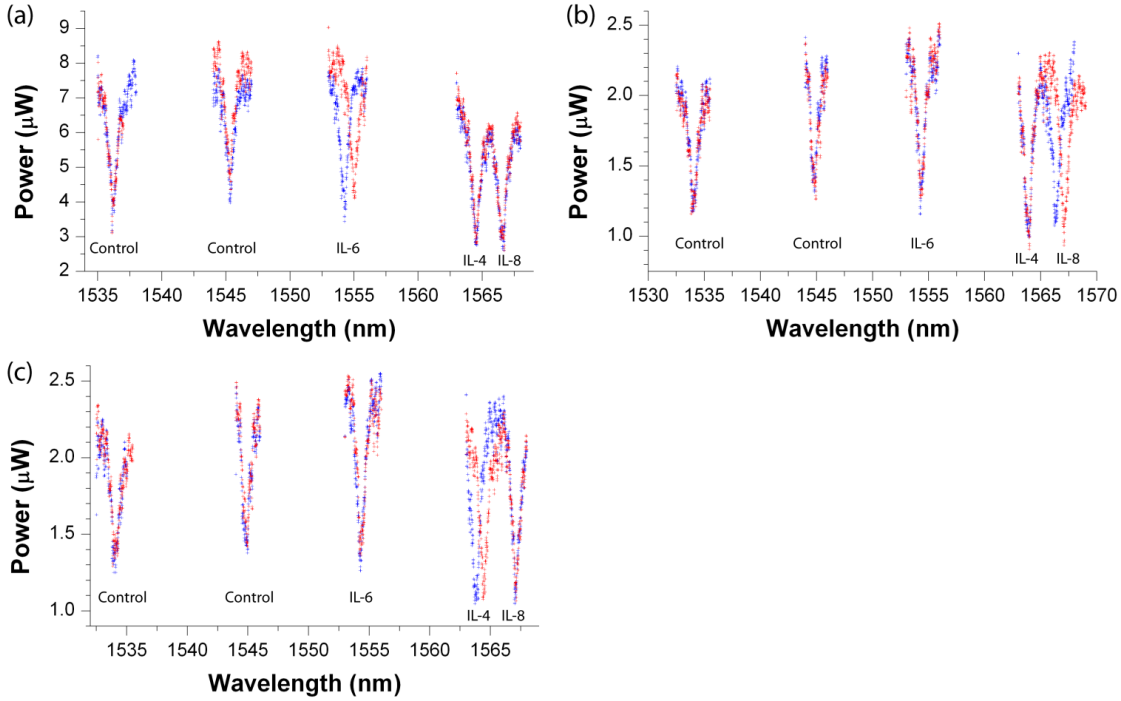

Figure 4.6: Plot showing the resulting spectra from multiplexed assays after introduction of 10 μg/ml of (a) interleukin 6, (b) interleukin 8, and (c) interleukin 4, followed by association with secondary antibody. Blue data points indicate the baseline spectrum taken before introducing the interleukins in the microfluidic channel. The red data points indicate the final test spectra after association with secondary antibodies. In each case we observe a shift of approximately 0.72 nm with negligible cross-reactivity.

4.3.4 Determination of Dynamic Range

A dose-response curve was generated by associating varying concentrations of anti-streptavidin antibody to immobilized streptavidin. Since all antibodies possess roughly the same size and molecular weight, we utilize an antibody-antigen system for determining and comparing the dynamic range of our NOSA sensor. Antibody concentration was varied from 0.010 to 500 μg/ml, and the resulting shift in resonant wavelength was recorded. The data were plotted on a log-linear scale as shown in

Figure 4.7, and fitted to a sigmoidal [IV.42] dose response model. These data indicate that the NOSA is capable of quantifying the concentration of antibody present in a sample in a dynamic range spanning two orders of magnitude (1 to 100 μg/ml) which is comparable to previous work on a streptavidin anti-streptavidin sensor [IV.43]. Using different biomolecular systems, WGM sensors [IV.3, 44] have previously demonstrated dynamic ranges spanning seven to eight orders of magnitude. As discussed in the next section, our current experiments are less sensitive due to the lower Q-factor of the 1-D resonators in comparison to most WGM sensors. However, this is not a fundamental limit and with future work on fabricating high-Q 1-D photonic crystal resonators, it should be possible to achieve similar dynamic ranges due to the enhanced detection limit while retaining the small device footprint and easy multiplexability afforded by the NOSA architecture.

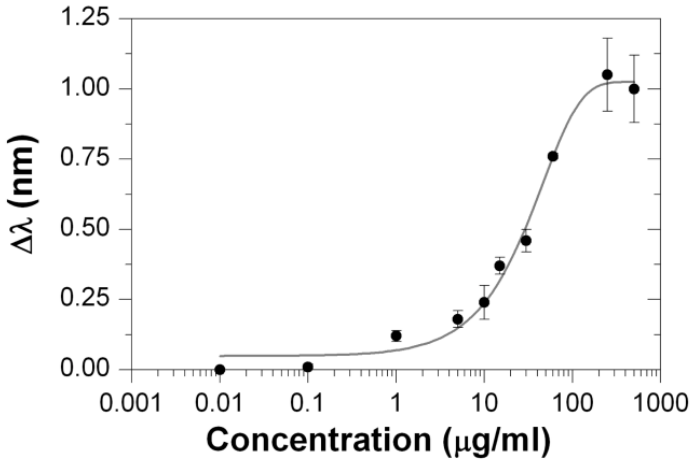

Figure 4.7: Streptavidin/anti-streptavidin dose response curve. Data have been fit to a sigmoidal model; error bars represent standard deviation.

Instead of continuously tuning the laser across its operational range to record the output spectrum, it is also possible to monitor the output power at a fixed

wavelength along the sloping profile of a resonant dip in the spectrum. As the resonant dip red-shifts due to the binding of target biomolecules, the power recorded at this fixed wavelength is observed to correspondingly increase as a function of time. Much like SPR sensors, it is possible to monitor biomolecular interactions in real-time and perform binding kinetic studies using this platform. Figure 4.8 shows the output power at a fixed wavelength (λ_m) for the association of 45 μg/ml anti-streptavidin antibody to a resonator on which streptavidin was immobilized. As expected, we clearly observe the association of anti-streptavidin to the sensor surface proceeding to saturation.

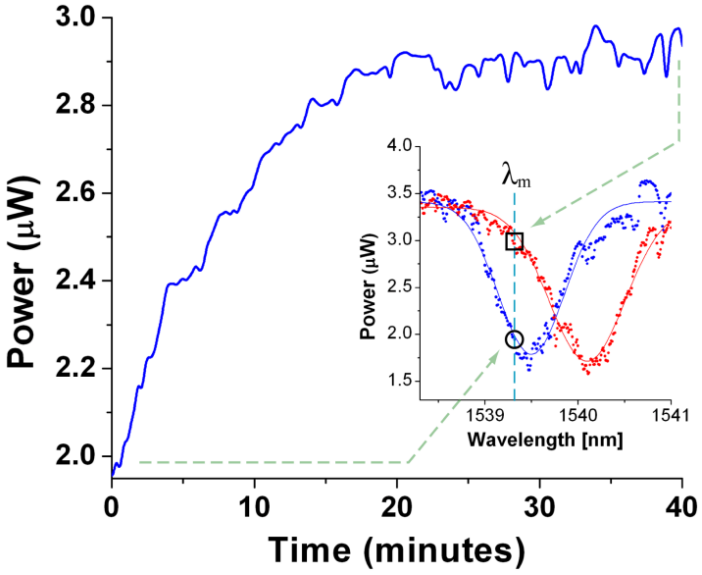

Figure 4.8: Measurement of binding kinetics. Trace of recorded power at a fixed wavelength λ_m as a function of time during the association of 45 μg/ml of anti-streptavidin antibody to a streptavidin functionalized resonator which clearly shows the reaction proceeding to saturation. The inset shows the correspondence of points at the start and end of the trace to the initial baseline and final red-shifted resonant spectrum.

4.4 Discussion

As mentioned above, we estimate here the mass sensitivity of the NOSA by growing multiple polyelectrolyte stacks consisting of polyethyleneimine (PEI) and polyacrylic acid (PAA) in a layer by layer manner. Ganesan *et. al.* [IV.45] measured the bound mass on a scanning probe cantilever due to the self-assembly of PEI and PAA monolayers. They reported measuring 24 pg of bound mass for a 5 layer polyelectrolyte stack over a surface area of 0.9×10^{-4} cm^2 which corresponded to a bound surface mass density of 2.67×10^{-7} g/cm^2. The functionalized surface area of a single 1-D photonic crystal resonant sensor including the internal surface area of the holes is 8.36 μm^2. Assuming the same surface mass density as above, we calculate the total bound mass on a NOSA sensor for a 5 layer stack of polyelectrolyte monolayers to be 22.3 fg. The corresponding red-shift in the resonant wavelength was observed to be 3.53 nm. The smallest resolvable red-shift can be approximated as the linewidth/50 [IV.2] which is approximately 0.01 nm in our system. Thus we estimate the smallest amount of bound mass that can be detected by our current sensor to be 63 ag corresponding to a surface mass coverage of 7.5 pg/mm^2. This value agrees well with our previously estimated mass LOD of the NOSA of tens of attograms [IV.28] using FDTD simulations. Due to the ultra-small mode volume of our 1-D photonic crystal resonator structure we are able to demonstrate a mass LOD that is an improvement on current optical biosensors [IV.17, 31-32] which are typically able to achieve mass LODs of a few femtograms. Current progress in improving the Q-factor of such 1-D resonators [IV.46-47] can greatly enhance the detection limit of our devices by orders of magnitude thus paving the way towards the detection of sub- attogram amounts of bound mass.

We compare our sensing platform to another robust, multiplexable photonic crystal based sensing platform developed by Choi *et al* .[IV.18] In their work they report observing a 1 nm red-shift while detecting the association of 500 μg/ml of rabbit IgG (Immunoglobin G). In our experiments, we have used rabbit IgG anti-streptavidin which possesses a similar molecular weight. We have demonstrated an equivalent red-shift of approximately 1nm for concentrations almost 5 times lower than those presented in the reference [IV.18] mentioned above (see Figure 4.7).

Recently, researchers have demonstrated high-Q optical resonator sensors with the capability to detect a single bio- molecule [IV.3] and virus [IV.15]. In addition other WGM sensors such as capillary based optofluidic ring resonators have demonstrated the ability to detect picomolar concentrations of adsorbed proteins [IV.48]. Our current experiments indicate a higher solution phase detection limit in comparison to these optical sensing techniques. In the case of resonant optical devices, the detection limit is primarily dictated by the Q-factor of the resonators. High Q-factors allow for narrow line-widths which increases the ability to resolve small shifts in the resonant peak. Micro-toroid resonators which possess Q-factors close to 10^8 are capable of resolving resonance shifts as small as 0.001 pm. In comparison our current sensors have a Q-factor of around 3000 thus setting the detection limit to approximately 0.01 nm. However, this is by no means a fundamental limitation of the device architecture. Researchers have recently designed similar 1-D photonic crystal resonators with a theoretical Q-factor as high as 10^8 [IV.47]. By incorporating such high-Q 1-D resonators, the NOSA architecture can achieve LODs that are similar to those of state of the art optical biosensors while maintaining a smaller device footprint.

While the detection limit of the current NOSA implementation is lower than some of these other optical interrogation techniques, it is important to note that the

refractive index sensitivity (which correlates to the device sensitivity) of 130 nm/RIU of the NOSA [IV.28] is almost an order of magnitude higher than most WGM optical sensors [IV.49]. Figure 4.4 shows the electric field distribution within the innermost hole of the 1-D photonic crystal resonator. It is evident that a very significant portion of the resonant optical field exists within the hole thus enabling stronger light-matter interaction at the sensor surface. This enhanced optical interaction leads to a higher device sensitivity in comparison to evanescent field and WGM sensors. Since most antibodies and antigens rarely exceed 20 nm in size they should easily infiltrate the holes of the photonic crystal resonator and bind to the sensor surface.

Another advantage of our approach over other optical resonator designs is its suitability for performing multiplexed detections. Due to the fabrication process and the planar nature of the device, it is easy to fabricate a single bus waveguide coupled to many 1-D photonic crystal resonators for performing multiplexed detections. In contrast, multiplexed detections in microtoroid, microsphere and some microdisk sensors requires complicated alignment of tapered optical fibers in free space [IV.50] thus making these sensors prohibitive for performing highly parallel detections in a robust, integrated sensor platform. Given our observed linewidth and the 100 nm operational range of a standard 1550 nm tunable laser, we expect that 50 1-D resonators could be incorporated along a single waveguide. However with current work on ultra high-Q single-dimensional microcavities [IV.46-47] the number of multiplexed resonators on a single waveguide can easily be extended into the hundreds. Another important advantage of the NOSA design is that the small cavity size results in each resonator possessing a large free spectral range (FSR) of over 200 nm. In comparison, most WGM sensors have cavity lengths over 100μm resulting in a maximum FSR of 3-5 nm. The large FSR for our NOSA architecture enables each resonator to have a single resonant peak in the output spectrum, thus facilitating

interpretation of the multiplexed output signal. The larger FSR of our sensor design also allows for a higher number of resonant sensors to be multiplexed along a waveguide as compared to WGM sensors.

4.5 Materials and Methods

4.5.1 Fabrication of NOSA device

The NOSA consists of a silicon (Si) waveguide with a 1D photonic crystal micro-cavity that lies adjacent to the waveguide. The side resonator consists of a central defect cavity with 8 holes on either side which form the 1-D photonic crystal. The Si waveguide was designed to be 450 nm wide and 250 nm tall to make it single mode. The low index silicon dioxide (SiO_2) layer which lies beneath the high index Si waveguide helps confine the light within the waveguide core, preventing optical losses into the lower substrate. The devices were fabricated using silicon-on-insulator (SOI) wafers having a device layer thickness of 250 nm which were subsequently patterned using electron beam (e-beam) lithography and finally etched using an inductively coupled plasma etching system. The residual e-beam resist (XR-1541, Dow Corning Corporation) was dissolved in a 100:1 HF solution which is dilute enough to prevent undercutting and releasing the devices from the silica substrate. Lift-off processing was used to mask each resonator on the chip and 1.8 μm of SiO_2 was subsequently evaporated onto the rest of the chip using e-beam evaporation. The evaporated SiO_2 serves two purposes. Firstly, it acts as a vital cladding layer for the nanotapers [IV.51] that is important for coupling light into the end facets of the waveguides and secondly, it protects large portions of the waveguides by masking them and thus preventing degradation in device behavior due to repeated usage. Each waveguide has five

evanescently coupled resonators placed adjacent to it where each resonator is designed to have a slightly different cavity spacing. Since the resonant wavelength is dependent on the central cavity length, each resonator has a unique resonant wavelength associated with it.

4.5.2 Experimental Setup

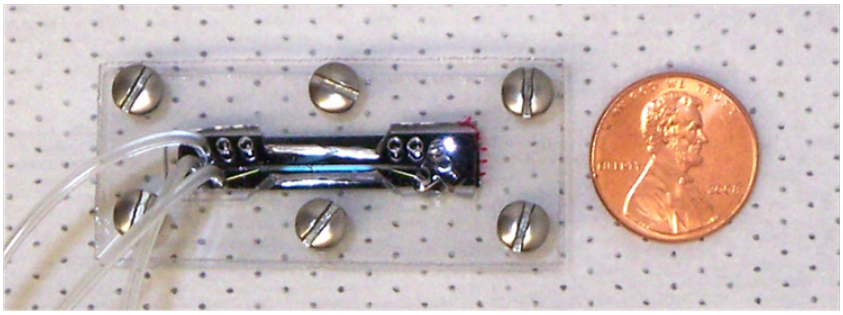

Figure 4.9: NOSA chip integrated with PDMS microfluidics and secured in a plexiglass housing.

The top microfluidic architecture was fabricated from polydimethylsiloxane (PDMS) using a soft lithography technique [IV.52]. After punching inlet and outlet ports, the channels were aligned with the resonators by using a modified overhead optical microscope setup, and secured with a custom plexiglass housing (Figure 4.9 in supplementary information). A laser source (Ando AQ4321D, Ando Corp, San Jose, CA) which is tunable between 1520 nm to 1620 nm was used to excite the waveguides. A lensed fiber is clamped onto a three axis stage and positioned precisely so as to couple light into the nanotaper present at the end facets of the waveguide. The chip is mounted on another 3-axis stage. A lens is used to collect and collimate the light from the output end of the waveguide into a photodetector. A polarizer is placed between the lens and the detector to select only the TE (Transverse Electric) component of light emerging from the waveguide. The photodetector was linked to a

PC via a GPIB controller (NI GPIB-USB-HS, National Instruments Corp, Austin, TX). A LABVIEW (National Instruments Corp, Austin, TX) script was used for data acquisition. Approximately 750 μW of optical power was launched into the input end of the waveguide and around 10-20 μW of optical power was measured at the output facet of the waveguides.

4.5.3 Surface Functionalization

Unless otherwise stated, all chemical reagents were purchased through VWR (West Chester, PA) and Sigma Aldrich (St. Louis, MO) and biological reagents were purchased from United States Biological (Swampscott, MA). After cleaning in piranha solution (1:3 hydrogen peroxide in concentrated sulfuric acid, thirty minutes at 70^{o}C) sensors were functionalized with 2% aminopropyltrimethoxysilane in 95% ethanol (5% deionized water) for 10 minutes, followed by rinsing in ethanol and curing for two hours at 80^{o}C. Amine-functionalized sensors were then shaken for two hours in 1x PBS (1x PBS is 10 mM phosphate buffer, 137 mM NaCl, and 2.7 mM KCl) , pH 7.4, containing 10 mM glutaraldehyde and 10 mM sodium cyanoborohydride to prepare aldehyde functionalized substrates. Immobilization of the polyelectrolyte multilayer and proteins (described below) was performed in polydimethylsiloxane (PDMS) microfluidic channels, prepared by casting a 1:10 ratio of curing agent to elastomer base over a positive relief master [IV.52]. To refurbish between uses, NOSA devices were soaked in concentrated sulfuric acid overnight to dissolve PDMS residues, after which they were treated for 10 minutes in air plasma (Harrick Plasma Cleaner PDC-32G, Ithaca, NY), followed by piranha cleaning and functionalization as described above.

4.5.4 Polyelectrolyte Multilayer

Deposition of the polyelectrolyte multilayer onto the NOSA sensor was performed in a microfluidic channel (45 mm x 1 mm x 2 cm). After a thirty minute wash in 30 mM sodium citrate buffer, containing 0.1% sodium dodecyl sulfate (SDS) and 0.3 M NaCl, baseline spectra were taken in 1.5 mM sodium citrate buffer, containing 15 mM NaCl. To form the polyelectrolyte multilayer, alternating solutions of polyethylenimine (PEI) and polyacrylic acid (PAA) (2 mg/ml in 1x PBS) were introduced to the channel for thirty minutes, after which spectra were recorded in 1.5 mM sodium citrate buffer, containing 15 mM NaCl. Covalent cross-linking agents were included during multilayer deposition in order to ensure stability of the polyelectrolyte multilayer to the shear stresses induced by continuous microfluidic flow. Deposition of the initial PEI layer was performed in cyanoborohydride coupling buffer (0.02 M sodium phosphate, pH 7.5, containing 0.2 M sodium chloride and 3.0 g/L sodium cyanoborohydride) and was allowed to conjugate for an hour, and 50 mM 1-ethyl-3-[3-dimethylaminopropyl] carbodiimide (EDC) and 5 mM N-hydroxysuccinimide (NHS) were included in the PAA solution. Ellipsometry (Nanofilm EP3, Nanofilm Technologie GmbH, Göttingen, Germany) was performed on silicon wafers treated in parallel with the NOSA device to quantify thicknesses of deposited multilayers.

4.5.5 Protein Immobilization

In order to individually address parallel NOSA resonators, a set of functionalization PDMS microfluidics (5 adjacent channels, each channel 32 μm tall and 42 μm wide) was aligned over APTMS-glutaraldehyde functionalized NOSA sensors for protein

immobilization. Of the five parallel NOSA resonators, two were kept as controls and were therefore not further functionalized. Streptavidin hydrazide (100 μg/ml in 1x PBS, Thermo Fisher Scientific Inc, Rockford, IL) was conjugated to the remaining three resonators for two hours, followed by rinsing in 1x PBS. Binding kinetics and dynamic range experiments were conducted on streptavidin treated NOSA sensors as described below. For multiplexed interleukin immunoassays, biotinylated monoclonal antibodies to IL-4, IL-6, and IL-8 (100 μg/ml in 1x PBS) were conjugated for one hour to streptavidin treated NOSA sensors, followed by rinsing in 1x PBS. After protein immobilization, the functionalization fluidics were removed, and a separate set of detection fluidics (700 μm wide and 32 μm tall**)** were aligned for the immunoassays described below. The sizes of these channels were selected for experimental convenience and were not optimized for target capture efficiency as described in Squires *et al.* [IV.53] All antibodies and recombinant interleukins were purchased from United States Biological Inc. (Swampscott, Massachusetts) and were used without further purification.

4.5.6 Non-specific Blocking

It is often necessary to perform a blocking step prior to performing a biosensing assay in order to prevent non-specific adsorption of analyte and non-target material, and thus improve device sensitivity. Selection of appropriate blocking agents becomes a unique challenge for label-free biosensors that quantify signal based on bound mass, as the sensor cannot distinguish between adsorbed blocking agent and bound analyte. Blocking buffers that have been previously determined to provide high sensitivity and low background noise in ELISA or fluorescence based microfluidic assays may

therefore not be suitable for a label-free detection platform, even if the analytes are the same. We have evaluated several blocking agents and determined that 1x PBS containing 0.1% Tween-20 and 0.2 mg/ml bovine albumin (PBST) provides sufficient blocking, without compromising device sensitivity. Data illustrating the effect of blocking buffer on device sensitivity are provided in supplemental data (Figure 4.10).

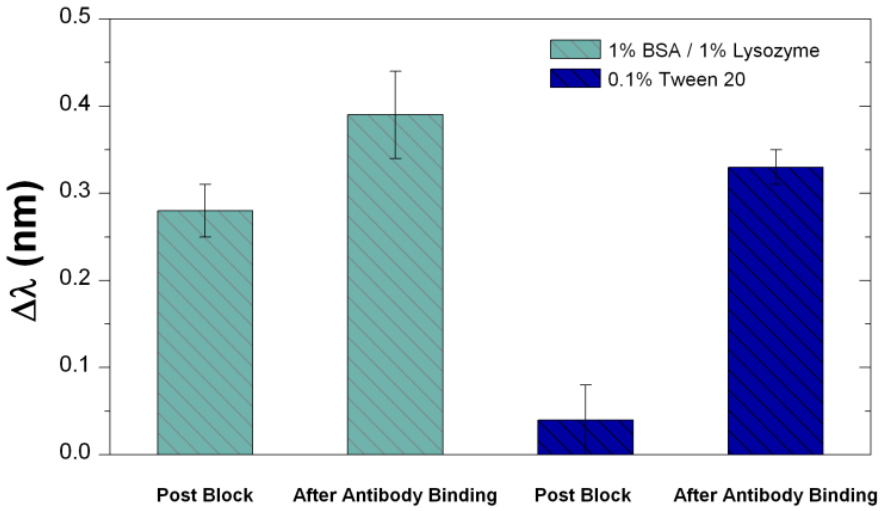

Figure 4.10: Effect of blocking buffer on device performance. Data represent mean of at least six repetitions; error bars represent standard deviation. In each experiment, the device is blocked for 15 minutes in blocking buffer, followed by association of 10 mg/ml anti-streptavidin antibody and recording of the resulting output spectra. Although the resonance shifts after association with antibody were similar, the resonance shift attributed to adsorbed blocking buffer alone was considerably higher with 1% BSA / 1% Lysozyme blocking buffer than with 0.1% Tween 20 blocking buffer (0.28 nm and 0.04 nm respectively). From this it was determined that 0.2 mg/ml BSA and 0.1% Tween 20 in PBS served as an appropriate blocking buffer.

4.5.7 Immunoassay Procedure

After alignment of detection fluidics, remaining aldehydes on the NOSA sensor surface were blocked with 0.1 M Tris, pH 8.0, containing 10 mM sodium cyanoborohydride for at least thirty minutes to prevent non-specific adsorption. The surface was then conditioned in 1x PBS containing 0.1% Tween-20 and 0.2 mg/ml bovine albumin (PBST), which was also used as the upper cladding fluid during spectral collection. For binding kinetics assays, 10 μg/ml polyclonal anti-streptavidin antibody in PBST was allowed to associate to the immobilized streptavidin for thirty minutes during which output power was collected to determine kinetics of antibody association on the NOSA sensor. Dynamic range of the sensor was determined by associating varying concentrations (0.01 to 500 μg/ml) of polyclonal anti-streptavidin antibody in PBST for 30 minutes, followed by brief rinsing with PBST, and spectral collection. Multiplexed NOSA immunoassays were performed by associating 10 μg/ml of one or multiple recombinant interleukins onto the immobilized monoclonal capture antibodies for 15 minutes, followed by rinsing in PBST, and association of 100 μg/ml secondary polyclonal antibody. Spectra were recorded, and resonant shifts were compared to the baseline spectra. After antibody association, the average resonance shift of control (aldehyde functionalized) resonators was less than 0.01 nm, and the shift of streptavidin functionalized resonators was 0.02 nm. These values correspond to the resolution limit of our sensor, suggesting that the observed shifts in resonance on the antibody functionalized resonators were a result of specific association of target antigens.

4.6 Conclusions

In conclusion, we have developed an optofluidic biosensor capable of multiplexed, label-free immunological detection with high device sensitivity and low mass limit of detection. We present a straightforward, repeatable technique to quantify the optical response of the device to changes in bound mass. By measuring device response as a function of growing polyelectrolyte multilayers, we are able to determine sensitivity of 0.35 nm resonance shift per nanometer of surface bound biomolecules. Comparing our results to reports of the mass of grown polyelectrolyte multilayers, we have estimated our device mass limit of detection to be 63 ag and a device sensitivity at least an order of magnitude greater than previously reported devices. Using the streptavidin / anti-streptavidin model, we characterized the dose-response of the NOSA device and observed a dynamic range of 1 to 100 μg/ml. Finally, by monitoring a single resonance during antibody association, we were able to observe binding kinetics in real-time, demonstrating how the NOSA device can be used for *in situ* monitoring of biomolecular interactions.

Acknowledgements

This work was supported by the Nanobiotechnology Center (NBTC), an STC Program of the National Science Foundation under Agreement No. ECS-9876771 and the National Institutes of Health - National Institute of Biomedical Imaging and Bioengineering (NIH-NIBIB) under grant number R21EB007031. Additional support has also been provided by the Defense Advanced Research Projects Agency Microsystems Technology Office (DARPA-MTO) Young Faculty Award Program.

Portions of this work were performed at the Cornell Nanoscale Facility, a member of the National Nanotechnology Infrastructure Network, which is supported by the National Science Foundation (Grant ECS-0335765).

REFERENCES

[IV.1] Anker, J. N. *et al.* Biosensing with plasmonic nanosensors. *Nature Materials* **7**, 442-453 (2008).

[IV.2] Arnold, S., Khoshsima, M., Teraoka, I., Holler, S. & Vollmer, F. Shift of whispering-gallery modes in microspheres by protein adsorption. *Optics Letters* **28**, 272-274 (2003).

[IV.3] Armani, A. M., Kulkarni, R. P., Fraser, S. E., Flagan, R. C. & Vahala, K. J. Label-Free, Single-Molecule Detection with Optical Microcavities. *Science* **317**, 783-787, doi:10.1126/science.1145002 (2007).

[IV.4] Daniels, J. S. & Pourmand, N. Label-free impedance biosensors: Opportunities and challenges. *Electroanalysis* **19**, 1239-1257 (2007).

[IV.5] Raiteri, R., Grattarola, M., Butt, H.-J. & Skládal, P. Micromechanical cantilever-based biosensors. *Sensors and Actuators B: Chemical* **79**, 115-126 (2001).

[IV.6] Cooper, M. A. Label-free screening of bio-molecular interactions. *Analytical and Bioanalytical Chemistry* **377**, 834-842 (2003).

[IV.7] Leatherbarrow, R. J. & Edwards, P. R. Analysis of molecular recognition using optical biosensors. *Current Opinion in Chemical Biology* **3**, 544-547 (1999).

[IV.8] Canziani, G. *et al.* Exploring biomolecular recognition using optical biosensors. *Methods* **19**, 253-269 (1999).

[IV.9] Erickson, D., Mandal, S., Yang, A. H. J. & Cordovez, B. Nanobiosensors: optofluidic, electrical and mechanical approaches to biomolecular detection at the nanoscale. *Microfluidics and Nanofluidics* **4**, 33-52 (2008).

[IV.10] Ilic, B. *et al.* Enumeration of DNA molecules bound to a nanomechanical oscillator. *Nano Letters* **5**, 925-929 (2005).

[IV.11] Wang, W. U., Chen, C., Lin, K. H., Fang, Y. & Lieber, C. M. Label-free detection of small-molecule-protein interactions by using nanowire nanosensors. *Proceedings of the National Academy of Sciences of the United States of America* **102**, 3208-3212 (2005).

[IV.12] Patolsky, F., Zheng, G. F. & Lieber, C. M. Nanowire-based biosensors. *Analytical Chemistry* **78**, 4260-4269 (2006).

[IV.13] Ymeti, A. *et al.* Fast, ultrasensitive virus detection using a young interferometer sensor. *Nano Letters* **7**, 394-397 (2007).

[IV.14] Brandenburg, A. Differential refractometry by an integrated-optical Young interferometer. *Sensors and Actuators B-Chemical* **39**, 266-271 (1997).

[IV.15] Vollmer, F., Arnold, S. & Keng, D. Single virus detection from the reactive shift of a whispering-gallery mode. *Proceedings of the National Academy of Sciences* **105**, 20701-20704, doi:10.1073/pnas.0808988106 (2008).

[IV.16] Zhu, H. Y., White, I. M., Suter, J. D., Zourob, M. & Fan, X. D. Integrated refractive index optical ring resonator detector for capillary electrophoresis. *Analytical Chemistry* **79**, 930-937 (2007).

[IV.17] Lee, M. R. & Fauchet, P. M. Two-dimensional silicon photonic crystal based biosensing platform for protein detection. *Optics Express* **15**, 4530-4535 (2007).

[IV.18] Choi, C. J. & Cunningham, B. T. A 96-well microplate incorporating a replica molded microfluidic network integrated with photonic crystal biosensors for high throughput kinetic biomolecular interaction analysis. *Lab on a Chip* **7**, 550-556 (2007).

[IV.19] Schmidt, B., Almeida, V., Manolatou, C., Preble, S. & Lipson, M. Nanocavity in a silicon waveguide for ultrasensitive nanoparticle detection. *Applied Physics Letters* **85**, 4854-4856 (2004).

[IV.20] Wark, A. W., Lee, H. J. & Corn, R. M. Long-range surface plasmon resonance imaging for bioaffinity sensors. *Analytical Chemistry* **77**, 3904-3907, doi:10.1021/ac050402v (2005).

[IV.21] Yang, C.-Y. *et al.* Detection of picomolar levels of interleukin-8 in human saliva by SPR. *Lab on a Chip* **5**, 1017-1023 (2005).

[IV.22] Homola, J. Surface Plasmon Resonance Sensors for Detection of Chemical and Biological Species. *Chemical Reviews* **108**, 462-493, doi:doi:10.1021/cr068107d (2008).

[IV.23] Robinson, J. T., Chen, L. & Lipson, M. On-chip gas detection in silicon optical microcavities. *Optics Express* **16**, 4296-4301 (2008).

[IV.24] Armani, D. K., Kippenberg, T. J., Spillane, S. M. & Vahala, K. J. Ultra-high-Q toroid microcavity on a chip. *Nature* **421**, 925-928 (2003).

[IV.25] Vollmer, F. *et al.* Protein detection by optical shift of a resonant microcavity. *Applied Physics Letters* **80**, 4057-4059 (2002).

[IV.26] Ksendzov, A. & Lin, Y. Integrated optics ring-resonator sensors for protein detection. *Optics Letters* **30**, 3344-3346 (2005).

[IV.27] Sang-Yeon, C. & Jokerst, N. M. A Polymer Microdisk Photonic Sensor Integrated Onto Silicon. *Photonics Technology Letters, IEEE* **18**, 2096-2098 (2006).

[IV.28] Mandal, S. & Erickson, D. Nanoscale optofluidic sensor arrays. *Optics Express* **16**, 1623-1631 (2008).

[IV.29] Akahane, Y., Asano, T., Song, B.-S. & Noda, S. High-Q photonic nanocavity in a two-dimensional photonic crystal. *Nature* **425**, 944-947 (2003).

[IV.30] Song, B.-S., Noda, S., Asano, T. & Akahane, Y. Ultra-high-Q photonic double-heterostructure nanocavity. *Nature Materials* **4**, 207-210 (2005).

[IV.31] De Vos, K., Bartolozzi, I., Schacht, E., Bienstman, P. & Baets, R. Silicon-on-Insulator microring resonator forsensitive and label-free biosensing. *Optics Express* **15**, 7610-7615 (2007).

[IV.32] Zhu, H., White, I. M., Suter, J. D., Dale, P. S. & Fan, X. Analysis of biomolecule detection with optofluidic ring resonator sensors. *Optics Express* **15**, 9139-9146 (2007).

[IV.33] Monat, C., Domachuk, P. & Eggleton, B. J. Integrated optofluidics: A new river of light. *Nature Photonics* **1**, 106-114 (2007).

[IV.34] Psaltis, D., Quake, S. R. & Yang, C. H. Developing optofluidic technology through the fusion of microfluidics and optics. *Nature* **442**, 381-386 (2006).

[IV.35] Foresi, J. S. *et al.* Photonic-bandgap microcavities in optical waveguides. *Nature* **390**, 143-145 (1997).

[IV.36] Polanski, M. & Anderson, N. L. A List of Candidate Cancer Biomarkers for Targeted Proteomics. *Biomarker Insights* **1**, 1-48 (2007).

[IV.37] Bachelot, T. *et al.* Prognostic value of serum levels of interleukin 6 and of serum and plasma levels of vascular endothelial growth factor in hormone-refractory metastatic breast cancer patients. *British Journal of Cancer* **88**, 1721-1726.

[IV.38] Chen, Z. *et al.* Expression of proinflammatory and proangiogenic cytokines in patients with head and neck cancer. *Clinical Cancer Research* **5**, 1369-1379 (1999).

[IV.39] Leng, S. X. *et al.* ELISA and Multiplex Technologies for Cytokine Measurement in Inflammation and Aging Research. *J Gerontol A Biol Sci Med Sci* **63**, 879-884 (2008).

[IV.40] Lambeck, A. J. A. *et al.* Serum Cytokine Profiling as a Diagnostic and Prognostic Tool in Ovarian Cancer: A Potential Role for Interleukin 7. *Clin Cancer Res* **13**, 2385-2391, doi:10.1158/1078-0432.ccr-06-1828 (2007).

[IV.41] John V, P. Simple and Reliable Salivary Tests for HIV and Hepatitis A and B Virus Diagnosis and Surveillance. *Annals of the New York Academy of Sciences* **694**, 216-233 (1993).

[IV.42] DeLean, A., Munson, P. J. & Rodbard, D. Simultaneous analysis of families of sigmoidal curves: application to bioassay, radioligand assay, and physiological dose-response curves. *Am J Physiol Endocrinol Metab* **235**, E97-102 (1978).

[IV.43] Saleh, O. A. & Sohn, L. L. Direct detection of antibody-antigen binding using an on-chip artificial pore. *Proceedings of the National Academy of Sciences of the United States of America* **100**, 820-824, doi:10.1073/pnas.0337563100 (2003).

[IV.44] Zhu, H. Y., White, I. M., Suter, J. D., Zourob, M. & Fan, X. D. Opto-fluidic micro-ring resonator for sensitive label-free viral detection. *Analyst* **133**, 356-360, doi:10.1039/b716834a (2008).

[IV.45] Ganesan, P. G., Wang, X. & Nalamasu, O. Method for sensing the self-assembly of polyelectrolyte monolayers using scanning probe microscope cantilever. *Applied Physics Letters* **89**, 213107-213113 (2006).

[IV.46] Sauvan, C., Lecamp, G., Lalanne, P. & Hugonin, J. Modal-reflectivity enhancement by geometry tuning in Photonic Crystal microcavities. *Optics Express* **13**, 245-255 (2005).

[IV.47] Notomi, M., Kuramochi, E. & Taniyama, H. Ultrahigh-Q nanocavity with 1D photonic gap. *Optics Express* **16**, 11095-11102 (2008).

[IV.48] Suter, J. D. *et al.* Label-free quantitative DNA detection using the liquid core optical ring resonator. *Biosensors and Bioelectronics* **23**, 1003-1009 (2008).

[IV.49] White, I. M., Oveys, H., Fan, X., Smith, T. L. & Zhang, J. Integrated multiplexed biosensors based on liquid core optical ring resonators and antiresonant reflecting optical waveguides. *Applied Physics Letters* **89**, 191106-191113 (2006).

[IV.50] Vollmer, F., Arnold, S., Braun, D., Teraoka, I. & Libchaber, A. Multiplexed DNA Quantification by Spectroscopic Shift of Two Microsphere Cavities. *Biophysical Journal* **85**, 1974-1979 (2003).

[IV.51] Almeida, V. R., Panepucci, R. R. & Lipson, M. Nanotaper for compact mode conversion. *Optics Letters* **28**, 1302-1304 (2003).

[IV.52] Duffy, D. C., McDonald, J. C., Schueller, O. J. A. & Whitesides, G. M. Rapid prototyping of microfluidic systems in poly(dimethylsiloxane). *Analytical Chemistry* **70**, 4974-4984 (1998).

[IV.53] Squires, T. M., Messinger, R. J. & Manalis, S. R. Making it stick: convection, reaction and diffusion in surface-based biosensors. *Nat Biotech* **26**, 417-426 (2008).

CHAPTER 5

NANOMANIPULATION USING SILICON PHOTONIC CRYSTAL RESONATORS*

5.1 Abstract

Optical tweezers [V.1] have enabled a number of microscale processes such as single cell handling [V.2], flow-cytometry [V.3], directed-assembly [V.4-5] and optical chromatography [V.6-7]. To extend this functionality to the nanoscale, a number of near-field approaches have been developed that yield much higher optical forces by confining light to sub-wavelength volumes [V.8-10]. At present, these techniques are limited in both the complexity and precision with which handling can be performed. Here, we present a new class of nanoscale optical trap exploiting optical resonance in one-dimensional silicon photonic crystals. The trapping of 48-nm and 62-nm dielectric nanoparticles is demonstrated along with the ability to transport, trap and manipulate larger nanoparticles by simultaneously exploiting the propagating nature of the light in a coupling waveguide [V.11] and its stationary nature within the resonator. Field amplification within the resonator is shown to produce a trap several orders of magnitude stronger than conventional tweezers and an order or magnitude stiffer than other near-field techniques. Our approach lays the groundwork for a new class of optical trapping platforms that could eventually enable complex all-optical single molecule manipulation and directed assembly of nanoscale material.

* This chapter was previously published in Mandal, S., Serey, X. & Erickson, D., "Nanomanipulation Using Silicon Photonic Crystal Resonators", *Nano Letters*, doi:10.1021/nl9029225 (2009). Reproduced by permission of the American Chemical Society. Xavier Serey worked on the numerical simulations in collaboration with Sudeep Mandal.

5.2 Introduction

Since Arthur Ashkin's pioneering work [V.12] on laser-induced optical trapping and the manipulation of micrometer sized dielectric microspheres, optical tweezers have developed into an invaluable tool for a variety of applications such as flow-cytometry [V.2-3], single-molecule studies [V.13-14] and optical chromatography [V.6-7]. The interest in optical tweezers lies in their ability to precisely and non-invasively manipulate particles and to decouple their motion from that of the ambient background (for example a flow within a microfluidic environment). Recently demonstrated indirect optical methods [V.15] have enabled a similar level of control with significantly lower optical power requirements. Researchers have also demonstrated easy fabrication of well calibrated optical traps in an integrated, microfluidic system by incorporating Fresnel zone plates [V.16]. However, in all these methods diffraction limits how tightly light can be focused which in turn limits the ultimate strength of the optical trap and by extension the size of the matter which can be manipulated.

Recently, researchers have demonstrated the ability to surpass the limits imposed by free-space diffraction by tailoring the optical and structural properties of a medium [V.10, 17-18]. For example, Grigorenko *et al.* [V.8] utilized the strongly enhanced and localized optical near-fields of closely spaced metallic nanostructures. Similarly Yang *et al*. [V.9] were able to demonstrate optical trapping and transport of dielectric nanoparticles by exploiting the strong field confinement within slot waveguides [V.19]. While the strength of optical traps can be enhanced by the strong confinement of the optical field, it can also be improved by exploiting the field amplification within an optical resonator. Recently, Arnold *et al.* [V.20] demonstrated

the trapping and transport of polystyrene nanoparticles as small as 280-nm in diameter in a circular orbit around whispering gallery mode (WGM) resonators possessing Q-factors as high as 10^6.

5.3 Results

5.3.1 Device Design

Here, we present a new class of resonant optical traps that are capable of generating extremely strong optical field gradients in three dimensions while simultaneously enhancing the trap stiffness due to the amplification of the optical field within the resonator and enabling advanced particle handling functionalities. As illustrated in Figure 5.1(a), our optical trap consists of a one-dimensional silicon photonic crystal resonator that is evanescently coupled to a single mode waveguide. The standing wave nature of the resonant optical field within the resonator enables a true static point trap with strong field confinement in all three dimensions. An SEM image of a typical resonator is shown in Figure 5.2.

When light at the resonant wavelength is coupled into the bus-waveguide, a stationary interference pattern is formed within the photonic crystal resonator resulting in a tight confinement of the optical field in an extremely small volume as illustrated in Figure 5.1(b). These strong field gradients coupled with the resonant amplification of the optical field within the resonator enables the stable trapping of particles ranging in size from 50-500 nm.

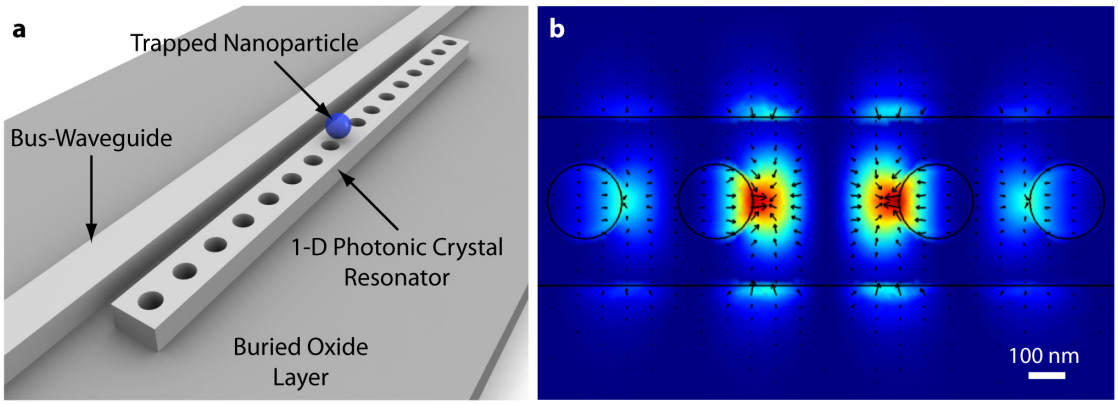

Figure 5.1: Photonic crystal resonator for enhanced optical trapping. (a) 3D schematic of the one-dimensional photonic crystal resonator optical trapping architecture **(b)** 3D FEM simulation illustrating the strong field confinement and amplification within the one-dimensional resonator cavity. The black arrows indicate the direction and magnitude of the local optical forces

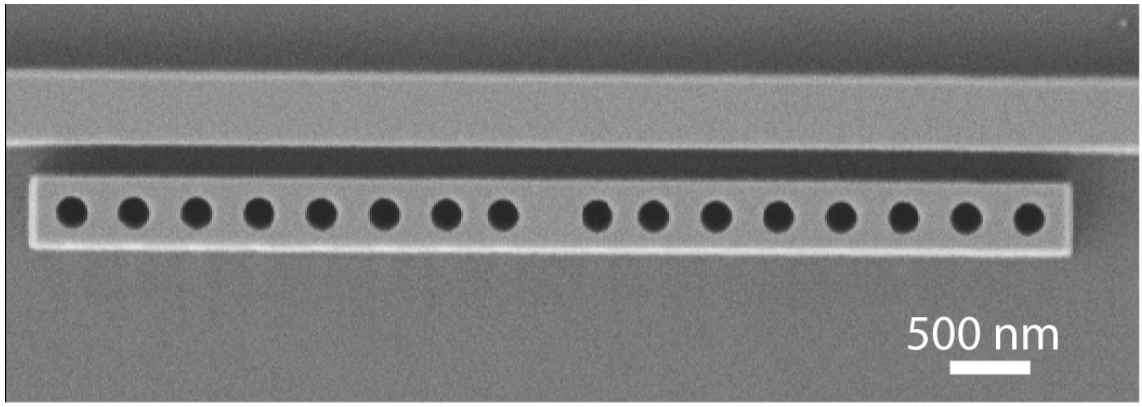

Figure 5.2: SEM Image of photonic crystal resonator. The photonic crystal resonators used in this work were fabricated from Silicon-on-Insulator using standard electron-beam lithography fabrication techniques described in our earlier works [V.21].

5.3.2 Optical Trapping and Handling of Nanoparticles

Figure 5.3 shows the trapping and release of a 62-nm polystyrene nanoparticle (refractive index n = 1.59). We were also able to trap polystyrene nanoparticles that were 48-nm in diameter. We note that both of these targets are well below the size

limit of what could be trapped using previous approaches [V.19]. A tunable infrared laser was used to couple TE polarized light at the resonant wavelength of 1548.15 nm into the input end of the waveguide using a lensed fibre. The output power at the fibre exit was measured to be 300-mW. In the experiment a microfluidic flow convects the particles along the channel and towards the resonator. If a particle passes within close proximity of the resonator surface and the resonant optical field lobes, it experiences a tweezing force due to the strong local field gradient resulting in the particle getting trapped at the resonator surface. The trapped particle is subsequently released by turning the laser power off (as is shown for the 62-nm case above). Trapped particles can also be released by either de-tuning the input wavelength away from resonance or by switching the polarization of light from TE to TM.

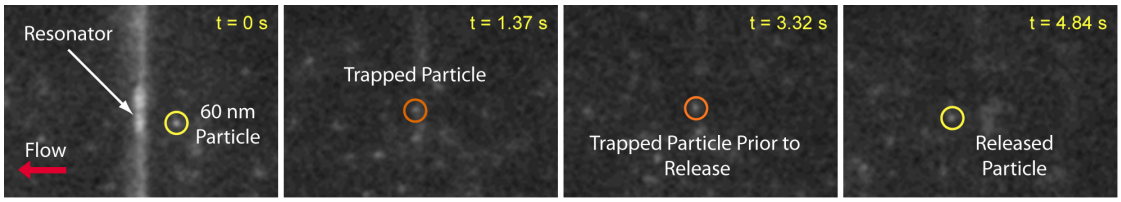

Figure 5.3: Trapping of nanoparticles on photonic crystal resonator. Capture and subsequent release of a 62-nm and 48-nm diameter polystyrene nanoparticle. In this figure the waveguide is excited at the resonant wavelength while 62-nm particles flow through a microfluidic channel running over the resonator and the waveguide. The sequence of images were captured by a Hamamatsu CCD camera with contrast and brightness adjustments applied to the entire image. The yellow circle tracks the 62-nm particle which is trapped (indicated by orange circles) on the resonator. Turning the laser power off releases the particle from the trap.

One interesting aspect of our optical trap design is that the guided optical mode within the waveguide possesses a forward momentum which enables the simultaneous trapping and propulsion of nanoparticles along its surface [V.11, 22-23]. In contrast, at resonance, the field within the optical resonator consists of a tightly confined standing wave with no propagation component. By tailoring the microfluidic flow and ex-

ploiting this contrasting nature of the optical field within the waveguide and the one-dimensional resonator we demonstrate a novel technique for performing particle manipulations.

Figure 5.4 illustrates a series of time-lapse images demonstrating the trapping and manipulation of 500-nm polystyrene microspheres. In the top panel of Figure 5.4 the flow in the microfluidic channel is from left to right. A 500-nm polystyrene microsphere is trapped and transported along the waveguide by the evanescent field of the guided optical mode. The input light is initially tuned to the resonant wavelength. As a result, when the particle moves up along the waveguide and approaches the resonator it experiences a lateral tweezing force towards the resonator centre. Due to the field amplification within the resonator and the stronger field gradients in the photonic crystal structure, the lateral tweezing force experienced by the particle is much stronger than the trapping force exerted by the waveguide. This results in the particle hopping from the waveguide to the resonator centre. Once trapped, the particle is held stationary on the resonator. To release the particle back onto the waveguide, the input wavelength is tuned away from resonance. This releases the particle from the resonator trap and it is convected with the fluid flow towards the waveguide. Since the waveguide is not wavelength selective, the evanescent field of the off-resonant guided optical mode re-traps the particle as it passes above its surface. Once the particle is trapped on the waveguide it is subsequently transported further along the waveguide. By reversing the direction of flow in the microchannel (Figure 5.4(b)) the trapped particle on the resonator can be rejected into the fluid flow when the input laser is tuned off-resonance.

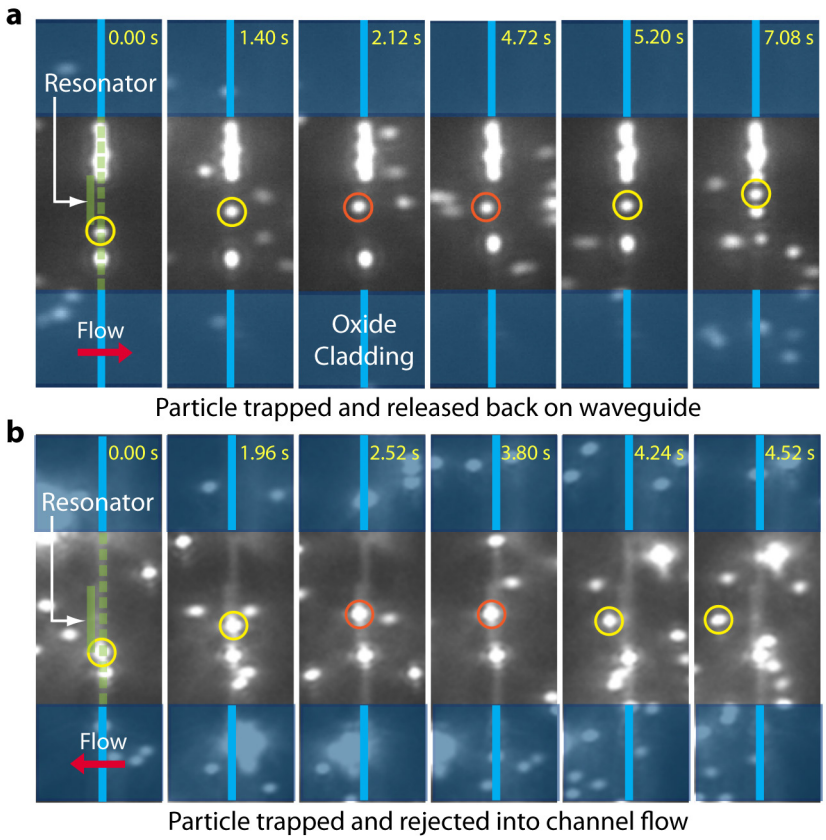

Figure 5.4: Particle handling and manipulation using photonic crystal resonators. (a) The waveguide is excited at the resonant wavelength with the guided mode propagating upwards (in the figure). A 500-nm particle is trapped on the waveguide (yellow circle) and is transported towards the resonator. When the particle arrives in the vicinity of the resonator centre it hops from the waveguide onto the resonator centre and remains trapped on the resonator (orange circles). Since the flow is from left to right, de-tuning the input wavelength away from resonance releases the particle from the resonator and back onto the waveguide after which it continues to be transported upwards along the waveguide. **(b)** By simply reversing the direction of flow in the microfluidic channel the particle can be rejected into the fluidic channel after it is initially transported and trapped at the resonator center.

5.3.3 Numerical Simulations and Trap Stiffness Measurement

To characterize the trapping stiffness as well as the maximum trapping force in all three dimensions in our system, we have carried out a detailed three-dimensional finite element numerical analysis using a commercial software package (COMSOL). Figure

5.5 illustrates the trapping force profile for a 100-nm polystyrene microsphere that is displaced in all three dimensions from the stable trapping position for 1-W of input power. We observe that the maximum trapping force for a 100-nm particle is 700 pN which is more than an order of magnitude higher than the maximum trapping force in the case of slot waveguides [V.9] (25 pN). A common figure of merit related to the quality of optical traps is the trap stiffness for a given particle size. From Figure 5.5 we estimate a trap stiffness of 4.81 pN nm^{-1} W^{-1}, 3.30 pN nm^{-1} W^{-1} and 8.53 pN nm^{-1} W^{-1} for a 100-nm polystyrene microsphere along the X, Y and Z axes respectively.

To obtain experimental values for the trapping stiffness in the X and Y axis and compare them with theoretical estimates, the suppressed Brownian motion of a trapped 200-nm particle was studied. Figure 5.6(a) illustrates a scatter plot of the position trace of a 200-nm particle when the output power measured at the waveguide output was 140 μW. The scatter plot is overlaid on top of the field distribution within the resonator (to scale). It is evident that at such low optical powers, the trap is weak and the particle hops between the two centre lobes of the resonant optical field. We also observe that the particle hops to the weaker traps at the side lobes for a short duration of time. When the power is raised such that the measured power at the waveguide output is 175 μW the strength of the trap increases and the particle is observed to remain stably trapped at a single site. Figure 5.6(c) and (d) shows histograms for the displacement of a trapped 200-nm particle which exhibits a Gaussian distribution. From these plots we are able to determine a radial trapping stiffness of 2.86 pN nm^{-1} W^{-1} which is slightly lower than our numerical estimate of 5.38 pN nm^{-1} W^{-1} for a 200-nm particle (see Section 1.5 and Figure 5.7).

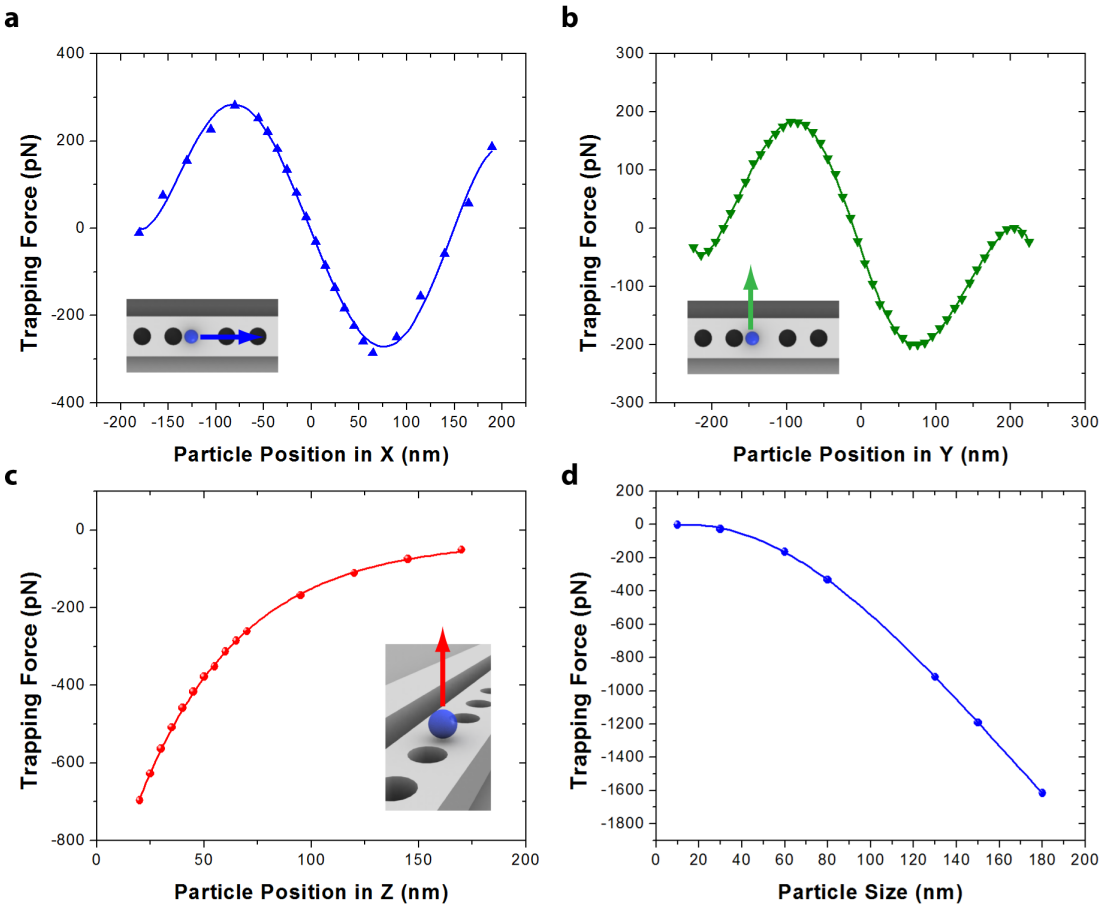

Figure 5.5: Numerical analysis of trapping stiffness and the maximum trapping force. All computed trapping forces listed are normalized to 1W of input power in the waveguide. **(a)** Force experienced by a 100-nm trapped polystyrene nanoparticle as it is displaced along the length of the resonator (X-axis). The zero X-axis value corresponds to the stable trapping position at the lobe centre. The linear nature of the plot of the restoring force in the X-axis indicates a Hookean behaviour over a displacement of approximately 75nm from the stable trapping position. **(b)** Graph illustrating the restoring force on a 100-nm particle as it is displaced in the Y-axis, normal to the length of the resonator. The zero Y-axis value corresponds to the stable trapping position at the lobe centre. Similar to the displacement in the X-axis, the restoring force indicates a Hookean behaviour for displacements of approximately 75-nm from the equilibrium trapping position. **(c)** Plot of the trapping force in the Z-direction as the particle is moved away from the resonator surface. The zero Z-axis value corresponds to the particle being in contact with the resonator surface. Due to the exponential nature of decay of the optical field in the Z-direction, the force is also observed to decay exponentially. **(d)** Graph shows the magnitude of the maximum trapping force in the Z-direction as a function of particle size. We observe that forces over 1 nN can be exerted on dielectric particles as small as 135-nm with this resonant photonic crystal architecture.

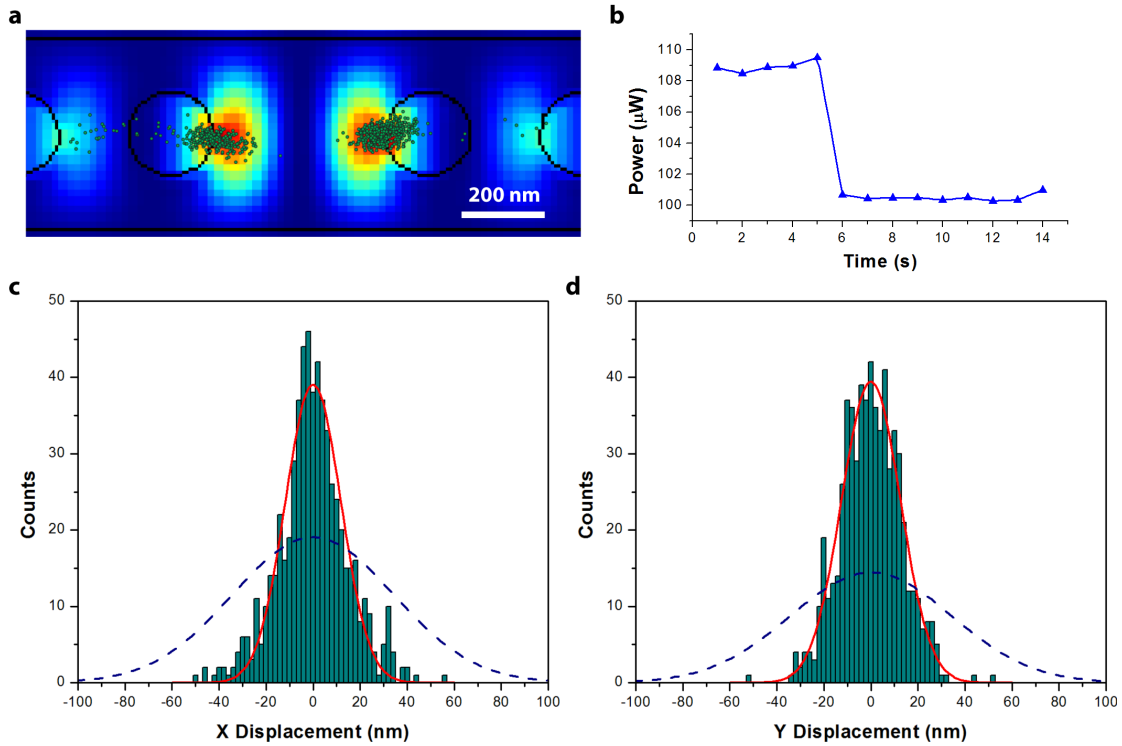

Figure 5.6: Trapping stiffness and the suppression of Brownian motion. (a) The plot shows the Brownian motion a 200-nm particle when the measured light output at the end of the waveguide was 140 μW. The particle is observed to hop between the two centre lobes in the resonant cavity. The nanoparticle is also observed to hop for a brief duration to the weaker optical lobes adjacent to the central lobes within the resonant cavity. **(b)** The release of a particle from a trap can be inferred by monitoring the output power of the waveguide for discrete jumps in the power level. In the case of 200-nm particles, the release of the particle induces a slight shift in the resonant wavelength of the cavity. This shift can be detected as a discrete jump in the output power at the end of the waveguide. This graph illustrates this concept by demonstrating a drop in the output power of the waveguide when the 200-nm particle escapes from the optical trap. **(c)** and **(d)** Histograms showing the Brownian motion of a trapped 200-nm particle in the X and Y directions at a single optical lobe (output power = 175 μW). The histograms follow a Gaussian distribution and are used to experimentally estimate the trapping stiffness of the optical traps. The blue dashed curves represent the true Gaussian fit for the Brownian motion after correcting for video motion-blur (see Section 1.5)

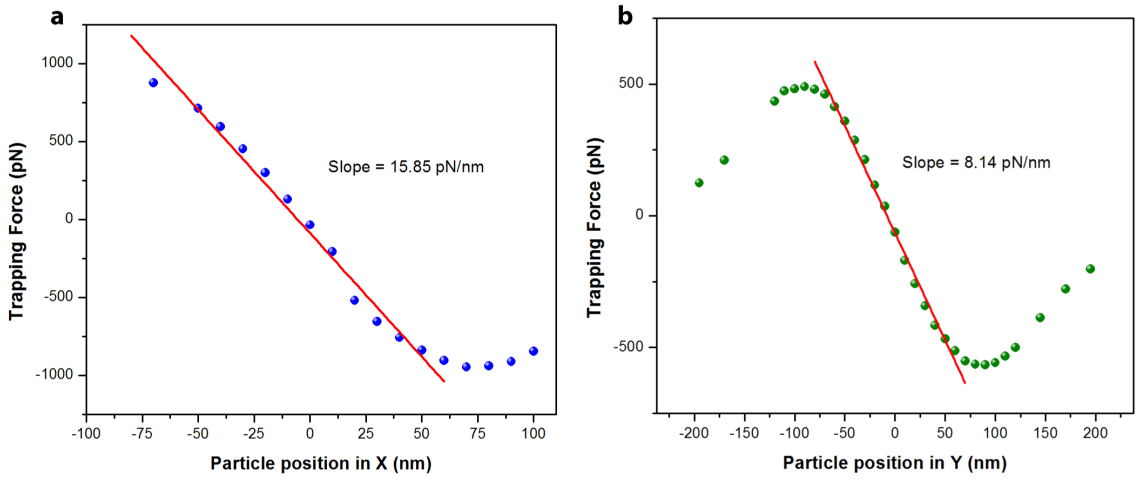

Figure 5.7: Numerical analysis of trapping stiffness for 200-nm polystyrene nanoparticles. All Forces are normalized to 1-W of input power in the waveguide. **(a)** Force experienced by a 200-nm trapped polystyrene nanoparticle as it is displaced along the length of the resonator (X-axis). The zero X-axis value corresponds to the stable trapping position at the lobe centre. The slope in the linear region of the plot indicates a trapping stiffness of 15.85 pN nm^{-1} W^{-1} along the X-axis. **(b)** Graph illustrating the restoring force on a 200-nm particle as it is displaced in the Y-axis, normal to the length of the resonator. The zero Y-axis value corresponds to the stable trapping position at the lobe centre. The slope of the linear region in the plot indicates a trapping stiffness of 8.14 pN nm^{-1} W^{-1} along the Y-axis.

The estimated trapping stiffness for this system is an order of magnitude higher than that of slot waveguides (0.2 pN nm^{-1} W^{-1} for a 100-nm particle [V.9]) and several orders of magnitude higher than other recent optical trapping techniques such as plasmonic tweezers [V.8] (0.013 pN nm^{-1} W^{-1} for a 200-nm bead), conventional high-NA optical tweezers [V.24] (0.16 pN nm^{-1} W^{-1} for a 500-nm bead) and Fresnel zone plate optical tweezers [V.16] (0.1 pN nm^{-1} W^{-1} for a 2-μm bead). While it is difficult to make a clear comparison between these different trapping techniques due to the dependence of the trapping stiffness on particle size, it is evident that the strength of our optical trap exceeds the state-of-the-art by at least an order of magnitude.

The presence of a trapped particle affects the resonant wavelength of the resonator by a small amount. Thus, when a trapped particle escapes from the trap, it induces a slight shift in the resonant wavelength which manifests itself as a discrete jump in the output power from the waveguide. By monitoring the laser power at the output end of the waveguide, it is possible to infer the release of a particle from the optical trap as shown in Figure 5.6(b). It is important to note that this effect is more pronounced in the case of larger nanoparticles [V.25]. As the size of the particle reduces, the induced shift in the resonant wavelength also decreases.

5.4 Conclusions

We have previously demonstrated the capability of this resonator design to perform multiplexed biomolecular detections [V.26]. This coupled with its ability to optically transport nanoparticles along trajectories independent of the microfluidic channel flow and trap, store and reject them opens up exciting possibilities in creating a robust integrated system for the simultaneous probing, detection and handling of biomolecules. An important aspect of this new trapping system is the ability to further improve upon the trapping capabilities by tuning the design geometry. In our current experiments the Q-factor of our resonator was approximately 2500. However, researchers have recently demonstrated the ability to achieve Q-factors higher than 10^7 using similar one-dimensional photonic crystal geometries [V.27-29]. While other optical resonator designs possessing higher Q-factors have been previously demonstrated [V.20, 30], they are not as well suited for trapping applications due to their larger mode volumes, weaker field gradients and propagating nature of their guided optical mode that prevents the static trapping of nanoparticles. Future work focused on the development of high-Q photonic crystal resonator traps will enable

further improvements in trapping capabilities by several orders of magnitude thus opening us up to the realm of single-molecule optical trapping.

Acknowledgements

We thank M. Lipson, A. Nitkowski, S. Moore, and A.H.J. Yang (Cornell) for technical discussions. This work was supported by the Nanobiotechnology Center (NBTC), an STC Program of the National Science Foundation under Agreement No. ECS-9876771, the National Institutes of Health - National Institute of Biomedical Imaging and Bioengineering (NIH-NIBIB) under grant number R21EB007031 and the US National Science Foundation through the NIRT: Active Nanophotofluidic Systems for Single Molecule/Particle Analysis grant CBET-0708599. Device fabrication for this work was performed in part at the Cornell NanoScale Facility, a member of the National Nanotechnology Infrastructure Network, which is supported by the National Science Foundation. Video Spot Tracker software package by CISMM at UNC-CH was supported by the NIH NIBIB (NIH 5-P41-RR02170).

5.5 Supplemental Methods – Trapping Stiffness Measurement

In this article, we estimate the radial trapping stiffness of our resonant optical trap by analyzing the suppressed Brownian motion of a trapped 200-nm polystyrene nanoparticle when the power at the output of the waveguide was measured to be 175 μW. For a particle in a harmonic potential with stiffness k_x, the equipartition theorem states that [V.24]:

$$\frac{1}{2}k_bT = \frac{1}{2}k_x\left\langle x^2\right\rangle \tag{5.1}$$

where k_B is the Boltzmann constant, T is the absolute temperature and $\left\langle x^2\right\rangle$ is the positional variance of the trapped particle. By measuring the instantaneous position of the particle, it is possible to determine the stiffness of the optical trap. However, detection systems such as video cameras do not measure the instantaneous particle position. Instead, they introduce a bias in the measurements due to the finite integration time W of the device. Wong *et al.* [V.31] performed a detailed experimental and theoretical analysis to demonstrate a novel method that accounts for these systematic biases introduced in measurements due to video-image motion blur. The true and measured variance var(X) and var(X_{meas}) are related by [V.16, 31]:

Error! Objects cannot be created from editing field codes. (5.2)

where $S(\alpha)$ is the motion blur correction function. α is given by $Wk_x / 2\pi\gamma$ where γ is the Stoke's drag coefficient and W is 51.17 ms. By combining Equations 5.1 and 5.2 we obtain:

$$\mathrm{var}\left(X_{meas}\right) = \frac{\left(k_BT\right)W}{2\pi\gamma}\left[\frac{S(\alpha)}{\alpha}\right] \tag{5.3}$$

We solve Equation 5.3 numerically for α using values for $\mathrm{var}\left(X_{meas}\right)$ and $\mathrm{var}\left(Y_{meas}\right)$ determined from Figure 5.6. Thus we obtain trap stiffness values along the X and Y axes of 3.73×10^{-3} pN/nm and 3.50×10^{-3} pN/nm respectively. We also determine the true standard deviation of the Brownian fluctuations in the X and Y axes to be 33.2 nm and 34.3 nm respectively.

The resonant output spectrum for the photonic crystal resonator was recorded. The ratio of the output power at the resonant wavelength to the output power for a non-resonant wavelength was determined to be 0.44. Additionally, silicon waveguides

that are fabricated using HSQ/XR-1541 (Dow-Corning Corporation) typically exhibit propagation losses around 2 dB/cm[V.32]. Taking these into account, we estimate the corresponding input power in the waveguide to be 630.4 μW. Thus, the power normalized stiffness for our resonant optical trap is determined to be 5.90 pN nm^{-1} W^{-1} and 5.55 pN nm^{-1} W^{-1} along the *X* and *Y* axes respectively thus giving us a final radial trap stiffness of 2.86 pN nm^{-1} W^{-1}.

By performing a detailed three dimensional finite element numerical analysis we obtain theoretical trap stiffness values of 15.85 pN nm^{-1} W^{-1} (X-axis) and 8.14 pN nm^{-1} W^{-1} (Y-axis) resulting in a net radial trap stiffness of 5.38 pN nm^{-1} W^{-1}. The results of these calculations are shown in Figure 5.7.

REFERENCES

[V.1] Grier, D. G. A revolution in optical manipulation. *Nature* **424**, 810-816 (2003).

[V.2] MacDonald, M. P., Spalding, G. C. & Dholakia, K. Microfluidic sorting in an optical lattice. *Nature* **426**, 421-424 (2003).

[V.3] Wang, M. M. *et al.* Microfluidic sorting of mammalian cells by optical force switching. *Nature Biotechnology* **23**, 83-87 (2005).

[V.4] Jamshidi, A. *et al.* Dynamic manipulation and separation of individual semiconducting and metallic nanowires. *Nat Photon* **2**, 86-89 (2008).

[V.5] Agarwal, R. *et al.* Manipulation and assembly of nanowires with holographic optical traps. *Optics Express* **13**, 8906-8912 (2005).

[V.6] Terray, A., Arnold, J. & Hart, S. J. Enhanced optical chromatography in a PDMS microfluidic system. *Optics Express* **13**, 10406-10415 (2005).

[V.7] Imasaka, T. Optical chromatography. A new tool for separation of particles. *Analusis* **26**, M53-M55 (1998).

[V.8] Grigorenko, A. N., Roberts, N. W., Dickinson, M. R. & ZhangY. Nanometric optical tweezers based on nanostructured substrates. *Nat Photon* **2**, 365-370 (2008).

[V.9] Yang, A. H. J. *et al.* Optical manipulation of nanoparticles and biomolecules in sub-wavelength slot waveguides. *Nature* **457**, 71-75 (2009).

[V.10] Reece, P. J., Garces-Chavez, V. & Dholakia, K. Near-field optical micromanipulation with cavity enhanced evanescent waves. *Applied Physics Letters* **88** (2006).

[V.11] Gaugiran, S. *et al.* Optical manipulation of microparticles and cells on silicon nitride waveguides. *Optics Express* **13**, 6956-6963 (2005).

[V.12] Ashkin, A. Acceleration and trapping of particles by radiation pressure. *Physical Review Letters* **24**, 156-159 (1970).

[V.13] Moffitt, J. R. *et al.* Intersubunit coordination in a homomeric ring ATPase. *Nature* **457**, 446-450 (2009).

[V.14] Ferrer, J. M. *et al.* Measuring molecular rupture forces between single actin filaments and actin-binding proteins. *Proceedings of the National Academy of Sciences* **105**, 9221-9226, doi:10.1073/pnas.0706124105 (2008).

[V.15] Chiou, P. Y., Ohta, A. T. & Wu, M. C. Massively parallel manipulation of single cells and microparticles using optical images. *Nature* **436**, 370-372 (2005).

[V.16] Schonbrun, E., Rinzler, C. & Crozier, K. B. Microfabricated water immersion zone plate optical tweezer. *Applied Physics Letters* **92**, 071112-071113 (2008).

[V.17] Fang, N., Lee, H., Sun, C. & Zhang, X. Sub-diffraction-limited optical imaging with a silver superlens. *Science* **308**, 534-537, doi:10.1126/science.1108759 (2005).

[V.18] Volpe, G., Quidant, R., Badenes, G. & Petrov, D. Surface plasmon radiation forces. *Physical Review Letters* **96**, 238101-238104 (2006).

[V.19] Almeida, V. R., Xu, Q. F., Barrios, C. A. & Lipson, M. Guiding and confining light in void nanostructure. *Optics Letters* **29**, 1209-1211 (2004).

[V.20] Arnold, S. *et al.* Whispering gallery mode carousel - a photonic mechanism for enhanced nanoparticle detection in biosensing. *Optics Express* **17**, 6230-6238 (2009).

[V.21] Mandal, S. & Erickson, D. Nanoscale optofluidic sensor arrays. *Optics Express* **16**, 1623-1631 (2008).

[V.22] Schmidt, B. S., Yang, A. H., Erickson, D. & Lipson, M. Optofluidic trapping and transport on solid core waveguides within a microfluidic device. *Optics Express* **15**, 14322-14334 (2007).

[V.23] Kawata, S. & Sugiura, T. Movement of micrometer-sized particles in the evanescent field of a laser beam. *Optics Letters* **17**, 772-774 (1992).

[V.24] Neuman, K. C. & Block, S. M. Optical trapping. *Review of Scientific Instruments* **75**, 2787-2809 (2004).

[V.25] Barth, M. & Benson, O. Manipulation of dielectric particles using photonic crystal cavities. *Applied Physics Letters* **89**, 253114-253113 (2006).

[V.26] Mandal, S., Goddard, J. M. & Erickson, D. A multiplexed optofluidic biomolecular sensor for low mass detection. *Lab on a Chip* **9**, 2924-2932 (2009).

[V.27] Velha, P. *et al.* Ultracompact silicon-on-insulator ridge-waveguide mirrors with high reflectance. *Applied Physics Letters* **89**, 171121-171123 (2006).

[V.28] Notomi, M., Kuramochi, E. & Taniyama, H. Ultrahigh-Q nanocavity with 1D photonic gap. *Optics Express* **16**, 11095-11102 (2008).

[V.29] Deotare, P. B., McCutcheon, M. W., Frank, I. W., Khan, M. & Loncar, M. High quality factor photonic crystal nanobeam cavities. *Applied Physics Letters* **94**, 121106-121103 (2009).

[V.30] Armani, D. K., Kippenberg, T. J., Spillane, S. M. & Vahala, K. J. Ultra-high-Q toroid microcavity on a chip. *Nature* **421**, 925-928 (2003).

[V.31] Wong, W. P. & Halvorsen, K. The effect of integration time on fluctuation measurements: calibrating an optical trap in the presence of motion blur. *Optics Express* **14**, 12517-12531 (2006).

[V.32] Xiao, S., Khan, M. H., Shen, H. & Qi, M. Compact silicon microring resonators with ultra-low propagation loss in the C band. *Optics Express* **15**, 14467-14475 (2007).

CHAPTER 6

FUTURE DIRECTIONS

6.1 Liquid Core Waveguides for Optical Chromatography

Chapter 2 described the application of liquid core waveguides for enabling optofluidic transport within the liquid core of the waveguide. One of the most interesting aspects of using optical radiation pressure to exert this propulsion force on particles is that the propulsion velocity of particles exhibits a 5^{th} power dependence on the particle size (within the Rayleigh regime) as shown in Equation 2.1. This implies that the optically induced propulsion force is extremely sensitive to the size of the particle. A direct application of this extreme size based sensitivity of the optical force would be to use it for performing optical chromatography [VI.1-3].

To achieve this however, it is critical to overcome the chief limitation in the device design detailed in Chapter 2. The primary drawback of that particular design for performing optical chromatography is that the liquid core waveguide is highly multi-moded due to the large refractive index contrast between the liquid core and the holey air-filled cladding. As a result of this multimoded nature, the optical field distribution within the liquid core is highly lobed and constantly changes with time due to perturbations from the particles propagating within the liquid core. This constantly changing field distribution within the core prevents a uniform propulsion force from being exerted on particles of the same size. This limitation precludes the possibility of performing optical chromatography using that particular design. One way to overcome this is to design a single-mode liquid core waveguiding structure. In this case, the Gaussian shaped mode profile of the single mode liquid-core waveguide

would be ideal for performing optical chromatography. The transverse gradient in the field profile distribution would cause particles to be tweezed towards the center of the optical mode. Subsequently they would all be subjected to the same optical field intensity present at the center of the mode profile. This would enable all particles of the same size to experience the same optical force and thus open up the possibility of performing highly sensitive size based discriminations using optical chromatography.

One method to achieve a single mode liquid-core waveguide has already been demonstrated in literature using antiresonant reflecting optical waveguides (ARROWs) [VI.4]. While ARROWs waveguides are well suited for liquid core waveguiding, it is not possible to easily fabricate extended waveguides with lengths of several meters. Another method that could potentially be used to design a single mode liquid core waveguide would be to design a photonic bandgap fiber such that the hole size and spacing in the holey cladding is optimized to obtain a bandgap for the wavelengths of interest while the holes are liquid filled. This would then allow the liquid core photonic crystal fiber to guide light by the bandgap effect and not by total internal reflection as in the case of the research outlined in Chapter 2. Creating a single mode liquid core waveguide with low optical losses would allow it to then be integrated with a microfluidic channel as shown in Figure 6.1. Particles or cells of interest would be flowed electrokinetically in one direction while the laser light would be coupled into the fiber so that the light propagates in the opposite direction. Depending on the size and refractive index of a particle, it would come to rest at a unique equilibrium position along the length of the liquid-core fiber as illustrated in Figure 6.1. Future work in this area can lead to the realization of the ultimate goal: To achieve extremely sensitive size based discriminations by using low-loss liquid core fibers and very long lengths of optical fiber over which to conduct the optical separations.

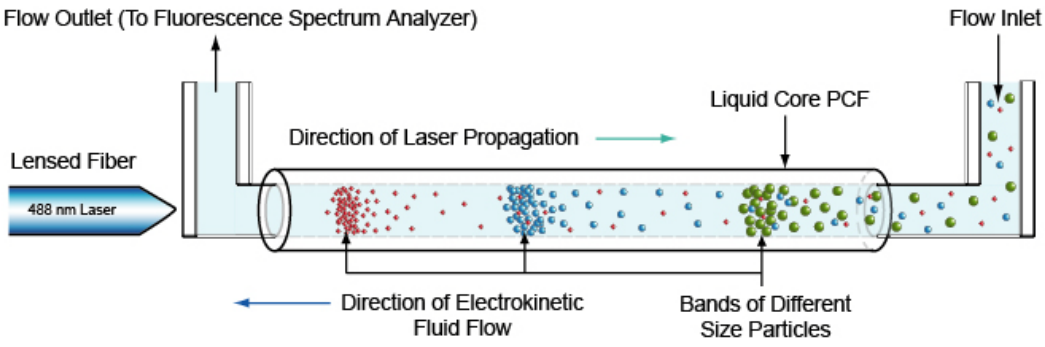

Figure 6.1: Schematic of a proposed optical choromatography setup incorporating a liquid-core photonic crystal fiber embedded in a microfluidic channel. A lensed fiber is used to couple laser light into one end of the fiber while the microfluidic flow is driven electrokinetically in the direction opposite to light propagation.

6.2 Nanoscale Optofluidic Sensor Arrays for Ultra-sensitive, Multiplexed, Label-free Detections

Chapter 3 and 4 described in detail nanoscale optofluidic sensor arrays (NOSA) and their application towards performing highly multiplexed biomolecular detections. The experimental results demonstrated the ability to detect anti-streptaviding at concentrations as low as 0.1 μg/ml as well as the ability to perform 5 detections in parallel using this architecture. One of the chief limitations of the demonstrated design was the low Q-factors of the devices which were on the order of 3000. Low Q-factors lead to larger line-widths for the resonance thus making it harder to discern small shifts in the resonance wavelength. This directly affects the resolution limit of the device. Usually, it is possible to resolve wavelength shifts on the order of $\Delta\lambda/50$ where $\Delta\lambda$ is the line-width of the resonance. Thus, for NOSA resonators with a Q-

factor of 3000, this is approximately 0.01 nm. However, to detect femtomolar concentrations of molecules requires the ability to resolve shifts as small as $1/10^{th}$ of a picometer. Thus the NOSA device design requires further improvements to enhance the Q-factor by orders of magnitude so as to enable such low resolution limits. As described in Chapters 4 and 5, there has been significant research on high-Q, air-clad, one dimensional photonic crystal resonators [VI.5-7] where researchers have demonstrated the ability to boost the quality factor of these devices to over one million.

Such high quality factors are enabled by gradually tapering the hole geometry and the lattice spacing of the photonic crystal mirrors so as to adiabatically match the effective index of the guided resonant mode in the cavity to the effective index of the bloch mode within the photonic crystal mirror [VI.7]. This is a three orders of magnitude improvement in quality factor in comparison to our current devices which would enable sub-picometer resolution for our NOSA devices. Thus, future work on improving the quality factor of these resonators will help greatly enhance the device sensitivity of the sensors. In addition, with significantly narrower line-widths, it will also enable an even greater extent of multiplexing since the resonances can be more closely packed together. It is conceivable that over a thousand detections could be carried out in parallel along a single waveguide with further improvements in the q-factor of these resonant sensors. The ability to also multiplex in two dimensions by having multiple such waveguides on a chip can open the doors to doing massively multiplexed detections with these nanoscale sensors without sacrificing their sensitivity and their ability to utilize small sample volumes for performing biomolecular detections.

6.3 Silicon Photonic Crystal Nanotweezers for Single Molecule Trapping

Chapter 5 detailed the use of silicon photonic crystal resonators for optically trapping nanoparticles as small as 50-nm. While this is an improvement by several orders of magnitude over conventional optical trapping techniques, the challenge remains to design novel trapping designs capable of producing optical traps strong enough so as to enable the trapping of a single protein or other biomolecules of interest. Such advances could pave the way for enabling novel single molecule studies. However, to achieve this, it is necessary to bring about further improvements in the design of these optical traps.

As described previously, the strength of an optical trap is dependent on the magnitude of the optical field gradient at the trapping site. This can be improved by increasing the total optical power in the trap or by enhancing the confinement of the optical field so as to generate stronger field gradients. The optical field strength in the trap can be increased by exploiting resonance so as to amplify the optical field within the resonator. The extent of this field enhancement is directly related to the quality-factor of the resonators. Designing ultra-high q-factor photonic crystal resonators provides a means for enabling extremely strong optical traps. One drawback however, is that as the optical field intensity within the resonator increases, the risk of damaging trapped molecules due to extremely high field intensities also rises. Thus, increasing the q-factor of the optical traps to enhance trap strength can only be useful up to a certain point.

However, another way to enhance the strength of an optical trap is to increase the confinement of the optical field to create stronger field gradients. While silicon photonic crystal resonators are already able to generate extremely strong sub-wavelength scale field confinement, this can be further improved with the use of

slotted geometries [VI.8-9] within the resonator. These slotted geometries exploit the discontinuity in the electric field at dielectric interfaces to produce extremely strong optical field confinement in slots as small as a few nanometers. Future work on the design of high-q, slotted photonic crystal resonators will enable a new generation of optical traps with the potential for performing single molecule trapping and manipulations.

REFERENCES

[VI.1] Hart, S. J., Terray, A., Kuhn, K. L., Arnold, J. & Leski, T. A. Optical chromatography of biological particles. *American Laboratory* **36**, (2004).

[VI.2] Imasaka, T. Optical chromatography. A new tool for separation of particles. *Analusis* **26**, M53-M55 (1998).

[VI.3] Kaneta, T., Ishidzu, Y., Mishima, N. & Imasaka, T. Theory of optical chromatography. *Analytical Chemistry* **69**, 2701-2710 (1997).

[VI.4] Yin, D., Deamer, D. W., Schmidt, H., Barber, J. P. & Hawkins, A. R. Integrated optical waveguides with liquid cores. *Applied Physics Letters* **85**, 3477-3479 (2004).

[VI.5] Sauvan, C., Lecamp, G., Lalanne, P. & Hugonin, J. Modal-reflectivity enhancement by geometry tuning in Photonic Crystal microcavities. *Optics Express* **13**, 245-255 (2005).

[VI.6] Velha, P. *et al.* Ultracompact silicon-on-insulator ridge-waveguide mirrors with high reflectance. *Applied Physics Letters* **89**, 171121-171123 (2006).

[VI.7] Deotare, P. B., McCutcheon, M. W., Frank, I. W., Khan, M. & Loncar, M. High quality factor photonic crystal nanobeam cavities. *Applied Physics Letters* **94**, 121106-121103 (2009).

[VI.8] Yang, A. H. J. *et al.* Optical manipulation of nanoparticles and biomolecules in sub-wavelength slot waveguides. *Nature* **457**, 71-75 (2009).

[VI.9] Lin, S., Hu, J., Kimerling, L. & Crozier, K. Design of nanoslotted photonic crystal waveguide cavities for single nanoparticle trapping and detection. *Optics Letters* **34**, 3451-3453 (2009).